

*El objetivo general de esta Tesis Doctoral es el desarrollo de metodologías de teledetección cuantitativa para la determinación del estado hídrico de la vegetación basándose en el desarrollo de un vehículo aéreo no tripulado equipado con sensores de imagen multispectrales y térmicos. Este tipo de vehículos, dotados de los sensores apropiados, puede ofrecer un nivel de precisión en la caracterización del estado hídrico de cultivos inaccesible hasta ahora. Para tal fin se han desarrollado metodologías de calibración radiométrica y corrección atmosférica que permiten la obtención de imágenes de reflectancia y temperatura de superficie a partir de sensores no calibrados. Las imágenes adquiridas han sido validadas mediante la estimación de parámetros biofísicos a partir del uso de índices de vegetación de banda estrecha conectados con modelos de transferencia radiativa que simulan la interacción de la radiación con la vegetación a escala de cubierta.*

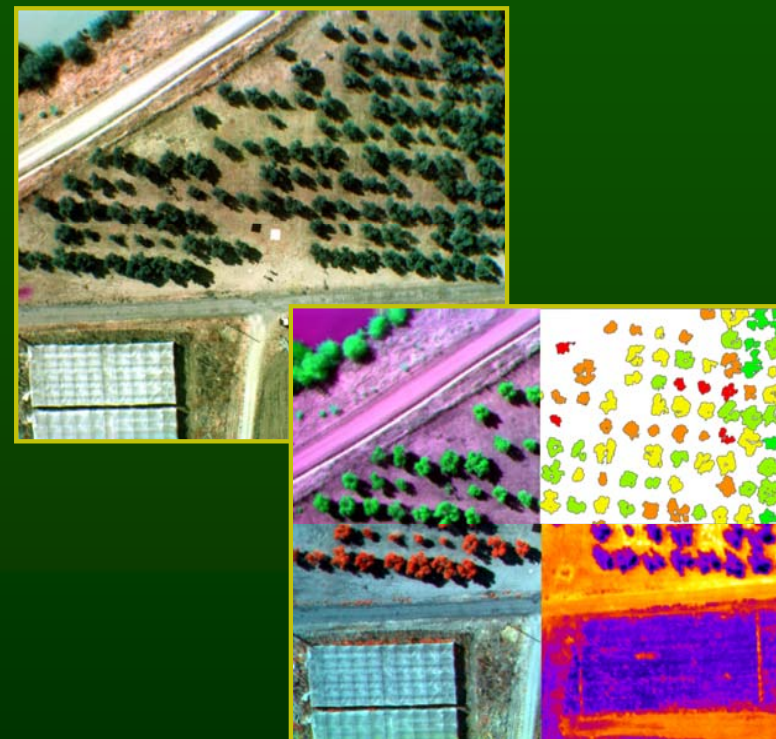
*Se presentan dos metodologías para la cuantificación del estado hídrico de la vegetación. La primera está basada en el uso de imágenes multispectrales de alta resolución espacial y bandas de 1nm de ancho para la detección de la fluorescencia clorofílica, parámetro éste relacionado con la fotosíntesis de la planta y que ha sido propuesto como indicador de su estado hídrico. El método utilizado para la detección de la fluorescencia ha sido el del denominado in-filling en la banda del oxígeno atmosférico, ya que es el menos afectado por factores como el contenido clorofílico y la densidad foliar. La segunda metodología utiliza imágenes térmicas de alta resolución espacial junto con datos meteorológicos para cuantificar la conductancia de la cubierta aplicando un balance de energía a nivel de copa. Esto permite la generación de mapas de conductancia y por lo tanto mostrar la distribución espacial del estrés hídrico. Se han usado distintos modelos físicos para determinar los parámetros de entrada en las ecuaciones de balance de energía. También se ha adaptado el Crop Water Stress Index a nivel de imagen como metodología para normalizar los valores de conductancia.*

## Determinación del estado hídrico de la vegetación mediante teledetección basada en vehículos aéreos no tripulados

José A. Jiménez Berni

TESIS DOCTORAL

2009



José Antonio Jiménez Berni

UNIVERSIDAD DE CÓRDOBA  
DEPARTAMENTO DE AGRONOMÍA

TESIS DOCTORAL

**Determinación del estado hídrico de la  
vegetación mediante teledetección basada en  
vehículos aéreos no tripulados**

*José Antonio Jiménez Berni*

Córdoba, Octubre 2.009



**DEPARTAMENTO DE AGRONOMÍA**

**UNIVERSIDAD DE CÓRDOBA**

Título de la tesis: Determinación del estado hídrico de la vegetación mediante teledetección basada en vehículos aéreos no tripulados

Autor: José Antonio Jiménez Berni

Presentada en satisfacción de los requisitos necesarios para la obtención del grado de

**DOCTOR INGENIERO AGRÓNOMO**

Dirigida por los Doctores:

Pablo J. Zarco Tejada

Elías Fereres Castiel

El Doctorando,

José Antonio Jiménez Berni

Córdoba, Octubre de 2009

# Índice

Índice.....	ii
Índice de Figuras .....	iv
Índice de Tablas.....	vii
Agradecimientos.....	x
Resumen .....	xii
Abstract.....	xiv
Introducción General .....	1
Visión histórica.....	2
Limitaciones actuales .....	5
Determinación del estado hídrico de la vegetación.....	8
Presentación del trabajo.....	12
Referencias.....	14
Objetivos Generales.....	21
Thermal and Narrowband Multispectral Remote Sensing for Vegetation Monitoring From an Unmanned Aerial Vehicle .....	25
Resumen.....	26
Abstract .....	27
1. Introduction.....	28
2. Methods .....	30
2.1. UAV and payload description .....	30
2.2. Multispectral sensor calibration and vegetation indices used for parameter estimation.....	35
2.3. Methods for surface temperature estimation.....	40
2.4. Automatic mosaicking with aerotriangulation methods.....	43
2.5. Study sites .....	45
3. Results and Discussion.....	46
4. Conclusions .....	54
Acknowledgments.....	55
References.....	55
Imaging chlorophyll fluorescence with an airborne narrow-band multispectral camera for vegetation stress detection .....	63
Resumen.....	64
Abstract .....	65
1.Introduction.....	66
2. Materials and Methods .....	69
2.1. Assessing the sensitivity of fluorescence indices and the <i>in-filling</i> <i>method</i> using the FluorMOD simulation model.....	69
2.2. Field experiments and airborne campaigns .....	75
3. Results .....	81
3.1. Simulation Results .....	81
3.2. Experimental results.....	84
4. Conclusions .....	90
Acknowledgements.....	92
References.....	93
Mapping canopy conductance and CWSI in olive orchards using high resolution thermal remote sensing imagery. ....	99
Resumen.....	100
Abstract .....	101
1. Introduction.....	102

2. Model Approach for estimating Canopy Conductance .....	104
2.1. Net Radiation Modeling.....	105
2.2. Aerodynamic Resistance Modeling.....	106
2.3. Modelling CWSI.....	107
3. Materials and Methods .....	108
3.1. Field data collection.....	108
3.2. Airborne Campaigns .....	109
4. Results and Discussion.....	111
4.1. Model Performance.....	111
4.2. Model Validation using ground thermal sensors.....	114
4.3. Model Validation using airborne remote sensing thermal imagery .....	115
4.4. Mapping CWSI at high resolution in open-canopy orchards .....	117
5. Concluding remarks.....	120
6. Acknowledgements.....	121
References .....	122
Discusión general .....	127
Conclusiones generales.....	133

## Índice de Figuras

Figura 1. Imagen multispectral adquirida en 1964 sobre distintos cultivos.....	3
Figura 2. Esquema del flujo de datos del programa LACIE.....	4
Figura 3. El UAV solar Pathfinder de la NASA volando sobre campos de café en Hawaii. Cortesía NASA.....	7
Figura 4. Comparación de la reflectancia de una cubierta fluorescente y otra no fluorescente. Se puede apreciar el pico en la región de absorción de O <sub>2</sub> .....	11
Figure 1.1. Block diagram showing the components for the autopilot and ground control station. ....	31
Figure 1.2. Sample flight plan undertaken over four study sites, showing the path followed by the platform.....	32
Figure 1.3. Changes of the radiometric temperature measured by the camera after power on over the course of two hours.....	34
Figure 1.4. Multispectral imagery collected by the MCA-6 camera at 0.15m spatial resolution and 6 spectral bands with 10 nm FWHM; spectra extracted from different image targets in the 400-800 nm spectral region. ....	36
Figure 1.5. Validation of the surface reflectance acquired by the MCA-6 multispectral camera as compared with the ASD field spectrometer. The plot shows 90 points from 3 flights over 5 targets (3 corn crop sites, 1 soil target, and 1 cotton site) for 6 spectral bands. ....	37
Figure 1.6. Algorithm to estimate chlorophyll a+b from TCARI/OSAVI index developed with the FLIGHT radiative transfer model.....	39
Figure 1.7. Simulated atmospheric transmittance and thermal radiation as function of platform altitude; effects of flight altitude and atmospheric conditions Ta(°C)/%RH on the surface temperature estimation for a black body at 300K; distribution of the atmospheric correction effects as function of the off-nadir view for a uniform black body at 300K, atmospheric conditions 20°C / 60% RH, flight altitude of 150m, pitch=10° and roll=6°. ....	41
Figure 1.8. Comparison between ground truth surface temperature (IRT measured) and obtained from the thermal camera at 150 m flight altitude before and after applying the atmospheric correction. ....	43
Figure 1.10. Multispectral ortho-mosaic collected over a peach orchard at 20 cm spatial resolution; spectral reflectance extracted from different targets from the image mosaic.....	45
Figure 1.11. Thermal ortho-mosaic obtained from the UAV over the peach orchard at 40 cm resolution.....	47
Figure 1.12. Corn plots of different varieties imaged by the MCA-6 camera onboard the UAV system; extracted reflectance spectra in the 530-570 nm spectral region for the calculation of the PRI index used for stress detection. ....	48
Figure 1.13. Relationships obtained between the FLIR thermal camera and spectral indices calculated from the multispectral camera over corn blocks under same NDVI levels.....	49
Figure 1.14. Thermal images acquired over the corn field at 0.4m pixel resolution showing the Tc-Ta changes at four different times of day.....	50
Figure 1.15. Diurnal stomatal conductance (G) and canopy Tc-Ta acquired from two corn cultivars.. ....	50
Figure 1.16. Ground truth chlorophyll content (Cab) measured in olive and peach trees compared with UAV-estimated Cab through the TCARI/OSAVI index and predictive algorithms. ....	51

Figure 1.17. Relationships between NDVI and LAI for corn and olive trees; validation of LAI estimates from the UAV vs ground truth LAI measurements. ....	52
Figure 1.18. Sample multispectral imagery acquired over an olive orchard with the MCA 6 camera at 10 nm FWHM bandwidths onboard the UAV platform (0.15 m spatial resolution), showing the chlorophyll content and LAI maps obtained. ....	53
Figure 2.1. FluorMOD model simulation of irradiance and canopy radiance at 1 nm resolution in the 400-800 nm range and 740-800 nm, reproducing the fluorescence in-filling at O2 A and O2-B bands using atmospheric, leaf and canopy inputs from Table 2.1. ....	73
Figure 2.2. FluorMOD leaf fluorescence, both reflected and transmitted, for a simulated leaf with $F_i=0.049$ and $C_{ab}=43 \mu\text{g}/\text{cm}^2$ ; leaf reflectance with added simulated fluorescence and without fluorescence, showing the reflectance difference. ....	73
Figure 2.3. Simulated canopy reflectance in the 400-800 nm range and 740-800 nm with and without fluorescence effects. Fluorescence radiance ( $\text{W}\cdot\text{m}^{-2}\cdot\mu\text{m}^{-1}\cdot\text{sr}^{-1}$ ) added to the canopy reflectance is extracted by reflectance difference calculation. ....	74
Figure 2.4. Simulated fluorescence radiance used to simulate the derivative canopy reflectance with and without fluorescence effects. ....	75
Figure 2.5. Multispectral airborne images acquired at 15 cm spatial resolution over each study site on olive orchard, peach, orange and olive variety trial field with 1 nm FWHM bandwidths on bands used for fluorescence retrievals. ....	78
Figure 2.6. Diurnal measurements of the white spectralon reference panel radiance conducted at the time of flight acquisitions at 0.065 nm spectral resolution in the O <sub>2</sub> -A spectral region (756-774 nm). White and dark target radiance used for airborne image calibration at 760.5 and 757.5 nm bands. ....	79
Figure 2.7. Calibrated images at 10 nm FWHM, and 1 nm FWHM at 757.5 nm and 760.5 nm used to extract crown radiance (fluorescing) and soil radiance (non-fluorescing) targets to estimate crown chlorophyll fluorescence using the <i>in-filling</i> method. ....	80
Figure 2.8. Synthetic leaf spectra generated with FluorMOD using random input parameters $F_i$ (0.03-0.06), $C_{ab}$ (30-80 $\mu\text{g}/\text{cm}^2$ ), and LAI (2-4). Leaf fluorescence emission ( $\text{W}\cdot\text{m}^{-2}\cdot\mu\text{m}^{-1}\cdot\text{sr}^{-1}$ ) and leaf reflectance show a wide range of both fluorescence and chlorophyll content variation. ....	81
Figure 2.9. Simulations conducted with FluorMOD model for parameters $F_i$ (0.03-0.06), $C_{ab}$ (30-80 $\mu\text{g}/\text{cm}^2$ ), and LAI (2-4) for canopy radiance and canopy reflectance. ....	82
Figure 2.10. Fluorescence retrievals from the synthetic canopy reflectance simulations using the <i>in-filling</i> method, derivative index $D_{702}/D_{680}$ , and reflectance indices $R_{690}/R_{630}$ , and $R_{761}-R_{757}$ . ....	83
Figure 2.11. Relationship obtained between ground-truth $F_s$ (PAM-2100) and fluorescence extracted from the airborne image using the <i>in-filling</i> method in a water-stress experiment conducted on an olive orchard. ....	85
Figure 2.12. Relationship obtained between ground-truth $F_s$ (PAM-2100) and fluorescence extracted from the airborne image using the <i>in-filling</i> method in a water-stress experiment conducted on a peach orchard. ....	86

Figure 2.13. Diurnal trend for both airborne fluorescence and field measured fluorescence using the PAM-2100 instrument acquired at 7.40, 11.00 and 12.50 GMT.....	87
Figure 2.14. Results obtained between airborne fluorescence estimates and ground truth assimilation and yield measured in the olive variety trial experiment. Relationships obtained between airborne crown temperature and airborne fluorescence and airborne-estimated chlorophyll content. ....	88
Figure 2.15. Image of the fluorescence estimates acquired at 15 cm pixel resolution using the in-filling method at the crown level from the multispectral image, showing the spatial variability of the vegetation fluorescence in-filling within the orchard. ....	89
Figure 3.1. Airborne thermal imagery acquired over the study site: AHS image collected at 12:30GMT on 16 July 2005; UAV image collected at 13:30 GMT on 23 August 2007; image detail showing the spatial resolution differences of AHS (2m) against the UAV (40cm). ....	110
Figure 3.2. Diurnal course of net radiation ( $R_n$ ), sensible heat ( $H_c$ ) and latent heat ( $\lambda E_c$ ), hourly averaged for each treatment on DOY 197.....	112
Figure 3.3. Hourly averaged estimations for simulated canopy conductance on DOY 197 using Eq. 3.4. ....	113
Figure 3.4. Seasonal variation of canopy conductance ( $G_c$ ) for the three different irrigation treatments obtained from the infrared sensor temperature at 12:00GMT during summer 2005. ....	113
Figure 3.5. Relationship obtained between the measured canopy conductance ( $G_c$ ) and the estimated $G_c$ for individual tree measurements at three times on 16 July 2005 and treatment averages during summer of 2005.....	114
Figure 3.6. Relationship obtained for the field-measured leaf stomatal conductance and from the AHS imagery estimates for individual trees at the different times (7:30GMT, 9:30GMT and 12:30GMT) on DOY 197, 2005. ....	115
Figure 3.7. Canopy conductance map obtained from the UAV thermal imagery at 13:30 GMT 23 August 2007. ....	116
Figure 3.8. Validation of the canopy conductance estimations against field measurements. ....	117
Figure 3.9. CWSI map obtained from the UAV high resolution thermal imagery at 13:30 GMT on 23 August 2007. ....	118
Figure 3.10. Relationships between the estimated CWSI from the UAV thermal imagery with leaf water potential and canopy conductance. ....	119
Figure 3.11. Simulations of NWSB for CWSI from 4 weather conditions. ....	120

## Índice de Tablas

Table 1.1. Multispectral MCA-6 Image Sensor Specifications .....	33
Table 1.3. FLIR and MCA cameras intrinsic parameters.....	35
Table 1.4. Nominal values and parameters used for leaf and canopy modeling with PROSPECT and FLIGHT for the peach study site. ....	39
Table 2.1. FluorMOD model inputs used in this study to assess the sensitivity of reflectance indices using atmospheric, leaf and canopy inputs. ....	72
Table 2.2. Relationships obtained between FluorMOD inputs and fluorescence estimates using the <i>in-filling</i> method, reflectance and derivative reflectance indices sensitive to chlorophyll fluorescence.....	84



A mis padres  
A Arantxa, mi futura esposa

## Agradecimientos

Los resultados presentados en esta Tesis Doctoral son el resultado de largas horas de trabajo y no poca inversión económica, pero su realización habría sido imposible sin la ayuda de un buen número de personas que han contribuido en mayor o menor medida en las distintas etapas de su realización.

En primer lugar me gustaría agradecer de forma especial a Pablo J. Zarco Tejada, mi maestro en el mundo de la investigación y quien un buen día quiso darme la oportunidad de poner en mis manos una serie de ideas ‘descabelladas’ que al final han resultado ser totalmente brillantes. Mucho ha llovido desde aquel primer día en que, como niños en el Día de Reyes, abrimos la caja del primer helicóptero llegado de USA. Poca gente como Pablo conoce realmente el esfuerzo que ha supuesto llegar hasta el punto en el que estamos hoy y nadie como él ha sido modelo en el modo de superar los fracasos y anticipar los triunfos. Gracias Pablo.

Quiero continuar agradeciendo a Elías Fereres, quien ha sido un apoyo fundamental en esta aventura y quien desde primero de carrera me enseñó cómo la agricultura se podía interpretar desde un punto de vista científico. Siempre me acordaré del día en que me pasó el artículo de Jackson del 77 y me dijo “esto es histórico”.

Una clave fundamental del éxito de este trabajo ha venido por parte de Alberto Vera y David Notario, nuestros pilotos, gracias a los cuales hemos podido volar seguros y sin muchos contratiempos. Sin su trabajo en el día a día no tendríamos más que un amasijo de metal. También quiero agradecer a Ignacio Calatrava, quién desde el primer día ha estado dispuesto a echarme un cable (nunca mejor dicho) y a Miguel Ruíz Bernier, quien nos ha sabido transmitir el entusiasmo por el radio control y nos ha transmitido muchos de sus conocimientos.

Tampoco habría sido posible esta Tesis sin la ayuda del resto de miembros de Quantalab: Guadalupe fue la primera en estar ahí, quien me introdujo en el maravilloso mundo del térmico y parte de su legado está presente en este trabajo; Lola por sus horas haciendo ROIs y su ayuda con los modelos; Mariluz por su ayuda en tantas medidas de campo; y por supuesto Jesús, Manoli y Alberto Hornero, ya que todos habéis estado dispuestos a arrimar el hombro y a sacar adelante estas ideas.

También quiero agradecer al resto de autores de los artículos publicados, especialmente a Francisco Villalobos, por sus ideas sobre la estimación de

conductancia. Y a todos los compañeros del departamento: Luca, Auxi, Carmen Ruz, Oscar, Marga y Manuel. Gracias por vuestro tiempo y vuestro apoyo.

No quiero terminar sin agradecer a todos mis amigos, que siempre han estado ahí a pesar de mi enclaustramiento y mi época 'antisocial'. A Miguel, Rafa, Isa, Enrique, Trini, Oscar, Elena, Santi, Almudena y Javi... gracias a todos.

Finalmente quiero dedicar este trabajo a mis padres, Fermín y Loli. Gracias a ellos tuve la oportunidad de estudiar y nunca estaré lo suficientemente agradecido por su paciencia, sus sacrificios y su apoyo.

Y por último, y en un lugar especial, quiero agradecer y dedicar esta Tesis a Arantxa. Tú sabes mejor que nadie el esfuerzo que hay tras estas líneas y nada de esto habría sido posible sin tu apoyo incondicional. Gracias a ese apoyo, dejé mi trabajo anterior para hacer esta Tesis y centrarme en la investigación. Gracias a ti no he tirado la toalla ante las primeras dificultades, pues tú siempre has estado ahí con una sonrisa, un abrazo y un consejo. Espero que, sobre todo ahora que empezamos una nueva vida, pueda compensarte por todas las horas que te he robado durante este tiempo.

## Resumen

La teledetección actual presenta una serie de limitaciones que han provocado la inexistencia de aplicaciones reales y disponibles de forma operativa en el sector de la agricultura. Una aplicación hasta ahora inviable es la determinación precisa del estado hídrico de una superficie cultivada y la generación de mapas de estrés hídrico que permitan hacer una gestión eficiente del agua de riego. Los satélites actuales carecen de la resolución espacial, espectral y temporal para este tipo de aplicaciones. La alternativa, que podría basarse en el uso de sensores aerotransportados, no ha sido implementada activamente debido a los costes y complejidad operativa de este tipo de sensores. Con el desarrollo en los últimos años de los vehículos aéreos no tripulados, se abren nuevas posibilidades para su utilización como plataformas de teledetección.

El objetivo general de esta Tesis Doctoral es el desarrollo metodologías de teledetección cuantitativa para la determinación del estado hídrico de la vegetación basándose en el desarrollo de un vehículo aéreo no tripulado equipado con sensores de imagen multiespectrales y térmicos. La hipótesis de trabajo es que este tipo de vehículos dotados de sensores apropiados puede ofrecer un nivel de precisión en la caracterización del estado hídrico de cultivos inaccesible hasta ahora.

Para tal fin se han desarrollado metodologías de calibración radiométrica y corrección atmosférica que permiten la obtención de imágenes de reflectancia y temperatura de superficie a partir de sensores no calibrados. Las imágenes adquiridas han sido validadas mediante la estimación de parámetros biofísicos a partir del uso de índices de vegetación de banda estrecha conectados con modelos de transferencia radiativa que simulan la interacción de la radiación con la vegetación a escala de cubierta.

Se presentan dos metodologías para la cuantificación del estado hídrico de la vegetación. La primera está basada en el uso de imágenes multiespectrales de alta resolución espacial y bandas de 1 nm de ancho para la detección de la fluorescencia clorofílica, parámetro éste relacionado con la fotosíntesis de la planta y que ha sido propuesto como indicador de su estado hídrico. Se ha utilizado el modelo FluorMOD para determinar la influencia de factores como el contenido de clorofila y el índice de área foliar en las distintas metodologías publicadas. El método utilizado para la detección de la fluorescencia ha sido el denominado *in-filling* en la banda del oxígeno atmosférica, ya que es el menos afectado por estos dos factores.

La segunda metodología utiliza imágenes térmicas de alta resolución espacial junto con datos meteorológicos para cuantificar la conductancia de la cubierta aplicando un balance de energía a nivel de copa. Esto permite la generación de mapas de conductancia y por lo tanto mostrar la distribución espacial del estrés hídrico. Se han usado distintos modelos físicos para determinar los parámetros de entrada en las ecuaciones de balance de energía y minimizar las medidas de campo necesarias. Finalmente, para obtener un mapa normalizado, se ha adaptado el *Crop Water Stress Index* para su uso a nivel de imagen usando las ecuaciones analíticas del mismo.

Las dos metodologías se han validado con medidas de campo, mostrándose como buenos indicadores del nivel de estrés hídrico en vegetación y demostrando la viabilidad para su cuantificación mediante plataformas no tripuladas. El uso de estas metodologías, junto con el uso de vehículos aéreos no tripulados, que permiten una alta resolución espacial y temporal, supondrá un avance cualitativo en la aplicación de metodologías de teledetección cuantitativa en agricultura, posibilitando el desarrollo de aplicaciones que permitan la gestión eficiente del riego en cultivos agrícolas.

## Abstract

The limitations of remote sensing have restricted until now the existence of operational real time applications in agriculture, such as the detection of water status in vegetation and the generation of water stress maps which could result in a more efficient water management. Present satellites lack the spatial, spectral and temporal resolution required for these applications. An alternative, based on the use of airborne sensors, has not been actively implemented mainly due to the costs and operational complexity of this type of platforms. The development of the unmanned aerial vehicles during the last years brings about new possibilities for their use as remote sensing platforms.

The aim of this PhD Thesis is the development of new methodologies of quantitative remote sensing to assess the water status of vegetation. Those methodologies use images acquired by means of unmanned aerial vehicles (UAV) equipped with multispectral and thermal imaging sensors. The working hypothesis is that UAVs equipped with the appropriate sensors could provide a level of precision in the detection of water stress via remote sensing that has not been available before.

Different methodologies have been developed to perform radiometric calibration and atmospheric correction in order to obtain images of reflectance and surface temperature from non-calibrated imaging sensors. To validate the acquired imagery, different biophysical parameters have been estimated using narrowband vegetation indexes connected to radiative transfer models which simulate the interaction of radiation and vegetation at canopy scale.

Two methodologies are presented here to quantify the water status of vegetation. The first one is based on the use of very high spatial resolution multispectral imagery with 1nm of band width in order to detect chlorophyll fluorescence. This parameter is related with the photosynthesis and has been proposed as an indicator of water stress. FluorMOD model have been used to determine the influence of factors such as chlorophyll content or leaf area index on different methodologies published. The method called *in-filling* in the oxygen band, has been chosen to detect fluorescence since this is the less affected by those factors.

The second methodology uses thermal imagery of high spatial resolution together with meteorological data in order to quantify the canopy conductance based on energy balance equations at crown level. This allows the generation of canopy conductance maps and thus the spatial distribution of water stress. Different physical models have been used to obtain the input parameters of the energy balance equations and to minimize the need of additional field

measurements. Finally, in order to obtain a normalized map with values from 0 to 1, the Crop Water Stress Index has been adapted to be used at image level using analytical equations.

Both methodologies have been validated using field measurements, and have shown to be good indicators of the levels of water stress in vegetation, demonstrating the feasibility to use them from an unmanned aerial vehicle. The use of these methodologies together with the use of unmanned aerial vehicles which allow a high spatial and temporal resolution will result in a qualitative advance in the application of quantitative remote sensing techniques in agriculture, allowing the development of applications directed at improving irrigation water management.



## Introducción General

*"Todo lo que una persona puede imaginar, otras podrán hacerlo realidad."*

Julio Verne (1828-1905).

Pocos años después de la aparición de los primeros sensores térmicos a finales de la década de los sesenta, algunos investigadores parecían tener una visión clara de la aplicación de la teledetección en agricultura y en concreto en la detección del estado hídrico de la vegetación. Ray D. Jackson, en uno de sus trabajos clásicos (Jackson et al., 1977) propuso que,

*... “La información presentada en este informe proporciona una infraestructura con la que se podría concebir un sistema de programación de riego para grandes comunidades de regantes. Un escáner térmico aerotransportado podría determinar la temperatura de las cubiertas y esta información se procesaría en una estación central. Los ordenadores recibirían estos datos para crear mapas de estrés diario para una zona, a partir de los cuales se podrían tomar decisiones de manejo de agua. El escáner y la tecnología ya están disponibles. Será necesario refinar los conceptos propuestos en este artículo y su extensión a otros cultivos y lugares. Estamos ante los comienzos del desarrollo de un sistema de riego totalmente automatizado en los que los instrumentos monitorizan las plantas para detectar signos de estrés hídrico y envían señales a otros dispositivos para proporcionarles automáticamente la cantidad necesaria de agua.”*

Posteriormente, en 1984, si bien Jackson era consciente de las limitaciones que existían, tenía la esperanza de que en 10 años esos problemas estuvieran resueltos y expuso la siguiente visión:

*“Un sistema que será posible dentro de 10 años, usará aviones solares de gran autonomía para patrullar áreas agrícolas durante toda la temporada de crecimiento. Los datos estarán disponibles inmediatamente para los agricultores mediante un enlace directo con sus ordenadores personales. Un número de estaciones de investigación contarán con programas activos que deberían dar una rápida interpretación de las imágenes adquiridas con la ayuda de inteligencia artificial y sistemas expertos que proporcionen un análisis instantáneo a los agricultores. La necesidad es obvia, los beneficios potenciales son enormes. Es hora de cumplir las promesas del pasado cuarto de siglo.”*

Lamentablemente, tras 32 años de la primera cita y 25 de la segunda, esas visiones siguen pareciendo totalmente futuristas, y aunque las oportunidades puedan estar claras, hay una serie de limitaciones aún no resueltas. Así, en pleno siglo XXI, la agricultura sigue esperando que se cumplan las promesas que la teledetección hizo en el siglo pasado.

### ***Visión histórica***

Se podría decir que la teledetección tiene sus orígenes en 1858 cuando Gaspard-Félix Tournachon tomó la primera fotografía aérea desde un globo aerostático. Sin embargo, los primeros usos de imágenes aéreas para la determinación de propiedades de la vegetación datan de 1956 (Keegan et al., 1956) cuando se usaron películas infrarrojas en fotografía aérea para la

detección de la roya del trigo. Tras el lanzamiento en 1960 del primer satélite meteorológico TIROS-1 y del que se recibieron las primeras imágenes de la Tierra, en 1966 se creó el Laboratorio de Teledetección Agrícola (*Laboratory for Agricultural Remote Sensing*) en *Purdue University*, Michigan, EEUU. En dicho laboratorio se utilizaron los primeros sensores multispectrales aerotransportados con fines agrícolas. Las primeras aplicaciones de este tipo de sensores eran la identificación de cultivos (Hofjer, 1967) o la detección de enfermedades como por ejemplo el tizón del maíz (Bauer et al., 1971). Por aquel entonces ya se usaban sensores aerotransportados de origen militar, operados por la NASA, y que contaban un número considerable de bandas (12 en algunos casos) en el rango espectral del ultravioleta al infrarrojo térmico. Las imágenes se registraban indistintamente en películas con emulsiones sensibles a distintas longitudes de onda combinadas con el uso de filtros de distintos ancho de banda, o bien en cintas magnéticas mediante el uso de sensores de barrido y detectores electrónicos (Fig. 1).

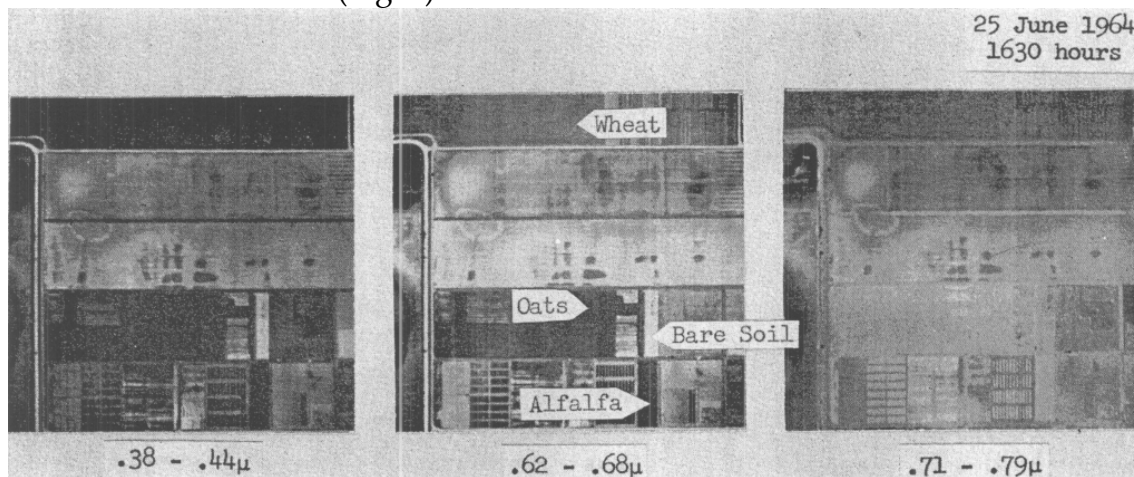


**Figura 1.** Imagen multispectral adquirida en 1964 sobre distintos cultivos (Hofjer, 1967).

En 1972 se lanzó el satélite *Earth Resources Technology Satellite (ERTS-1)* que posteriormente pasó a llamarse *Landsat-1*. Inicialmente era un satélite experimental con el que la NASA quería demostrar la operatividad de aplicaciones como la monitorización agrícola y medioambiental. El satélite incorporaba un sensor llamado MSS (*MultiSpectral Scanner*) que contaba con 4 bandas en el rango espectral del visible al infrarrojo cercano y una en el térmico, pensadas específicamente para la detección de propiedades de la vegetación. A partir de los primeros resultados obtenidos de las imágenes de Landsat-1 se especificaron, por un grupo de expertos, las características a implementar en los siguientes satélites de la misión (Hovis et al., 1975). De esa forma se definieron una serie de requisitos de bandas, resolución espacial, tiempo de revisita, etc, pensando fundamentalmente en aplicaciones agrícolas y de monitorización ambiental. El resultado fue la creación del sensor TM (*Thematic Mapper*) instalado a bordo de Landsat-4 y Landsat-5, y que sigue siendo operativo a día

de hoy en este último satélite. La idea original era contar con al menos dos satélites Landsat operativos al mismo tiempo que permitiesen un tiempo de revisita de 9 días, pensando en aplicaciones agrícolas.

Parecía por tanto que la teledetección iba a ofrecer grandes oportunidades a la comunidad agrícola, por lo que durante los años 70 y 80 se desarrollaron los programas LACIE (*Large Area Crop Inventory Experiment*) y posteriormente AgRISTARS (*Agriculture and Resources Inventory Surveys Through Aerospace Remote Sensing*) como un esfuerzo común entre distintos departamentos del gobierno estadounidense por desarrollar metodologías de teledetección que permitiesen identificar cultivos, así como determinar su estado o potencial producción a nivel regional (Bauer, 1985). El esquema de funcionamiento de estos programas tenía en cuenta el uso combinado de datos provenientes de Landsat, así como de otros sensores aerotransportados, que junto a datos meteorológicos daría lugar, tras un análisis, a informes para los gestores de fincas, agencias gubernamentales, etc (Figura 2). Estos programas permitieron definir las leyes físicas tras las relaciones entre las medidas espectrales y las propiedades biofísicas de la vegetación y el suelo.

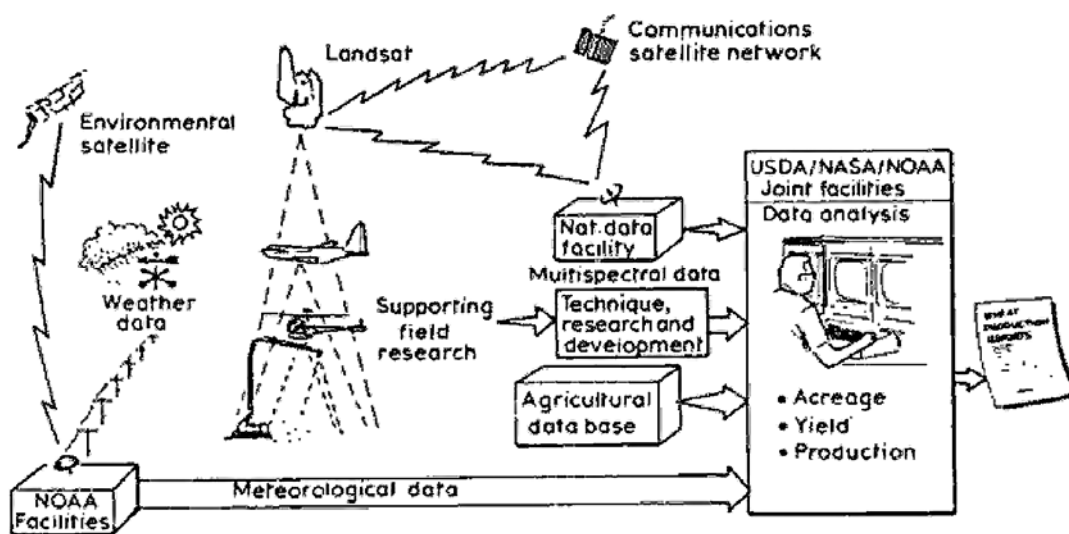


Figura 2. Esquema del flujo de datos de programa LACIE (Barret and Curtis, 1992).

Durante todos estos años se ha avanzado mucho en aspectos científicos de la teledetección y hay numerosos ejemplos de aplicaciones publicadas como la clasificación de cultivos (Erol & Akdeniz, 1996; Grignetti et al., 1997; PaxLenney & Woodcock, 1997), predicciones de cosecha y rendimiento (Clevers, 1997; Moran et al., 1995; Rasmussen, 1992; Tucker et al., 1980), estado de los cultivos (Blackmer et al., 1994; Boissard et al., 1993; Clevers et al., 1994; Potdar, 1993), detección de malas hierbas (Anderson et al., 1993; Everitt, 1995; Underwood et al., 2003), detección de enfermedades y deficiencias nutricionales (Adams et al., 1999; Adams et al., 2000; Malthus & Madeira, 1993) o estimación

de contenido de pigmentos fotosintéticos (Martin et al., 2007; Zarco-Tejada et al., 2005).

### ***Limitaciones actuales***

El principal problema que dificulta la aplicación práctica de muchas de las investigaciones desarrolladas en la última década y que se basan fundamentalmente en el uso de bandas espectrales estrechas, es que sus conclusiones no se han traducido en el diseño de los sensores instalados en los nuevos satélites comerciales de observación de la tierra. Dichos nuevos sensores se han limitado a incluir algunas de las bandas que ya incorporaba el sensor MSS del Landsat-1 en 1972, probablemente buscando la continuidad del programa Landsat en lugar de la innovación. Lamentablemente, la situación de las aplicaciones basadas en el térmico es aun más preocupante. Ninguno de los satélites comerciales lanzados recientemente cuenta con bandas en esa región del espectro y solamente quedan operativos a día de hoy Landsat 5 y ASTER como satélites que proporcionen imágenes térmicas de resolución media (120m y 90m respectivamente).

En una revisión de las oportunidades y limitaciones de la teledetección en el manejo de cultivos, Moran et al. (1997) afirmaba que los satélites de entonces carecían de unas bandas espectrales adecuadas, no tenían la suficiente resolución espacial para aplicaciones a nivel de parcela, contaban con tiempos de revisita inadecuados para el manejo agrícola y el tiempo de entrega de resultados era demasiado largo. También afirmaba que los sensores aerotransportados podrían evitar esas limitaciones pero no obstante presentaban otras limitaciones diferentes como la calibración radiométrica y geométrica de dichos sensores, la necesidad de correcciones atmosféricas o la complejidad de generar mosaicos a partir de las imágenes capturadas.

Actualmente los sensores aerotransportados hiperespectrales y multiespectrales pueden proporcionar resoluciones espaciales de 0.5 a 2 m y anchos de banda a partir de 2 nm en la región del espectro comprendida entre 300 y 2.500 nm. Existen numerosos trabajos que demuestran el uso de sensores como el *Compact Airborne Spectrographic Imager* (CASI) o el *Airborne Visible Infrared Imaging Spectrometer* (AVIRIS) para la estimación de parámetros de vegetación como contenido clorofílico (Cheng et al., 2006; Roberts, 1997; Serrano et al., 2000; Ustin et al., 1998; Zarco-Tejada et al., 2004), contenido de materia seca (Fourty & Baret, 1997; Jacquemoud et al., 1996; Riaño et al., 2005), y estimación de parámetros estructurales como fracción cubierta e índice de área foliar (LAI) (Haboudane et al., 2004). De igual modo existen trabajos publicados que hacen uso de sensores aerotransportados con bandas en el térmico como el *Airborne Hyperspectral Scanner* (AHS) y que han demostrado su utilidad en la detección de estrés hídrico en cultivos leñosos (Sepulcre-Cantó et al., 2005; 2006;

2007). Sin embargo, la aplicación de estos sensores sigue siendo casi exclusiva con fines científicos, sin producirse una transferencia de las metodologías desarrolladas a aplicaciones reales en el manejo de cultivos. Si bien la resolución espectral y espacial es adecuada, la complejidad de este tipo de sensores implica un tiempo de entrega de resultados demasiado largo. A eso hay que sumar la propia complejidad que conllevan las operaciones con aviones tripulados, que se traduce en problemas logísticos y un incremento de costes que hace que las posibles aplicaciones derivadas del uso de estos sensores no sean atractivas para los agricultores.

La llegada de los vehículos aéreos no tripulados (UAV) al mundo civil podría evitar algunas de las limitaciones que presentan los aviones tripulados. Por ese motivo, la comunidad científica pronto adoptó esta tecnología y la NASA fue pionera en el uso de UAVs solares (Figura 3) en campos de café en Hawaii (Herwitz et al., 2003; 2004) o el RCATS/APV-3 sobre viñedos en California (Johnson et al., 2003). La evolución en la microelectrónica y la miniaturización de elementos como los receptores GPS o sensores inerciales, ambos necesarios para el desarrollo de sistemas de navegación autónoma (autopilotos) para este tipo de vehículos, ha provocado que se desarrollen autopilotos comerciales de bajo peso que puedan ser integrados en vehículos aéreos cada vez más pequeños y sencillos de operar. De igual modo, en los últimos años se ha producido un gran avance en el desarrollo de nuevos sensores de imagen de alta resolución, promovido especialmente por la electrónica de consumo. También, gracias al desarrollo de sensores de imagen térmica, actualmente existen en el mercado cámaras térmicas comerciales sin necesidad de refrigeración a precios asequibles para ciertas aplicaciones. Como consecuencia, varios autores han publicado trabajos en los que usando este tipo de cámaras en pequeños aviones o helicópteros similares a los usados en radio control, han demostrado su viabilidad como plataformas para la adquisición de imágenes (Ambrosia et al., 2003; Esposito, 2007; Haitao & Lei, 2007; Lambers et al., 2007; Sugiura et al., 2005; Zhao et al., 2006).



**Figura 3.** El UAV solar Pathfinder de la NASA volando sobre campos de café en Hawaii. Cortesía NASA.

La principal limitación de este tipo de plataformas es que para hacer uso de las metodologías de teledetección cuantitativa antes mencionadas, es necesario el desarrollo de metodologías de calibración radiométrica, así como las correcciones atmosféricas necesarias para la obtención de datos validados de reflectancia y temperatura de superficie. Igual atención hay que prestar a aspectos como la calibración geométrica de la óptica y los sensores que permitan aplicar metodologías fotogramétricas para la posterior obtención de mosaicos georreferenciados.

La principal ventaja que permitiría el uso de estas plataformas de teledetección es que si se consiguen superar dichas limitaciones, podríamos estar ante una nueva era de la teledetección en la que la visión de Jackson podría hacerse realidad. La superación de esas limitaciones y el desarrollo de nuevas metodologías y aplicaciones para la detección del estado hídrico de la vegetación, que hagan uso de las ventajas de este tipo de plataformas, ha sido una de las principales justificaciones de la presente Tesis Doctoral.

### ***Determinación del estado hídrico de la vegetación***

El sector agrícola es, con mucho, el que utiliza la mayor cantidad de agua a nivel mundial. Más de las dos terceras partes del agua extraída de los ríos, lagos y acuíferos del mundo se utilizan para el riego. Ante el aumento de la competencia con otros sectores, los conflictos, la escasez, el desperdicio, la utilización excesiva y la degradación de los recursos hídricos, los responsables políticos están volviendo cada vez más la vista hacia la agricultura (FAO, 1993). Las ciudades y las industrias pueden pagar más por el agua, y su tasa de rentabilidad económica por unidad de agua es más alta que la del sector agrícola. Por primera vez en la historia de muchos países, la agricultura se está viendo obligada a ceder agua de forma permanente en favor de usos más valiosos en las ciudades e industrias.

Un mejor uso del agua en agricultura resultará no sólo en un ahorro económico, sino en la posibilidad de cultivar una mayor extensión y por lo tanto obtener una mayor producción. Existen numerosas técnicas para posibilitar un uso más eficiente del agua de riego y obtener una mayor producción por unidad de agua usada, o sea de mejorar la productividad del agua. Éstas abarcan desde la mejora de los sistemas de riego hasta el riego deficitario controlado (RDC) que consiste en aplicar una menor cantidad de agua a los cultivos durante etapas clave del cultivo en las que un estrés moderado no influye negativamente en el rendimiento del cultivo o en la calidad de la cosecha (English, 1990). Con estas técnicas de RDC es posible ahorrar hasta un 40% de agua según el tipo de cultivo en el que se empleen (Domingo et al., 1996; Fereres & Soriano, 2007). Para controlar el nivel de estrés del cultivo durante el período de riego deficitario es necesario monitorizar el estado hídrico del cultivo de forma muy precisa al objeto de evitar que se exceda el nivel programado de estrés, lo que influiría negativamente en la cosecha (Hsiao et al., 1976). La forma más aceptada de medir el estado hídrico de las plantas es la medida de potencial hídrico del xilema en hoja o tallo, mediante el uso de bombas de presión (Hsiao, 1990). Otra medida aceptada es la conductancia estomática medida mediante el uso de porómetros de difusión y que indica el nivel de transpiración foliar. Sin embargo, ambas medidas son a escala foliar, resultan laboriosas y requieren de mucho tiempo para caracterizar espacialmente el estrés, lo que no permite su uso generalizado.

La importancia que tiene la teledetección en la estimación del estado hídrico de un cultivo es que al hacer uso de imágenes es posible determinar la distribución espacial de los distintos niveles de estrés, a diferencia de las medidas puntuales arriba mencionadas.

Desde el punto de vista de la teledetección se podría decir que hay dos tipos de metodologías fundamentales para la detección de estrés hídrico: a) aquellas que hacen uso del uso del térmico y que se basan en detectar el aumento de temperatura que se observa al producirse un cierre estomático parcial y por lo tanto, una reducción del flujo de calor latente; y b) aquellas que hacen uso de observaciones en la región del espectro desde el visible al infrarrojo medio.

Las metodologías de detección de estrés hídrico mediante el uso de la temperatura de superficie tienen su origen con el desarrollo de los primeros sensores de infrarrojo térmico (IRT) durante los años 60 (Fuchs & Tanner, 1966; Idso et al., 1978; Jackson et al., 1977; Tanner, 1963). Inicialmente, se propuso usar como indicador de estrés la diferencia de la temperatura del cultivo y la del aire (Jackson et al., 1977), si bien pronto se puso de manifiesto que la temperatura de la cubierta se veía afectada por otros factores ambientales tales como la humedad relativa, la radiación o el viento. Es por esto por lo que surgió la necesidad de normalizar dicha medida teniendo en cuenta factores como la humedad relativa (Idso et al., 1981). Así surgió el *Crop Water Stress Index* (CWSI), que si bien empezó siendo una metodología empírica que dependía de la determinación de líneas base dependientes del cultivo y del lugar donde se desarrollaban, pronto dio lugar a una formulación analítica (Jackson et al., 1981). Aunque el uso del CWSI tuvo bastante difusión como observaciones puntuales, realizadas con termómetros de infrarrojos portátiles, la aplicación del CWSI a nivel de imagen ha estado limitada por la resolución espacial de los sensores disponibles hasta este momento.

Todas estas técnicas se basan fundamentalmente en el balance energético y en el reparto de la energía neta (la absorbida por la vegetación) entre calor sensible (temperatura), calor latente (evaporación) y almacenamiento en el suelo o vegetación. Usando ese balance de energía se han desarrollado modelos que permiten obtener estimaciones de la evapotranspiración (ET) a partir de imágenes satélites de Landsat. Modelos como SEBAL (Bastiaanssen et al., 1998) o METRIC (Allen et al., 2007) se encuentran actualmente operativos y dan resultados aceptables en cultivos herbáceos de extensiones suficientes para la resolución de los sensores empleados (120m en el caso de Landsat 5). Sin embargo estos modelos parecen no comportarse correctamente en cultivos heterogéneos para los que se han desarrollado modelos de varias componentes que intentan separar la temperatura de la vegetación de la del suelo en píxeles agregados usando observaciones multiangulares (Anderson et al., 1997) o combinados con índices de vegetación (Moran et al., 1994).

Otras técnicas para cuantificar el estado hídrico de los cultivos se basan en la estimación de la conductancia foliar a partir de la temperatura de

superficie (Smith, 1988). Algunas de estas metodologías se han aplicado a nivel de imagen usando imágenes térmicas de alta resolución obtenidas desde grúas (Jones et al., 2002; Leinonen et al., 2006; Lhomme & Monteny, 2000). Recientemente, el uso de imágenes térmicas obtenidas con sensores aerotransportados y su aplicación a la detección de estrés hídrico en cultivos leñosos como olivar (Sepulcre-Cantó et al., 2006; Sepulcre-Cantó et al., 2007) hacen pensar que estas metodologías también se podrían implementar para este tipo de sensores, permitiendo la obtención de mapas del estrés hídrico a nivel de copas de árboles individuales, es decir, a resolución submétrica.

En cuanto a las metodologías basadas en la parte visible/infrarroja del espectro, hay diversas aproximaciones que van desde la monitorización de cambios estructurales en la vegetación, tales como marchitez o pérdida de área foliar (Bradford & Hsiao, 1982; Wolfe et al., 1983), hasta la estimación de la pérdida de constituyentes bioquímicos como la clorofila (Björkman & Powles, 1982) o agua (Gao, 1996; Peñuelas et al., 1993; Peñuelas et al., 1997). Sin embargo, todos estos efectos ocurren cuando ya se ha instalado en la planta un elevado nivel de estrés hídrico y los síntomas llegan incluso a ser visibles a simple vista. Por lo tanto, se hace deseable el uso de otras metodologías que proporcionen una detección del estrés de forma más precoz, idealmente en un estado pre-visual. En este sentido, se proponen indicadores como el *Photochemical Reflectance Index* (PRI) (Gamon et al., 1992), un índice que es sensible a la absorción por xantofilas y su variación bajo condiciones de estrés hídrico (Peguero-Pina et al., 2008; Suárez et al., 2008; Suárez et al., 2009; Thenot et al., 2002). De igual modo, la detección de fluorescencia clorofílica en condiciones de iluminación natural fue propuesta como un indicador pre-visual de estrés en vegetación (Bolhar-Nordenkamp et al., 1989; McFarlane et al., 1980) ya que se observa una alta correlación entre la fluorescencia en estado estacionario ( $F_s$ ) y la conductancia estomática (Flexas et al., 1999; Flexas et al., 2000; Flexas et al., 2002; Moya et al., 2004). Esto se debe a que los sistemas fotosintéticos de las plantas cuentan con sistemas de protección ante el exceso de radiación. Una parte de ese exceso de radiación se disipa en forma de calor, mientras que otra parte produce una reemisión de luz en longitudes de onda mayores que las de excitación. Los picos de emisión están centrados a 690 y 740 nm. En los estados iniciales de estrés hídrico, la planta aumenta la disipación de energía por medio de calor, reduciendo la  $F_s$  (Yahyaoui et al., 1998). De ese modo, la detección de la reducción de la  $F_s$  podría servir para determinar el grado de estrés.

El principal problema para la detección de la  $F_s$  desde el aire o el espacio es que la señal de fluorescencia emitida es muy pequeña (alrededor del 3% de la radiancia) y está mezclada con la reflectancia de la superficie, además de estar influenciada por efectos atmosféricos. El resultado es que se produce un ligero

incremento en la radiancia detectada y por lo tanto en la reflectancia aparente de la cubierta. Una de las técnicas empleadas para la detección de la  $F_s$  es observar aquellas regiones del espectro en las que se produce una gran absorción atmosférica, conocidas como líneas de Fraunhofer. En esas bandas, la irradiancia que llega a la superficie es muy pequeña, por lo que la radiancia reflejada provendrá en su mayor parte de la fluorescencia (Figura 4). Se denomina a este método “*in-filling*” o rellenado espectral y Pérez-Priego et al. (2005) demostró que usando la línea del  $O_2$ -A, podía ser usado en condiciones de iluminación natural para la detección de estrés hídrico en olivar, mediante el empleo de espectrorradiómetros subnanométricos (0.065 nm FWHM, *full-width at half-maximum*).

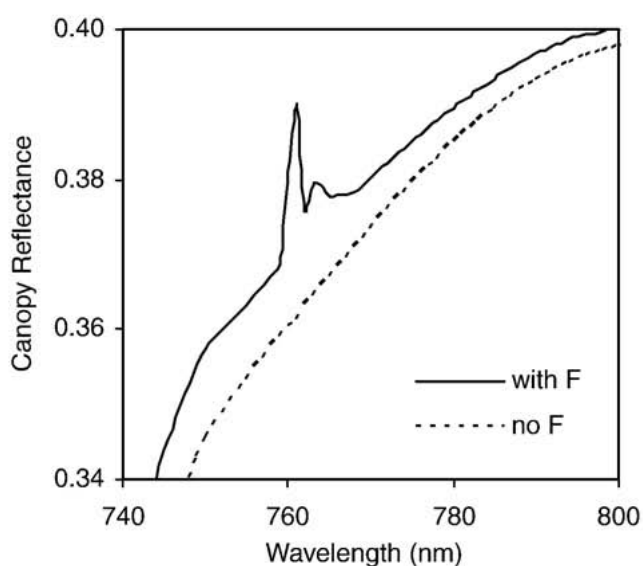


**Figura 4.** Comparación de la reflectancia de una cubierta fluorescente y otra no fluorescente. Se puede apreciar el pico en la región de absorción de  $O_2$ .

A nivel de imagen con sensores aerotransportados, Maier et al. (2002) y Zarco-Tejada et al. (2004) propusieron el uso de esta técnica para la detección de la señal de la fluorescencia en condiciones naturales de iluminación usando la reflectancia aparente a partir de sensores como el *Reflective Optics System Imaging Spectrometer* (ROSIS) y el *Compact Airborne Spectrographic Imager* (CASI), con bandas de 7.5 nm FWHM. Sin embargo, en esos trabajos no se llevó a cabo una validación de campo para confirmar la hipótesis, objetivo que se ha llevado a cabo en esta tesis doctoral en el contexto de detección de estrés hídrico.

## **Presentación del trabajo**

En el desarrollo de esta Tesis Doctoral podemos diferenciar dos partes importantes: i) una parte técnica que conlleva el trabajo realizado para desarrollar una plataforma de teledetección basada en un vehículo aéreo no tripulado, y que requirió la puesta a punto de todas aquellas metodologías de calibración, generación de mosaicos, etc, que permitiesen obtener imágenes de calidad para su uso en teledetección cuantitativa; y, ii) una parte de aplicación y, por lo tanto, del uso de metodologías existentes a partir de imágenes obtenidas con la plataforma no tripulada desarrollada, así como la investigación en el desarrollo de nuevas metodologías de cuantificación del estado hídrico de la vegetación, que serían posible gracias a las características específicas de esta plataforma. En este caso, se proponen dos metodologías de detección de estrés, una basada en las imágenes obtenidas con la cámara multiespectral y que emplea de la detección de fluorescencia clorofílica gracias al uso de bandas de 1.6 nm FWHM de ancho, y a la alta resolución espacial; y otra metodología basada en el térmico que permite generar mapas de CWSI, así como cuantificar la conductancia de la cubierta usando imágenes térmicas de alta resolución espacial y datos meteorológicos.

El trabajo se describe por lo tanto en tres capítulos que se resumen a continuación.

**En el Primer Capítulo** se expone el desarrollo de una plataforma de teledetección basada en un vehículo aéreo no tripulado con capacidad de obtención de imágenes multiespectrales en el rango de 400-1000nm y térmicas en el rango de 8-14 $\mu$ m, con resoluciones espaciales de 20cm y 40cm respectivamente. Se explican los diversos aspectos, desde la integración de los sensores de imagen en el vehículo aéreo hasta el desarrollo e implementación de todas aquellas metodologías necesarias para obtener una calibración radiométrica y geométrica de los sensores, pasando por la corrección atmosférica y posterior proceso fotogramétrico de obtención de mosaicos georreferenciados. Para la validación de la plataforma se han aplicado diversas metodologías de teledetección cuantitativa, ya publicadas, para la obtención de parámetros biofísicos de la vegetación, tales como contenido clorofílico, índice de área foliar, indicadores de estrés previsual basados en el *Photochemical Reflectance Index* (PRI) y temperatura de superficie.

**En el Segundo Capítulo** se presenta la posibilidad de obtener imágenes de fluorescencia de vegetación usando imágenes multiespectrales de alta resolución espacial con bandas de 1.6nm FWHM de ancho. Para ello se utiliza el método *in-filling* usando la banda de absorción de O<sub>2</sub>-A. En este capítulo se hace uso de modelos de transferencia radiativa para comparar metodologías

publicadas de detección de fluorescencia a nivel de imagen y cómo afectan diversos parámetros como el LAI o el contenido de clorofila. La fluorescencia obtenida de las imágenes aéreas se ha validado mediante medidas de campo en olivar, melocotonero y cítricos, así como su conexión con las medidas de estrés hídrico.

**En el Tercer Capítulo** se propone una metodología basada en el uso de imágenes térmicas de alta resolución espacial para la determinación de la conductancia de la cubierta ( $G_c$ ) y del *Crop Water Stress Index* (CWSI) en cultivos arbóreos. Dichas estimaciones permiten obtener mapas de la variabilidad espacial de estrés hídrico, a la vez que sirven de base para la cuantificación de las necesidades hídricas del cultivo, y por lo tanto para la planificación de riegos. La metodología presentada se basa en la hipótesis de que la alta resolución espacial permite separar los distintos componentes que intervienen en el balance de energía de un cultivo heterogéneo, y por lo tanto se puede estimar la temperatura de la vegetación pura. El modelo hace uso de distintos modelos físicos que permite estimar parámetros necesarios en el balance de energía como la radiación neta y la resistencia aerodinámica, lo que evita el uso de superficies de referencia que supondría una metodología menos aplicable de forma práctica.

Cada uno de estos capítulos ha dado lugar a un artículo científico que ha sido enviado a revistas internacionales de reconocido prestigio en el área. Tras la consecuente revisión, han sido aceptados y publicados de forma definitiva, según la siguiente relación:

2009. Berni, J.A.J., Zarco-Tejada, P.J., Suarez, L., Fereres, E., **Thermal and Narrow-band Multispectral Remote Sensing for Vegetation Monitoring from an Unmanned Aerial Vehicle.** *IEEE Transactions on Geoscience and Remote Sensing*, 47, (3), 722-738.

2009. Zarco-Tejada, P.J., Berni, J.A.J., Suárez, L., Sepulcre-Cantó, G., Morales, F., Miller, J.R., **Imaging Chlorophyll Fluorescence from an Airborne Narrow-Band Multispectral Camera for Vegetation Stress Detection.** *Remote Sensing of Environment*, 113, 1262-1275.

2009. Berni, J.A.J., Zarco-Tejada, P.J., Sepulcre-Cantó, G., Fereres, E., Villalobos, F.J., **Mapping stomatal conductance and CWSI in olive orchards using high resolution thermal remote sensing imagery.** *Remote Sensing of Environment*, 113, 2380-2388.

## **Referencias**

- Adams, M.L.; Norvell, W.A.; Philpot, W.D.; Peverly, J.H. (2000) Toward the discrimination of manganese, zinc, copper, and iron deficiency in 'Bragg' soybean using spectral detection methods. *Agronomy Journal*, 92 (2), 268-274.
- Adams, M.L.; Philpot, W.D.; Norvell, W.A. (1999) Yellowness index: an application of spectral second derivatives to estimate chlorosis of leaves in stressed vegetation. *International Journal of Remote Sensing*, 20 (18), 3663-3675.
- Allen, R.; Tasumi, M.; Trezza, R. (2007) Satellite-Based energy balance for Mapping Evapotranspiration with Internalized Calibration (METRIC) - Model. *Journal of Irrigation and Drainage Engineering*, 133 (4), 380-394.
- Ambrosia, V.; Wegener, S.; Sullivan, D.; Buechel, S.; Dunagan, S.; Brass, J. et al. (2003) Demonstrating UAV-acquired real-time thermal data over fires. *Photogrammetric Engineering and Remote Sensing*, 69 (4), 391-402.
- Anderson, G.; Everitt, J.; Richardson, A.; Escobar, D. (1993) Using satellite data to map false broomweed (*Ericameria austrotexana*) infestations on south Texas rangelands. *Weed Technology*, 7 (4), 865-871.
- Anderson, M.; Norman, J.; Diak, G.; Kustas, W.; and Mecikalski, J. (1997) A two-source time-integrated model for estimating surface fluxes using thermal infrared remote sensing. *Remote Sensing of Environment*, 60, 195-216.
- Barret, E.C., Curtis, L.F. (1993). Introduction to Environmental Remote Sensing. 3rd ed., 1993. Ed. Chapman and Hall. London, UK. p 335
- Bastiaanssen, W.; Menenti, M.; Feddes, R.; Holtslag, A. (1998) A remote sensing surface energy balance algorithm for land (SEBAL): 1. Formulation. *Journal of Hydrology*, 212-213 (1-4), 198-212.
- Bauer, M. (1985) Spectral inputs to crop identification and condition assessment. *Proceedings of the IEEE*, 73 (6), 1071-1085.
- Bauer, M.; Mroczynski, R.; MacDonald, R.; Hoffer, R. (1971) Detection of southern corn leaf blight using color infrared aerial photography. In Proc. Third Biennial Workshop on color Aerial Photography in the Plant Sciences, Gainesville Florida, 114-126.
- Björkman, O.; Powles, S. (1982) Inhibition of photosynthetic reactions under water stress: Integration with light level. *Planta*, 161, 490-504.
- Blackmer, T.M.; Schepers, J.S.; Varvel, G.E. (1994) Light reflectance compared with other nitrogen stress measurements in corn leaves. *Agronomy Journal*, 86 (6), 934-938.
- Boissard, P.; Pointel, J.G.; Huet, P. (1993) Reflectance, green leaf-area index and ear hydric status of wheat from anthesis until maturity. *International Journal of Remote Sensing*, 14 (14), 2713-2729.
- Bolhar-Nordenkamp, H.; Long, S.; Baker, N.; Oquist, G.; Schreiber, U.; Lechner, E. (1989) Chlorophyll fluorescence as a probe of the photosynthetic

competence of leaves in the field: A review of current instrumentation. *Functional Ecology*, 3 (4), 497-514.

Bradford K, Hsiao T (1982) Physiological responses to moderate water stress. In: Lange O, Nobel P, Osmond C, Ziegler H, editors. *Encyclopedia of plant physiology*. Springer. pp. 263-324.

Cheng, Y.B.; Riano, D.; Zarco-Tejada, P.J.; Ustin, S.L. (2006) Canopy water content estimates with AVIRIS imagery and MODIS reflectance products - art. no. 629809, 6298, 29809-29809.

Clevers, J.G.P.W. (1997) A simplified approach for yield prediction of sugar beet based on optical remote sensing data. *Remote Sensing of Environment*, 61 (2), 221-228.

Clevers, J.G.P.W.; Buker, C.; Vanleeuwen, H.J.C.; Bouman, B.A.M. (1994) A framework for monitoring crop growth by combining directional and spectral Remote-Sensing information. *Remote Sensing of Environment*, 50 (2), 161-170.

Domingo, R.; Ruiz-Sánchez, M.; Sánchez-Blanco, M.; Torrecillas, A. (1996) Water relations, growth and yield of Fino lemon trees under regulated deficit irrigation. *Irrigation Science*, 16, 115-123.

English, M. (1990) Deficit irrigation. I. Analytical framewrok. *Journal of Irrigation and Drainage Engineering*, 116, 399-412.

Erol, H.; Akdeniz, F. (1996) A multispectral classification algorithm for classifying parcels in an agricultural region. *International Journal of Remote Sensing*, 17 (17), 3357-3371.

Esposito, F.; Rufino, G.; Moccia, A. (2007) 1st mini-UAV integrated hyperspectral/thermal electro-optical payload for forest fire risk management. *American Institute of Aeronautics and Astronautics, Infotech@Aerospace*, 1, 653-665.

Everitt, J.H.; Anderson, G.L.; Escobar, D.E.; Davis, M.R.; Spencer, N.R.; Andrascik, R.J. (1995) Use of remote sensing for detecting and mapping leafy spurge (*Euphorbia esula*). *Weed Technology*, 9 (3), 599-609.

FAO (1993) Estado mundial de la agricultura y la alimentación. FAO. p.

Fereres, E.; Soriano, M. (2007) Deficit irrigation for reducing agricultural water use. *J. Exp. Bot.*, 58 (2), 147-159.

Flexas, J.; Briantais, J.; Cerovic, Z.; Medrano, H.; Moya, I. (2000) Steady-state and maximum chlorophyll fluorescence responses to water stress in grapevine leaves: A new remote sensing system. *Remote Sensing of Environment*, 73 (3), 283-297.

Flexas, J.; Escalona, J.; Evain, S.; Gulías, J.; Moya, I.; Osmond, C. et al. (2002) Steady-state chlorophyll fluorescence (Fs) measurements as a tool to follow variations of net CO<sub>2</sub> assimilation and stomatal conductance during water-stress in C<sub>3</sub> plants. *Physiologia Plantarum*, 114 (2), 231-240.

Flexas, J.; Escalona, J.; Medrano, H. (1999) Water stress induces different levels of photosynthesis and electron transport rate regulation in grapevines. *Plant, Cell and Environment*, 22 (1), 39-48.

Fourty, T.; Baret, F. (1997) Vegetation water and dry matter contents estimated from top-of-the-atmosphere reflectance data: A simulation study. *Remote Sensing of Environment*, 61 (1), 34-45.

Fuchs, M.; Tanner, C.B. (1966) Infrared Thermometry of Vegetation. *Agronomy Journal*, 58, 297-601.

Gamon, J.; Penuelas, J.; Field, C. (1992) A narrow-waveband spectral index that tracks diurnal changes in photosynthetic efficiency. *Remote Sensing of Environment*, 41 (1), 35-44.

Gao, B. (1996) NDWI - A normalized difference water index for remote sensing of vegetation liquid water from space. *Remote Sensing of Environment*, 58, 257-266.

Grignetti, A.; Salvatori, R.; Casacchia, R.; Manes, F. (1997) Mediterranean vegetation analysis by multi-temporal satellite sensor data. *International Journal of Remote Sensing*, 18 (6), 1307-1318.

Haboudane, D.; Miller, J.; Pattey, E.; Zarco-Tejada, P.; Strachan, I. (2004) Hyperspectral vegetation indices and novel algorithms for predicting green LAI of crop canopies: Modeling and validation in the context of precision agriculture. *Remote Sensing of Environment*, 90 (3), 337-352.

Haitao, X.; Lei, T. (2007) An autonomous helicopter system for aerial image collection. In *2007 ASABE Annual International Meeting, Technical Papers*, Minneapolis, MN, 2.

Herwitz, S.; Dunagan, S.; Sullivan, D.; Higgins, R.; Johnson, L.; Zheng, J. et al. (2003) Solar-powered UAV mission for agricultural decision support. In *Proc. 2003 IGARSS: Learning From Earth's Shapes and Colours*, 3, 1692-1694.

Herwitz, S.; Johnson, L.; Dunagan, S.; Higgins, R.; Sullivan, D.; Zheng, J. et al. (2004) Imaging from an Unmanned Aerial Vehicle: Agricultural surveillance and decision support. *Computers and Electronics in Agriculture*, 44 (1), 49-61.

Hofjer, R.M. (1967) Interpretation of Remote Multispectral Imagery of Agricultural Crops. *Research Bulletin of the Laboratory for Agricultural Remote Sensing*, 1 (831), 1-36.

Hovis, W.; Nichols, J.; Potter, A.; Thomson, F. (1975) Landsat - D Thematic Mapper Technical Working Group. Final Report. NASA.

Hsiao, T.; Fereres, E.; Acevedo, E.; Henderson, D. (1976) Water stress and dynamics of growth and yield of crops. water and plant life: problems and modern approaches. Springer.

Hsiao, T.C. (1990) Measurements of plant water status. American Society of Agronomy, Madison (EUA); Crop Science Society of America, Madison (EUA); Soil Science Society of America, Madison (EUA).

Idso, S.; Jackson, R.; Pinter P.J., J.; Reginato, R.; Hatfield, J. (1981) Normalizing the stress-degree-day parameter for environmental variability. *Agricultural Meteorology*, 24 (1), 45-55.

Idso, S.; Jackson, R.; Reginato, R. (1978) Extending the 'degree-day' concept of plant phenological development to include water stress effects. *Ecology*, 59, 431-433.

Jackson, R.D.; Reginato, R.; Idso, S. (1977) Wheat canopy temperature: A practical tool for evaluating water requirements. *Water Resources Research*, 13 (3), 651-656.

Jackson, R.D. (1984) Remote sensing of vegetation characteristics for farm management. *Sixth Critical Reviews of Technology Series* of the Society of Photo-optical Instrumentation Engineers (SPIE), 475, 81-96.

Jackson, R.D.; Idso, S.B.; Reginato, R.J.; Pinter, P.J. (1981) Canopy temperature as a crop water-stress indicator. *Water Resources Research*, 17 (4), 1133-1138.

Jackson, R.D.; Reginato, R.J.; Idso, S.B. (1977) Wheat Canopy Temperature - Practical Tool for Evaluating Water Requirements. *Water Resources Research*, 13 (3), 651-656.

Jacquemoud, S.; Ustin, S.; Verdebout, J.; Schmuck, G.; Andreoli, G.; Hosgood, B. (1996) Estimating leaf biochemistry using the PROSPECT leaf optical properties model. *Remote Sensing of Environment*, 56 (3), 194-202.

Johnson, L.; Herwitz, S.; Dunagan, S.; Lobitz, B.; Sullivan, D.; Slye, R. (2003) Collection of ultra high spatial and spectral resolution image data over California vineyards with a small UAV. In *Int'l Symp. Rem. Sens. Environ.* 10-14 Nov., Honolulu, HI. 2003, 10-14.

Jones, H.G.; Stoll, M.; Santos, T.; Sousa, C.D.; Chaves, M.M.; Grant, O.M. (2002) Use of infrared thermography for monitoring stomatal closure in the field: Application to grapevine. *Journal of Experimental Botany*, 53 (378), 2249-2260.

Keegan, H.; Schleter, J.; Hall, W. (1956) Spectrophotometric and colorimetric study of diseased and rust resisting cereal crops. *National Bureau of Standards Report*, 4591.

Lambers, K.; Eisenbeiss, H.; Sauerbier, M.; Kupferschmidt, D.; Gaisecker, T.; Sotoodeh, S. et al. (2007) Combining photogrammetry and laser scanning for the recording and modelling of the Late Intermediate Period site of Pinchango Alto, Palpa, Peru. *J. Archaeol. Sci.*, 34 (10), 1702-1712.

Leinonen, I.; Grant, O.M.; Tagliavia, C.P.P.; Chaves, M.M.; Jones, H.G. (2006) Estimating stomatal conductance with thermal imagery. *Plant, Cell and Environment*, 29, 1508-1518.

Lhomme, J.P.; Monteny, B. (2000) Theoretical relationship between stomatal resistance and surface temperatures in sparse vegetation. *Agricultural and Forest Meteorology*, 104, 119-131.

Maier, S.; Günther, K.; Stellmes, M. (2002) Remote sensing and modelling of solar induced fluorescence. In *1st Workshop on Remote Sensing of Solar Induced Vegetation Fluorescence*, Noordwijk, Netherlands.

Malthus, T.J.; Madeira, A.C. (1993) High-resolution spectroradiometry - spectral reflectance of field bean-leaves infected by botrytis-fabae. *Remote Sensing of Environment*, 45 (1), 107-116.

Martin, P.; Zarco-Tejada, P.; Gonzalez, M.; Berjon, A. (2007) Using hyperspectral remote sensing to map grape quality in 'Tempranillo' vineyards affected by iron deficiency chlorosis. *Vitis*, 46 (1), 7-14.

McFarlane, J.; Watson, R.; Theisen, A.; Jackson, R.; Ehrlert, W. (1980) Plant stress detection by remote measurement of fluorescence. *Applied Optics*, 19, 3287-3289.

Moran, M.S.; Clarke, T.; Inoue, Y.; Vidal, A. (1994) Estimating crop water deficit using the relation between surface-air temperature and spectral vegetation index. *Remote Sensing of Environment*, 49 (3), 246-263.

Moran, M.S.; Maas, S.; Pinter Jr, P. (1995) Combining remote sensing and modeling for estimating surface evaporation and biomass production. *Remote Sensing Reviews*, 12 (3-4), 335-353.

Moran, M.S.; Inoue, Y.; Barnes, E.M. (1997) Opportunities and limitations for image-based remote sensing in precision crop management. *Remote Sensing of Environment*, 61 (3), 319-346.

Moya, I.; Camenen, L.; Evain, S.; Goulas, Y.; Cerovic, Z.; Latouche, G. et al. (2004) A new instrument for passive remote sensing: 1. Measurements of sunlight-induced chlorophyll fluorescence. *Remote Sensing of Environment*, 91 (2), 186-197.

PaxLenney, M.; Woodcock, C.E. (1997) The effect of spatial resolution on the ability on to monitor the status of agricultural lands. *Remote Sensing of Environment*, 61 (2), 210-220.

Peguero-Pina, J.; Morales, F.; Flexas, J.; Gil-Pelegrín, E.; Moya, J. (2008) Photochemistry, remotely sensed physiological reflectance index and depoxidation state of the xanthophyll cycle in *Quercus coccifera* under intense drought. *Oecologia*, 1 (156), 1-11.

Perez-Priego, O.; Zarco-Tejada, P.; Miller, J.; Sepulcre-Cantó, G.; Fereres, E. (2005) Detection of water stress in orchard trees with a high-resolution spectrometer through chlorophyll fluorescence in-filling of the O<sub>2</sub>-A band. *IEEE Transactions on Geoscience and Remote Sensing*, 43 (12), 2759-2769.

Peñuelas, J.; Filella, I.; Biel, C.; Serrano, L.; Save, R. (1993) The reflectance at the 950-970 nm region as an indicator of plant water status. *International Journal of Remote Sensing*, 14 (10), 1887-1905.

Peñuelas, J.; Piñol, J.; Ogaya, R.; Filella, I. (1997) Estimation of plant water concentration by the reflectance Water Index WI (R900/R970). *International Journal of Remote Sensing*, 18 (13), 2869-2875.

Potdar, M.B. (1993) Sorghum yield modeling based on crop growth-parameters determined from visible and near-IR channel NOAA AVHRR Data. *International Journal of Remote Sensing*, 14 (5), 895-905.

Rasmussen, M.S. (1992) Assessment of millet yields and production in Northern Burkina-Faso using integrated NDVI From the AVHRR. *International Journal of Remote Sensing*, 13 (18), 3431-3442.

Riaño, D.; Vaughan, P.; Chuvieco, E.; Zarco-Tejada, P.; Ustin, S. (2005) Estimation of fuel moisture content by inversion of radiative transfer models to simulate equivalent water thickness and dry matter content: Analysis at leaf and canopy level. *IEEE Transactions of Geoscience and Remote Sensing*, 43 (4), 821-826.

Roberts, D. A. and Green, R. O. and Adams, J. B. (1997) Temporal and spatial patterns in vegetation and atmospheric properties from AVIRIS. *Remote Sensing of Environment*, 62 (3), 223-240.

Sepulcre-Cantó, G.; Zarco-Tejada, P.; Jiménez-Munoz, J.; Sobrino, J.; Soriano, M.; Fereres, E. et al. (2007) Monitoring yield and fruit quality parameters in open-canopy tree crops under water stress. Implications for ASTER. *Remote Sensing of Environment*, 107 (3), 455-470.

Sepulcre-Cantó, G.; Zarco-Tejada, P.; Jiménez-Munoz, J.; Sobrino, J.; de Miguel, E.; Villalobos, F. (2006) Detection of water stress in an olive orchard with thermal remote sensing imagery. *Agricultural and Forest Meteorology*, 136 (1/2), 31-44.

Sepulcre-Cantó, G.; Zarco-Tejada, P.J.; Sobrino, J.A.; Jimenez-Munoz, J.C.; Villalobos, E. (2005) Spatial variability of crop water stress in an olive grove with high-spatial thermal remote sensing imagery. In *5th European Conference on Precision Agriculture (5ECPA), Precision Agriculture '05 - J.V. Stafford (Ed.)*, Wageningen Academic, pp 267-272.

Serrano, L.; Ustin, S.L.; Roberts, D.A.; Gamon, J.A.; Penuelas, J. (2000) Deriving water content of chaparral vegetation from AVIRIS data. *Remote Sensing of Environment*, 74 (3), 570-581.

Smith, R.C.G. (1988) Inferring stomatal resistance of sparse crops from infrared measurements of foliage temperature. *Agricultural and Forest Meteorology*, 42, 183-198.

Sugiura, R.; Noguchi, N.; Ishii, K. (2005) Remote-sensing technology for vegetation monitoring using an unmanned helicopter. *Biosystems Engineering*, 90 (4), 369-379.

Suárez, L.; Zarco-Tejada, P.; Berni, J.A.J.; Gozalez-Dugo, V.; Fereres, E. (2009) Modelling PRI for water stress detection using radiative transfer models. *Remote Sensing of Environment*, 113, 730-744.

Suárez, L.; Zarco-Tejada, P.; Sepulcre-Cantó, G.; Pérez-Priego, O.; Miller, J.; Jimenez-Muñoz, J. (2008) Assessing canopy PRI for water stress detection with diurnal airborne imagery. *Remote Sensing of Environment*, 112, 560-575.

Tanner, C.B. (1963) Plant Temperatures. *Agronomy Journal*, 55, 210-211.

Thenot, F.; Méthy, M.; Winke, T. (2002) The photochemical reflectance index (PRI) as a water-stress index. *Journal of Remote Sensing*, 23 (23), 5135-5139.

Tucker, C.J.; Holben, B.N.; Elgin, J.H.; McMurtrey, J.E. (1980) Relationship of spectral data to grain-yield variation. *Photogrammetric Engineering and Remote Sensing*, 46 (5), 657-666.

Underwood, E.; Ustin, S.; DiPietro, D. (2003) Mapping nonnative plants using hyperspectral imagery. *Remote Sensing of Environment*, 86 (2), 150-161.

Ustin, S.L.; Roberts, D.A.; Pinzon, J.; Jacquemoud, S.; Gardner, M.; Scheer, G. et al. (1998) Estimating canopy water content of chaparral shrubs using optical methods. *Remote Sensing of Environment*, 65 (3), 280-291.

Wolfe, D.; Fereres, E.; Voss, R. (1983) Growth and yield response of two potato cultivars to various levels of water applied. *Irrigation Science*, 3, 211-222.

Yahyaoui, W.; Harnois, J.; Carpentier, R. (1998) Demonstration of thermal dissipation of absorbed quanta during energy-dependent quenching of chlorophyll fluorescence in photosynthetic membranes. *FEBS Letters*, 440 (1-2), 59-63.

Zarco-Tejada, P.; Berjon, A.; Lopez-Lozano, R.; Miller, J.; Martin, P.; Cachorro, V. et al. (2005) Assessing vineyard condition with hyperspectral indices: Leaf and canopy reflectance simulation in a row-structured discontinuous canopy. *Remote Sensing of Environment*, 99 (3), 271-287.

Zarco-Tejada, P.; Miller, J.; Haboudane, D.; Tremblay, N.; Apostol, S. (2004) Detection of chlorophyll fluorescence in vegetation from airborne hyperspectral CASI imagery in the red edge spectral region. In *2003-International Geoscience and Remote Sensing Symposium, IGARSS'03*, Toulouse, France, 598-600.

Zarco-Tejada, P.; Miller, J.; Morales, A.; Berjon, A.; Agüera, J. (2004) Hyperspectral indices and model simulation for chlorophyll estimation in open-canopy tree crops. *Remote Sensing of Environment*, 90 (4), 463-476.

Zhao, H.; Yan, L.; Gou, Z.; Zhang, L. (2006) The characteristic analyses of images from the UAV remote sensing system. In *2006 IEEE International Geoscience and Remote Sensing Symposium, IGARSS 2006*, Denver, CO. 3349-3351.

## **Objetivos Generales**

*La ciencia no es sino una perversión de sí misma a menos que tenga como objetivo final la mejora de la humanidad.*

Nikola Tesla (1856-1943).



Los objetivos generales de esta Tesis Doctoral son los siguientes:

1. Desarrollo de una plataforma de teledetección basada en un vehículo aéreo no tripulado (UAV) equipado con sensores de imagen de tipo multispectral y térmico.
2. Desarrollo de metodologías de calibración radiométrica, calibración geométrica y corrección atmosférica, que permitan la obtención de imágenes georreferenciadas de reflectancia y temperatura de superficie a partir de micro-sensores multispectrales y térmicos instalados en plataformas UAV.
3. Desarrollo de una metodología de detección de estrés hídrico a partir de imágenes multispectrales de alta resolución espacial y espectral, basada en la detección de la fluorescencia clorofílica en estado estacionario bajo condiciones de iluminación natural.
4. Desarrollo de una metodología para la determinación de la conductancia de la cubierta y Crop Water Stress Index (CWSI) a partir de imágenes térmicas de alta resolución.



# Capítulo 1

## **Thermal and Narrowband Multispectral Remote Sensing for Vegetation Monitoring from an Unmanned Aerial Vehicle**

**Autores:** Berni, J.A.J.<sup>a</sup>, Zarco-Tejada, P.J.<sup>a</sup>, Suarez, L.<sup>a</sup>, Fereres, E.<sup>a,b</sup>

<sup>a</sup> *Instituto de Agricultura Sostenible (IAS), Consejo Superior de Investigaciones Científicas (CSIC), Córdoba, Spain*

<sup>b</sup> *Departamento de Agronomía, Universidad de Córdoba (UCO), Córdoba, Spain*

**Publicado en:** *IEEE Transactions on Geoscience and Remote Sensing*, 47, (3), 722-738. Special Issue on Unmanned Airborne Vehicle (UAV) Sensing Systems for Earth Observations.

*“Los que se enamoran de la práctica sin la teoría son como los pilotos sin timón ni brújula, que nunca podrán saber a dónde van.”*

Leonardo da Vinci (1452-1519).

## **Resumen**

Las dos limitaciones críticas para el uso de imágenes de satélite en el manejo de cultivos en tiempo real son: a) la falta de imágenes con la resolución espacial y espectral óptima; y b) un tiempo de revisita desfavorable para la mayoría de aplicaciones de detección de estrés en cultivos. Las alternativas, basadas en plataformas aéreas tripuladas, son escasas debido a su alto coste operativo. Un requerimiento fundamental para proporcionar productos de teledetección útiles para la agricultura tendría que ser la capacidad de combinar alta resolución espacial y tiempos de respuesta rápidos. Sensores remotos instalados en vehículos aéreos no tripulados (*unmanned aerial vehicles* – UAV) podrían rellenar ese vacío, proporcionando una solución de bajo coste para satisfacer las necesidades de resolución espacial, espectral y temporal. Este artículo demuestra la viabilidad de generar productos de teledetección cuantitativa mediante un helicóptero no tripulado equipado con sensores de imagen térmica y multiespectral de banda estrecha. Durante el verano de 2007 la plataforma sobrevoló parcelas agrícolas, obteniendo imágenes en la región espectral de 7.5-13  $\mu\text{m}$  (40cm de resolución) e imágenes multiespectrales de banda estrecha en la región espectral de 400-800 nm (20cm resolución). Las imágenes de reflectancia y temperatura de superficie fueron obtenidas tras aplicar una corrección atmosférica basada en MODTRAN. Diversos parámetros biofísicos fueron estimados usando índices de vegetación (NDVI, TCARI/OSAVI y PRI) junto con los modelos físicos de transferencia radiativa PROSPECT y FLIGHT. Como resultado, mapas de índice de área foliar (LAI), contenido clorofílico ( $C_{ab}$ ), detección de estrés hídrico con el índice PRI, y temperatura de superficie, fueron producidas y validadas satisfactoriamente. Este trabajo demuestra que los resultados obtenidos con un sistema UAV no tripulado para aplicaciones agrícolas dieron como resultados estimaciones comparables, si no mejores, que las obtenidas por sensores aerotransportados tradicionales.

**Palabras clave:** multiespectral, banda estrecha, térmico, teledetección, vehículo aéreo no tripulado, modelos de transferencia radiativa, detección de estrés, UAS, UAV.

## **Abstract**

Two critical limitations for using current satellite sensors in real-time crop management are the lack of imagery with optimum spatial and spectral resolution, and an unfavourable revisit time for most crop stress-detection applications. Alternatives based on manned airborne platforms are lacking due to their high operational costs. A fundamental requirement for providing useful remote sensing products in agriculture is the capacity to combine high spatial resolution and quick turnaround times. Remote sensing sensors placed on *unmanned aerial vehicles* (UAV) could fill this gap, providing low cost approaches to meet the critical requirements of spatial, spectral and temporal resolution. This paper demonstrates the ability to generate quantitative remote sensing products by means of a helicopter-based UAV equipped with inexpensive thermal and narrow-band multispectral imaging sensors. During summer 2007 the platform was flown over agricultural fields, obtaining thermal imagery in the 7.5-13  $\mu\text{m}$  region (40 cm resolution), and narrow-band multispectral imagery in the 400-800 nm spectral region (20 cm resolution). Surface reflectance and temperature imagery were obtained, after atmospheric corrections with MODTRAN. Biophysical parameters were estimated using vegetation indices NDVI, TCARI/OSAVI, and PRI coupled with PROSPECT and FLIGHT models. As a result, image products of leaf area index (LAI), chlorophyll content ( $C_{ab}$ ), and water stress detection from PRI index and canopy temperature were produced and successfully validated. This work demonstrates that results obtained with a low-cost UAV system for agricultural applications yielded comparable estimations, if not better, than those obtained by traditional manned airborne sensors.

**Keywords:** multispectral, narrow-band, thermal, remote sensing, unmanned aerial vehicle, radiative transfer modeling, stress detection, UAS, UAV

## **1. Introduction**

Remote sensing for agricultural and crop management applications aims at providing spatial- and spectrally-derived surface parameters for crop classification and mapping (Erol & Akdeniz, 1996; Grignetti, 1997; PaxLenney, 1997), crop forecasting and yield predictions (Clevers, 1997; Moran, 1995; Rasmussen, 1992; Tucker, 1980), crop status and condition (Blackmer et al., 1994; Boissard et al., 1993; Clevers et al., 1994; Potdar, 1993), weed detection (Anderson et al., 1993; Everitt, 1995; Underwood, 2003), disease detection and nutrient deficiency (Adams et al., 1999; Adams et al., 2000; Malthus, 1993) and photosynthetic pigment content (Martin et al., 2007; Sampson et al., 2003; Zarco-Tejada et al., 2005). Critical issues such as the optimum spatial and spectral resolution, the turnaround time and repeat cycle are main factors limiting the usefulness of remote sensing products for precision crop management (Moran, 1997); in addition, data acquisition costs must be weighed against anticipated benefits. Current satellite-based products have limited application in crop management due to the low spatial and spectral resolutions provided, and the large revisit periods. Spatial resolution has been improved in some new satellite sensors such as Ikonos or Quickbird, however lacking the narrow spectral bands required for quantitative parameter retrievals on which most of the applications mentioned before are based. Moreover, thermal imaging is currently limited to medium-resolution sensors such as TERRA-ASTER (Yamaguchi, 1998), providing 90 m pixel size images which are impractical for site-specific agricultural applications.

Alternatives based on airborne sensors can deliver higher spatial and spectral resolutions, and are more flexible in terms of revisit time. Airborne remote sensing has demonstrated capabilities for vegetation condition monitoring due to high spatial and spectral resolution used, ranging between 0.5 and 2 m pixel size with 2 to 20 nm bandwidths in the 400-2500 nm spectral range. Work conducted for crop management and stress detection applications such as the estimation of chlorophyll content with the *Compact Airborne Spectrographic Imager* (CASI) (Moorthy, 2003; Sampson, 2003; Zarco-Tejada et al., 2004; Zarco-Tejada et al., 2004; Zarco-Tejada, 2001), leaf water content from the Airborne Visible Infrared Imaging Spectrometer (AVIRIS) (Cheng et al., 2006; Cheng, 2006; Roberts, 1997; Serrano, 2000; Ustin, 1998), carotenoid estimation (Sims, 2002; Zarco-Tejada et al., 2005), dry matter content (Fourty & Baret, 1997; Jacquemoud, 1996; Riano et al., 2005), and structural parameters such as ground cover and leaf area index (LAI) minimizing background effects on traditional indices such as NDVI (Haboudane et al., 2004), are examples of the use of airborne sensors. In addition, high spectral resolution thermal imagery has demonstrated high potential for water stress detection in crops because of the increased temperature of stressed vegetation (Jackson et al., 1977; Jackson et al.,

1981), enabling the detection of water-stressed trees in orchards for site specific field management (Sepulcre-Cantó et al., 2006; Sepulcre-Cantó et al., 2007; Sepulcre-Cantó, 2005). However, the high operating costs, long turnaround times due to high volume of data processing acquired in large airborne campaigns, and the lack of private corporations providing cost-effective products have limited the use of airborne so far to research activities.

Back in 1977, Jackson (Jackson et al., 1977) envisioned a fleet of airborne thermal scanners collecting remote sensing imagery over irrigated fields to generate maps for irrigation scheduling based on an automated decision support system. However, after 30 years this vision still seems futuristic due to the mentioned limitations mostly based on the costs required and the operational complexity involved. Another potential application of canopy temperature measurements is its capability for genotype screening in breeding programs for drought resistance (Blum et al., 1982; Reynolds, 1998). A new era of remote sensing is emerging with the arrival of unmanned aerial vehicles (UAV) for civil applications. Scientific interest in this type of platforms is growing and a number of experiences have already been reported. Large fixed-wing UAVs, most of them NASA funded, have been tested for agricultural applications, such is the case of the solar-powered Pathfinder Plus over coffee orchards in Hawaii (Herwitz et al., 2004; Herwitz, 2002), the smaller RCATS/APV-3 tested over California vineyards (Johnson et al., 2003), or the future European Pegasus UAV (Everaerts, 2005). Miniaturization and cost reduction of inertial sensors, GPS devices and embedded computers have enabled the use of a new generation of autopilots for inexpensive model aircrafts (Esposito, 2007; Esposito, 2007). At present time commercial, off-the-shelf (COTS) autopilots are readily available for an easy integration with small model aircrafts. Rotary-wing UAVs are also available, but complexity of the flight control system, smaller endurance, and the lack of autopilots supporting helicopter platforms have prevented a wide use of this platform. However, some successful applications have also been developed (Haitao, 2007; Lambers, 2007; Sugiura, 2005).

Along with the development of low-cost autopilot systems, also imaging sensors have suffered a critical size, weight and price reduction, evolving from large sensors, rack mounted dataloggers and control computers to palm size imagers that can be easily installed into these micro aircrafts (Esposito, 2007; Herwitz, 2002). An example is the development of uncooled thermal instruments which avoid the use of heavy and expensive cooled sensors yet obtaining similar results at better spatial resolutions. The main problem concerning this type of micro-sensors is that they require spectral and geometric characterization to retrieve physical values such as ground reflectance or

surface temperature. This is the reason why most of the applications mentioned before focused only on digital values or visual qualitative interpretation.

This paper describes the integration of COTS optical and thermal sensors placed on an unmanned aerial platform, focusing into radiometric quality of the acquired imagery. The main objective of this work was to demonstrate that it is possible to combine successfully an unmanned rotary-wing platform and digital multispectral and thermal sensors, along with the appropriate calibrating methodologies, for agricultural applications. The assessment is conducted on narrowband vegetation indices in the 400 1000 nm and thermal spectral regions for quantitative parameter retrievals. Narrow-band vegetation indices and thermal retrieval from crop canopies were then used to generate maps that could assist managers in water stress detection and many other site specific applications in agriculture. In particular, this manuscript deals with the estimation of biophysical parameters such as leaf area index (LAI), chlorophyll content, a pre-visual indicator of stress based on the Photochemical Reflectance Index (Gamon et al., 1992) (PRI), and water stress detection using thermal imagery. Calibration and atmospheric effects are also considered and assessed for the correct retrieval of parameters from the UAV system.

## **2. Methods**

The UAV helicopter platform was developed to carry a payload with thermal and multispectral imaging sensors for remote sensing operation. A total of 288 flights were conducted in spring and summer 2007 for both flight testing and imagery acquisitions over crop fields for parameter validation and stress detection using narrow spectral bands and thermal imagery. A description of the payload, sensor calibration, physical models used for parameter retrievals from multispectral imagery, and thermal corrections to account for atmospheric transmission are given below.

### **2.1. UAV and payload description**

The UAV airframe used in this study was based on a model helicopter (Benzin Acrobatic, Vario, Germany), modified to carry the camera system, autopilot and sensors. Modifications consist mainly in a larger engine (29 cc), oversized landing skids and a container for camera installation. The UAV was controlled by an autopilot system (model AP04H, UAV Navigation, Madrid, Spain) which provided autonomous navigation based on waypoints programmed during the mission planning. The air segment (Figure 1.1a) consists on a dual CPU logic which controls an integrated Attitude Heading Reference System (AHRS) based on a L1 GPS board, 3 axis accelerometers, yaw rate gyros and a 3 axis magnetometer. The CPUs continuously monitored

internal sensors for battery status, internal temperature and barometric pressure, including an external RPM sensor. The guidance is based on standard servos controlled by Pulse-Width Modulation (PWM) outputs from the autopilot. A radio link communicates with the ground segment sending telemetry of position, attitude and status at 20Hz frequency.

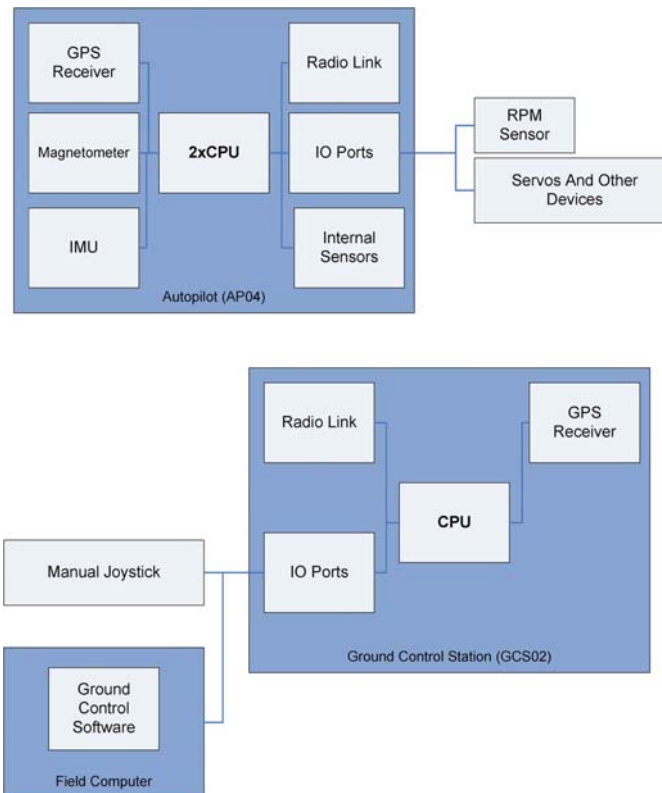


**Figure 1.1.** Block diagram showing the components for the a) autopilot and b) ground control station.

The ground segment (Figure 1.1b) consists on a control box which contains a CPU in charge of processing the safety manual control and sends the telemetry to a laptop PC where the user application is running. This application monitors the status and position of the UAV and allows the user to upload and modify the flight plan. There is an additional GPS antenna on the ground control station used for pointing the telemetry antenna towards the UAV platform.

The flight plans are performed starting with the autonomous take off, continuing with an autonomous flight over a number of way points at a given altitude, and finally landing (Figure 1.2). Flight altitude was selected depending on the study area to cover, camera field of view and the desired spatial resolution for remote sensing imagery acquisition. The nominal speed in autonomous mode was fixed at 30 km/h.

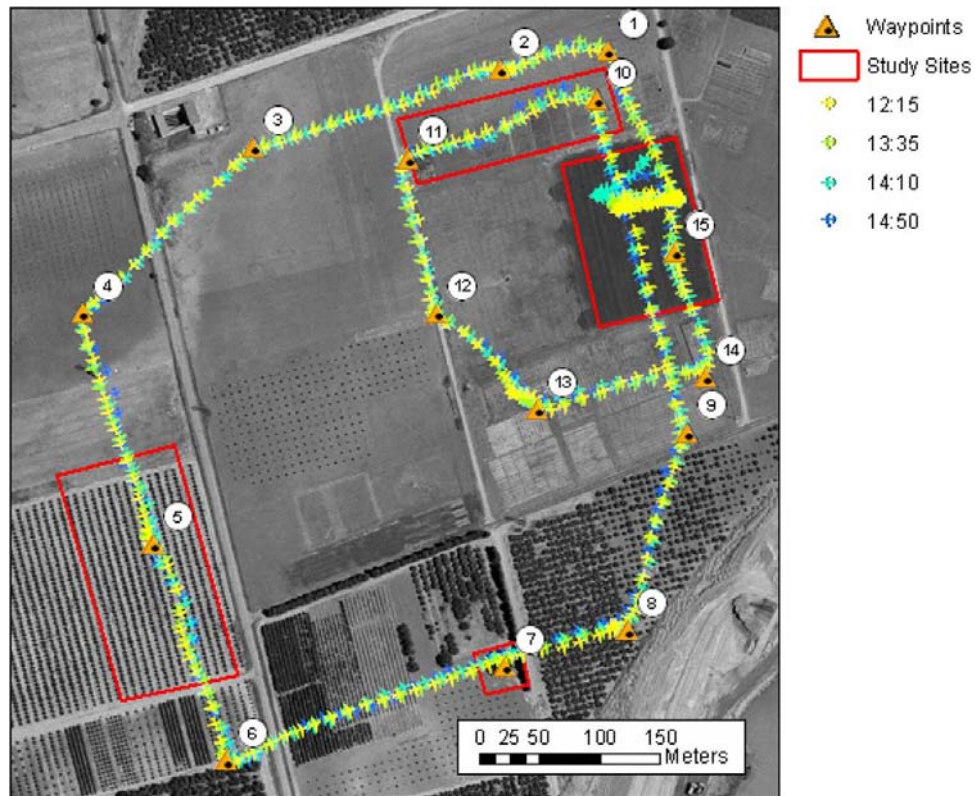


**Figure 1.2.** Sample flight plan undertaken over four study sites, showing the path followed by the platform. Each numbered triangle symbols represent a waypoint programmed on the autopilot's flight plan. Four consecutive flights are overlapped, showing the precise paths followed by the UAV.

### **2.1.1. Multispectral Camera**

The multispectral sensor used in this study was a 6-band multispectral camera (MCA-6, Tetracam, Inc., California, USA). The camera consists of 6 independent image sensors and optics with user configurable filters. The image resolution is 1280x1024 pixels with 10-bit radiometric resolution and optics focal length of 8.5mm, yielding an angular FOV of  $42.8^{\circ} \times 34.7^{\circ}$ . Table 1.1 shows a summary of the multispectral camera sensor specifications. Different bandsets were used depending on the objectives sought for the remote sensing study, including 25 mm diameter bandpass filters of 10 nm FWHM (Andover Corporation, NH, USA), with center wavelengths at 490 nm, 550 nm, 670 nm, 700 nm, 750 nm, and 800 nm. The raw images were compressed on a proprietary format and stored on individual compact flash cards installed in the camera. Image triggering was activated from the ground control station when the helicopter reached the desired study site.

**Table 1.1.** Multispectral MCA-6 Image Sensor Specifications

Array Elements	1280 x 1024
Pixel Size	5.2 $\mu$ m x 5.2 $\mu$ m
Image Area	6.66mm x 5.32mm
Output	10-bit digital raw data
Scan Mode	Progressive
S/N Ratio	54 dB
Fixed Pattern Noise	< 0.03% $V_{\text{PEAK-TO-PEAK}}$
Dark Current	28mV/s
Dynamic Range	60 dB
Total weight (6 sensors)	2.7 kg

### 2.1.2. Thermal Camera

The thermal imager used in this study was the Thermovision A40M (FLIR, USA) equipped with a 40° FOV lens and connected via IEEE-1394 protocol. The image sensor is a Focal Plane Array (FPA) based on uncooled microbolometers with a resolution of 320x240 pixels and spectral response in the range 7.5-13  $\mu$ m (Table 1.2). The camera delivers digital raw images at 16 bits of at-sensor calibrated radiance with a dynamic range of 233 K – 393 K. The sensor implements an internal calibration for non uniformity correction (NUC) and internal temperature calibration. The camera was controlled by a PC104 embedded computer (Cool Little Runner 2, LiPPERT, Germany), storing one raw image on a compact flash card every two seconds over the entire flight. A laboratory calibration was conducted using a calibration blackbody source (RAYBB400, Raytek, CA, USA).

**Table 1.2.** Thermal FLIR Image Sensor Specifications

Array Elements	320 x 240
Pixel Size	38 $\mu$ m x 38 $\mu$ m
Spectral response	7.5-13 $\mu$ m
Sensibility	0.08K at 303K
Dynamic Range	233K- 393K
Total weight	1.7 kg

During the calibration a need for stabilization after switch on was noticed. Temperature changes over the course of 30 minutes show the convergence to the black body temperature (Figure 1.3). Absolute temperature shifts observed were caused by the internal camera calibration which is automatically activated when the internal temperature changes above a configured value. A one-hour camera stabilization procedure was conducted before each remote sensing campaign.

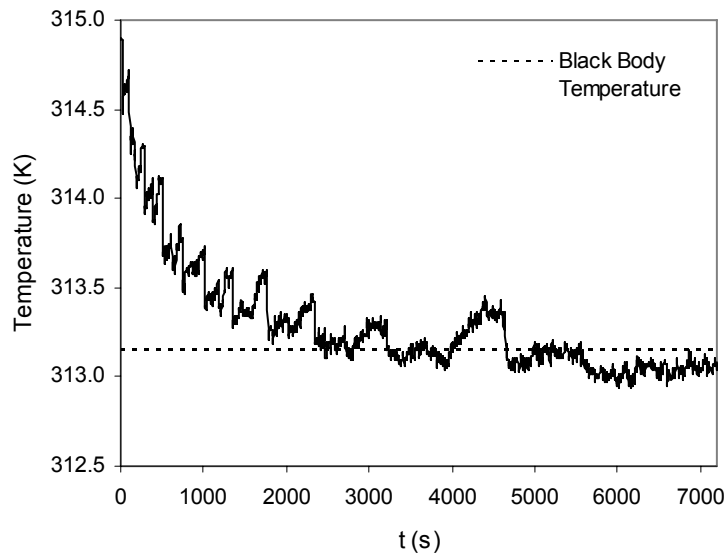


**Figure 1.3.** Changes of the radiometric temperature measured by the camera after power on over the course of two hours.

### 2.1.3. Camera geometric calibration

Several methodologies are available to conduct an accurate geometric calibration over non-metric commercial cameras (Heikkilä, 1997; Tsai, 1987). The objective of this calibration is to recover the intrinsic camera parameters (focal distance, principal point coordinates and lens radial distortion). In this case Bouguet’s calibration toolbox (Bouguet, 2001) was used, consisting of placing a calibration checkerboard pattern on a fixed location and acquiring several images from different locations and orientations. The grid corner coordinates were extracted semi-automatically from the images, and the intrinsic parameters and exterior orientation were calculated. In the case of the thermal camera, a calibration pattern was built using resistive wires to obtain a bright pattern when electricity circulated through the wires, thus increasing their temperature. Bouguet’s model uses a different lens distortion model than the one implemented by the software employed for the aerotriangulation which is based on Wolf (Wolf, 1983). In the former, radial and tangential distortion can be estimated. In this case tangential distortion was neglected and only the radial component was taken into account. The equation for Bouguet’s model is shown in Equation (1.1), whereas Wolf’s model is described in Equation (1.2). A least square adjustment was conducted to fit Equation (1.2) to Equation (1.1).

$$dr = k_1 r^2 + k_2 r^4 + k_5 r^6 \quad [1.1]$$

$$dr = k_0 r + k_1 r^3 + k_2 r^5 \quad [1.2]$$

Table 1.3 shows the intrinsic parameters estimated for the thermal and multispectral cameras used in this study. For the multispectral camera, in a second stage, one of the cameras was used as reference and the relative position of the rest of the cameras was estimated solving the system as different stereo rigs for each reference-camera pair.

**Table 1.3.** FLIR and MCA cameras intrinsic parameters

fc	16.999	mm	8.474	mm
xc	0.0254	mm	0.1307	mm
yc	-0.0998	mm	0.1501	mm
k1	-1.48861E-03		5.21444E-04	
k2	-2.45442E-02		-3.81969E-03	
k3	-3.53002E-03		3.30444E-05	

## 2.2. Multispectral sensor calibration and vegetation indices used for parameter estimation

Multispectral image calibration was conducted using the empirical line method (Smith G. M. & Milton E. J., 1999) by placing two 2x2 m levelled dark and white targets in a central location within the flight path of the UAV platform. Field spectral measurements were taken on the calibration targets with an ASD Field Spectrometer (FieldSpec Handheld Pro, ASD Inc., CO, USA) in the 350-1050 nm spectral range at the time of image acquisition. The ASD Field Spectrometer was first calibrated using a Spectralon (SRT-99-180, LabSphere, NH, USA) white panel, therefore enabling the calculation of white and dark panel reflectance spectra to be used later for the empirical line calibration method.

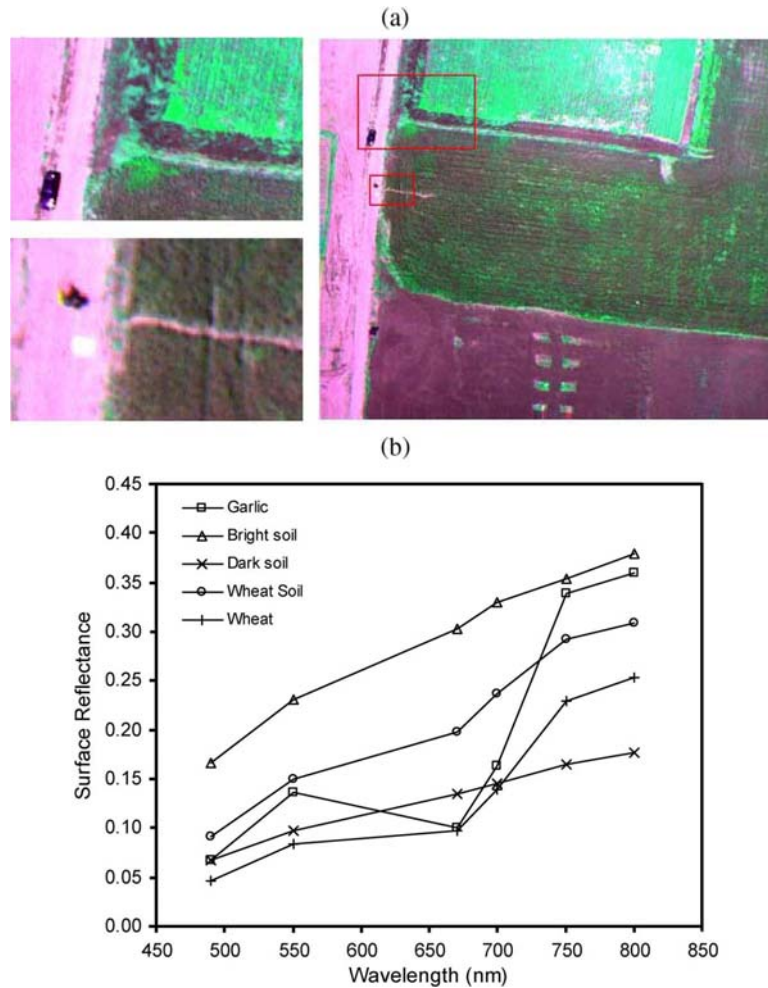


**Figure 1.4.** a) Multispectral imagery collected by the MCA-6 camera at 0.15m spatial resolution and 6 spectral bands with 10 nm FWHM; b) spectra extracted from different image targets in the 400-800 nm spectral region.

The empirical line calibration method derived the coefficients needed to fit uncalibrated airborne MCA-6 multispectral imagery to field-measured reflectance spectra. Figure 1.4 shows sample imagery and reflectance spectra for different field targets acquired with the MCA-6 multispectral camera onboard the UAV platform over one of the study sites, which included a field planted with garlic, bright soil, dark soil, bare soil between wheat rows, and a wheat field. Spectra from the different targets clearly show the photosynthetic pigment absorption in the visible spectral region (400-700 nm) in green vegetation, with an increased reflectance due to canopy scattering in the near-infrared region beyond 700 nm. A field validation assessment was conducted to evaluate the calibration method used to calculate surface reflectance, by measuring reflectance spectra with the ASD field spectrometer over different targets found on imagery acquired at different times of day. Figure 1.5 shows the validation of the calibration method using cotton and corn fields. UAV airborne flights were conducted three times over the course of one day on June 2007, acquiring field ASD spectra over cotton, corn with different canopy densities, and bare soil. The UAV MCA-6 spectral imagery and field spectra

were compared and generally agreed, yielding an RMSE=1.17% (n=90) after empirical line methods were applied at each flight time.

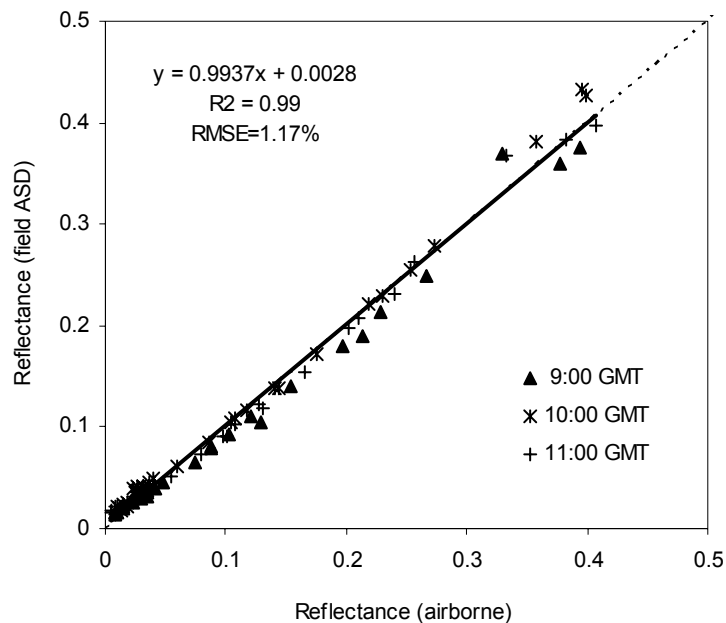


**Figure 1.5.** Validation of the surface reflectance acquired by the MCA-6 multispectral camera as compared with the ASD field spectrometer. The plot shows 90 points from 3 flights over 5 targets (3 corn crop sites, 1 soil target, and 1 cotton site) for 6 spectral bands.

Three vegetation indices were calculated from the airborne spectra using the six 10 nm FWHM bands of the multispectral camera. The Normalized Difference Vegetation Index (NDVI) (Rouse et al., 1974) was calculated to assess the estimation of canopy leaf area index (LAI). The Transformed Chlorophyll Absorption in Reflectance Index (TCARI) (Haboudane, 2002) based on the Modified Chlorophyll Absorption in Reflectance (MCARI) (Daughtry et al., 2000), normalized by the Optimized Soil-Adjusted Vegetation Index (OSAVI) (Rondeaux et al., 1996) to obtain TCARI/OSAVI is demonstrated to successfully minimize soil background and leaf area index variation in crops, providing predictive relationships for chlorophyll concentration estimation with narrow-band imagery in closed crops (Haboudane, 2002) and in open tree canopy orchards (Zarco-Tejada et al., 2004). Finally, the Photochemical Reflectance Index (PRI), originally developed for xanthophyll cycle pigment change detection (Gamon et al., 1992), a potential indicator for carotenoid/chlorophyll ratio monitoring (Dobrowski et al., 2005; Sims, 2002; Suárez, 2007), was calculated to assess its potential capability for water stress detection from the UAV platform. The PRI index was calculated with the MCA-6 camera using additional 10 nm FWHM filters centered at 530 and 570 nm wavelengths. The three indices are described in Equations 1.3-1.5.

$$NDVI = \frac{R_{800} - R_{670}}{R_{800} + R_{670}} \quad [1.3]$$

$$TCARI / OSAVI = \frac{3 \cdot [(R_{700} - R_{670}) - 0.2 \cdot (R_{700} - R_{550}) \cdot (R_{700} / R_{670})]}{(1 + 0.16) \cdot (R_{800} - R_{670}) / (R_{800} + R_{670} + 0.16)} \quad [1.4]$$

$$PRI = \frac{R_{570} - R_{531}}{R_{570} + R_{531}} \quad [1.5]$$

Field measurements of crown leaf area index were conducted with a Plant Canopy Analyzer (LAI-2000; Li-Cor, NE, USA) on an olive orchard using the method reported in (VILLALOBOS, 1995). A total of 6 trees were measured, and identified on the high-spatial resolution imagery acquired with the UAV platform. Field measurements of canopy LAI were also conducted on a variety trial corn field and 7 plots planted with different varieties were assessed. Mean spectral reflectance was calculated for each tree crown and variety plot, and indices calculated. Relationships between field-measured crown and canopy LAI and the NDVI index were also developed.

Leaf-level radiative transfer model PROSPECT (Jacquemoud & Baret, 1990) was linked with the canopy-level Forest LIGHT Interaction Model (FLIGHT) (North, 1996) to obtain predicting algorithms for chlorophyll concentration (Cab) from the airborne TCARI/OSAVI index. The modelling method consisted on ranging input chlorophyll a+b from 15 to 90 µg/cm<sup>2</sup> and crown leaf area index (cLAI) from 0.5 to 7. The rest of the input parameters were fixed for typical and field-measured structural parameters presented in Table 1.4. A total of 36 different input combinations were simulated, and TCARI/OSAVI calculated from the modelled spectra (Figure 1.6a and 1.6b). Ground truth chlorophyll content was estimated for a total of 41 olive tree and peach crowns using the SPAD meter (SPAD-502DL, Minolta, Japan). A total of 50 leaves were sampled from each crown, and mean SPAD measurements were used to estimate total chlorophyll content through SPAD-Cab relationships developed for each crop using destructive sampling methods based on spectrophotometer readings in the laboratory.

**Table 1.4.** Nominal values and parameters used for leaf and canopy modeling with PROSPECT and FLIGHT for the peach study site.

#### PROSPECT INPUTS

Leaf Internal Structure Parameter	N	1.8
Leaf Chlorophyll a+b content ( $\mu\text{g}/\text{cm}^2$ )	$C_{ab}$	15, 30, 45, 60, 75, 90
Leaf equivalent water thickness (cm)	$C_w$	0.0121
Leaf dry matter content ( $\text{g}/\text{cm}^2$ )	$C_m$	0.003
Brown pigments relative parameter	$C_s$	0.001

#### FLIGHT INPUTS

Total leaf area index	0.06035, 0.1207, 0.2413, 0.3621, 0.6035, 0.8449
Leaf angle distribution	0.015, 0.045, 0.074, 0.1, 0.123, 0.143, 0.158, 0.168, 0.174
Aerial optical thickness	0.1
Soil roughness	0.1
Leaf size (Equivalent radius, m)	0.02
Crown leaf area index (cLAI)	0.5, 1, 2, 3, 5, 7

To assess the capability of PRI for stress detection from the UAV platform the Photochemical Reflectance Index (PRI) was calculated from the MCA-6 camera. A variety trial corn field was flown at different times during the course of the day, and variety plots that differed in water status were identified on the imagery. Assessment of PRI for stress detection was conducted studying the relationships between PRI and plot temperature obtained from the UAV thermal and multispectral cameras. To remove effects of canopy or soil temperature variations on the vegetation index, the comparisons were made among corn plots with the same NDVI range.

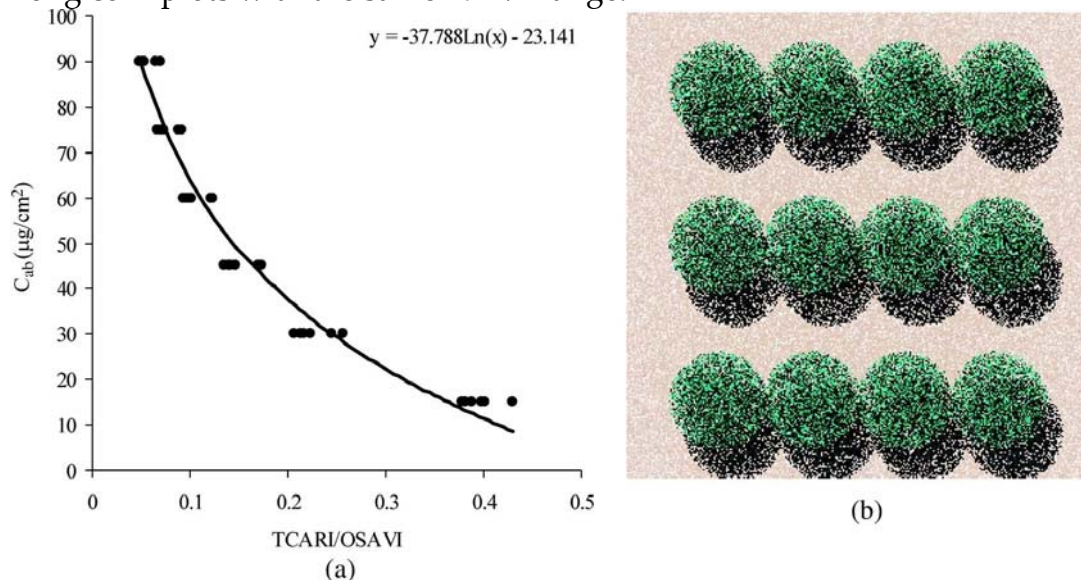


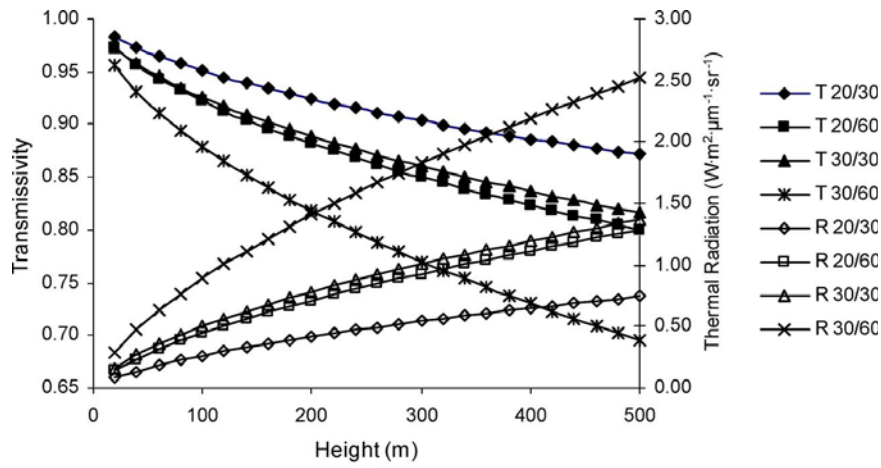
**Figure 1.6.** a) Algorithm to estimate chlorophyll a+b from TCARI/OSAVI index developed with the FLIGHT radiative transfer model. Input parameters for simulating the peach orchard canopy reflectance ranged between 0.5 and 7 (LAI) and 15 and 90  $\mu\text{g}/\text{cm}^2$  ( $C_{ab}$ ); b) Sample 3D scene simulated with FLIGHT model for developing the scaling-up algorithm to estimate chlorophyll concentration (cLAI= 2,  $C_{ab}$ = 45  $\mu\text{g}/\text{cm}^2$ ).

### 2.3. Methods for surface temperature estimation

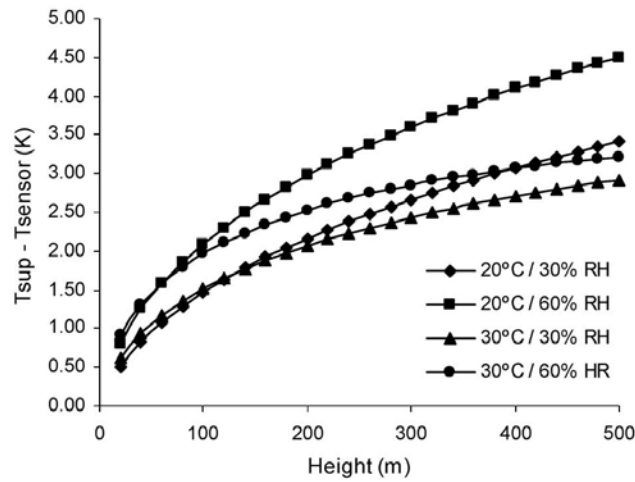
Different methods have been proposed recently to retrieve surface temperature from thermal sensors. A review of methods can be found in (Dash et al., 2002; Kerr, 2004; Sobrino, 2002). The thermal sensor used in this study provided a single band in the 7.5-13  $\mu\text{m}$ , therefore only techniques developed for single-channel atmospheric correction were used. Methods based on the Radiative Transfer Equation (RTE) use Equation (1.6) to estimate surface temperature. Needed parameters are atmospheric transmittance ( $\tau_\lambda$ ), emissivity ( $\varepsilon_\lambda$ ), down-welling ( $L_{atm,\lambda}^\downarrow$ ) and up-welling thermal radiation ( $L_{atm,\lambda}^\uparrow$ ) which are driven mainly by water vapour content, air temperature and distance to object.

$$L_{sensor,\lambda} = \left[ \varepsilon_\lambda B_\lambda(T_S) + (1 - \varepsilon_\lambda) L_{atm,\lambda}^\downarrow \right] \cdot \tau_\lambda + L_{atm,\lambda}^\uparrow \quad [1.6]$$

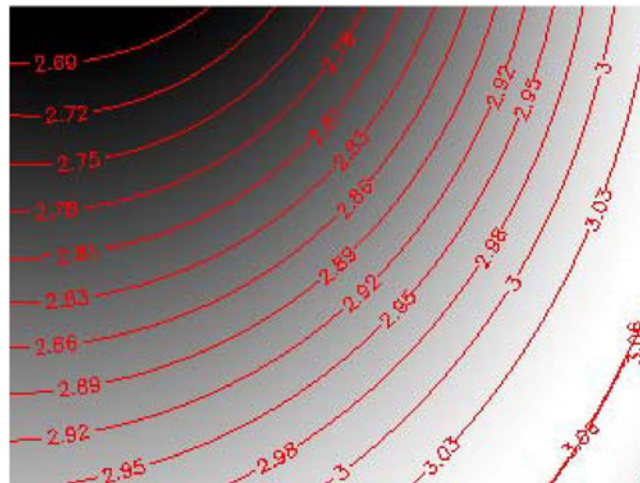
The MODTRAN radiative transfer code (Berk et al., 1999) was used to model  $\tau_\lambda$  and  $L_{atm,\lambda}^\uparrow$ , while  $L_{atm,\lambda}^\downarrow$  was measured in the field with a thermal sensor (LaserSight, Optris, Germany) pointing towards the zenith upwards with a field of view of  $15^\circ$  and a spectral response of 8-14 $\mu\text{m}$ . Since only vegetation temperature was retrieved as part of this study, surface emissivity was considered as 0.98 as an accepted value for natural vegetation (Salisbury & D'Aria, 1992). Local atmospheric conditions such as air temperature, relative humidity and barometric pressure were measured at the time of flight with a portable weather station (Model WXT510, Vaisala, Finland) and used as input into MODTRAN model. A single-layer atmosphere with uniform conditions was considered for the simulations since the variation for the typical UAV flight altitude (150-200m) could be neglected. Both, path transmittance and thermal radiance were simulated at different sensor altitudes and integrated for the spectral response range of the thermal camera. Two 4th grade polynomial relationships were fitted for transmittance and thermal radiation as a function of path length. The results for different atmospheric conditions are shown in Figure 1.7a, demonstrating that flight altitude can influence surface temperatures, if not corrected for atmospheric conditions. For instance, a bias of more than 4 K can occur under high relative humidity and low temperatures.



(a)



(b)



(c)

**Figure 1.7.** a) Simulated atmospheric transmittance and thermal radiation as function of platform altitude; b) effects of flight altitude and atmospheric conditions  $T_a(^{\circ}\text{C})/\%RH$  on the surface temperature estimation for a black body at 300K; c) distribution of the atmospheric correction effects as function of the off-nadir view for a uniform black body at 300K, atmospheric conditions  $20^{\circ}\text{C} / 60\% RH$ , flight altitude of 150m, pitch= $10^{\circ}$  and roll= $6^{\circ}$ .

Due to the camera wide FOV (40°) and the helicopter tilt angles, path lengths for each pixel had to be corrected. Assuming an image collected at a given time, the principal point of the camera  $P_o$  is located at the coordinates  $(X_o, Y_o, Z_o)$  with an attitude of  $(\varphi, \omega, \kappa)$  which are pitch, roll and yaw respectively. An approximation of these values was extracted from the autopilot telemetry, and calibration for pixel-to-sensor variations across the image conducted. For a given point  $P$  with ground coordinates  $(X_p, Y_p, Z_p)$ , the image coordinates of the corresponding pixel reduced to the principal point and with the effects of lens distortion removed  $(x'_p, y'_p)$  were estimated using the collinearity Equation (1.7),

$$\begin{bmatrix} x'_p \\ y'_p \\ -c \end{bmatrix} = \frac{1}{\lambda_p} M \begin{bmatrix} X_p - X_o \\ Y_p - Y_o \\ Z_p - Z_o \end{bmatrix} \quad [1.7]$$

where  $M$  is the rotation matrix obtained from the attitude angles,  $c$  is the focal distance and  $\lambda_p$  is the associated scale factor.

Equation 1.7 can be reversed and therefore ground coordinates for a given pixel can be calculated with Equations 1.8 and 1.9 if the centre of projection of the image ( $O$ ) and ground elevation are known, and the terrain is considered flat,

$$\begin{aligned} Xp &= \lambda_p [m_{11}x'_p + m_{21}y'_p + m_{31}(-c)] + Xo \\ Yp &= \lambda_p [m_{12}x'_p + m_{22}y'_p + m_{32}(-c)] + Yo \\ Zp &= \lambda_p [m_{13}x'_p + m_{23}y'_p + m_{33}(-c)] + Zo \end{aligned} \quad [1.8]$$

being,

$$\lambda_p = \frac{m_{12}x'_p + m_{23}y'_p - m_{33}c}{Z_p - Z_o} \quad [9]$$

Since  $Zp-Zo$  can be estimated as the mean altitude above ground level for a flat terrain,  $Xp$  and  $Yp$  can be solved. The distance to the ground point can be expressed as:

$$D_{o-p} = \sqrt{(X_o - X_p)^2 + (Y_o - Y_p)^2 + (Z_o - Z_p)^2} \quad [1.10]$$

We used this methodology to estimate the sensor-to-pixel distance across the image, needed to generate a transmittance and thermal radiation map for each image. The effect of this correction is shown in Figure 1.7b.

A flight campaign was conducted measuring simultaneously surface temperature with a thermal gun (LaserSight, Optris, Germany) over 3 different surfaces: soil, white and black targets (Figure 1.8). The RMSE before calibration was 3.44 K, which was reduced to 0.89 K after atmospheric correction.

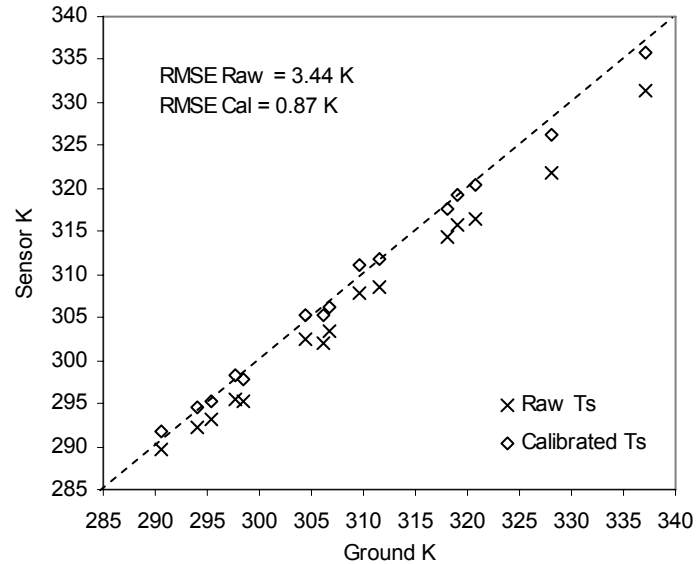


**Figure 1.8.** Comparison between ground truth surface temperature (IRT measured) and obtained from the thermal camera at 150 m flight altitude before (×) and after (o) applying the atmospheric correction.

#### 2.4. Automatic mosaicking with aerotriangulation methods

GPS and INS systems used along with photogrammetric methods enable the estimation of direct platform orientation without ground control points (Agouris & Schenk, 1996; Grejner-Brzezinska, 2005). Position and attitude were extracted directly from the autopilot AHRS with a time resolution of 0.05s. The lack of a precise synchronization between the autopilot time (based on GPS time) and image triggering prevented the estimation of the direct platform orientation. In the case of the thermal camera, time and mission time were reset before each flight campaign, acquiring one image every two seconds. This method enabled the estimation of an approximate exterior orientation (EO) for the projection centre of each image.



**Figure 1.9.** Footprints for the images acquired during a flight plan conducted over an orange orchard. Red rectangles correspond to single image frames. The yellow rectangle represents the overlapping of two consecutive images (stereo-pair).

Calibrated images were imported into Leica Photogrammetry Suite (Leica Geosystems, Switzerland) together with the EO file in plain text format. Images taken during UAV turns and outside the study sites were removed. The low platform speed (30 km/h) and low altitude (200 m) of the UAV generated a high degree of overlapping among images along the flight direction (80-90% overlap). The high overlapping obtained was very important to ensure that only the most nadir part of each image was considered to avoid viewing directional effects on both multispectral and thermal imagery. Figure 1.9 shows a study area with red rectangles representing the image footprint over the orange trees study site, with the yellow rectangle indicating the overlapping area of a stereo pair. Once the model was created and configured, tie points were generated automatically and a minimum number of ground control and check points were manually measured on the corresponding images. Aerotriangulation was calculated and the results revised until the RMS error of the ground control points was below the estimated pixel resolution. Finally an ortho-mosaic could be generated using an existing DTM or a uniform terrain height (Figure 1.10).

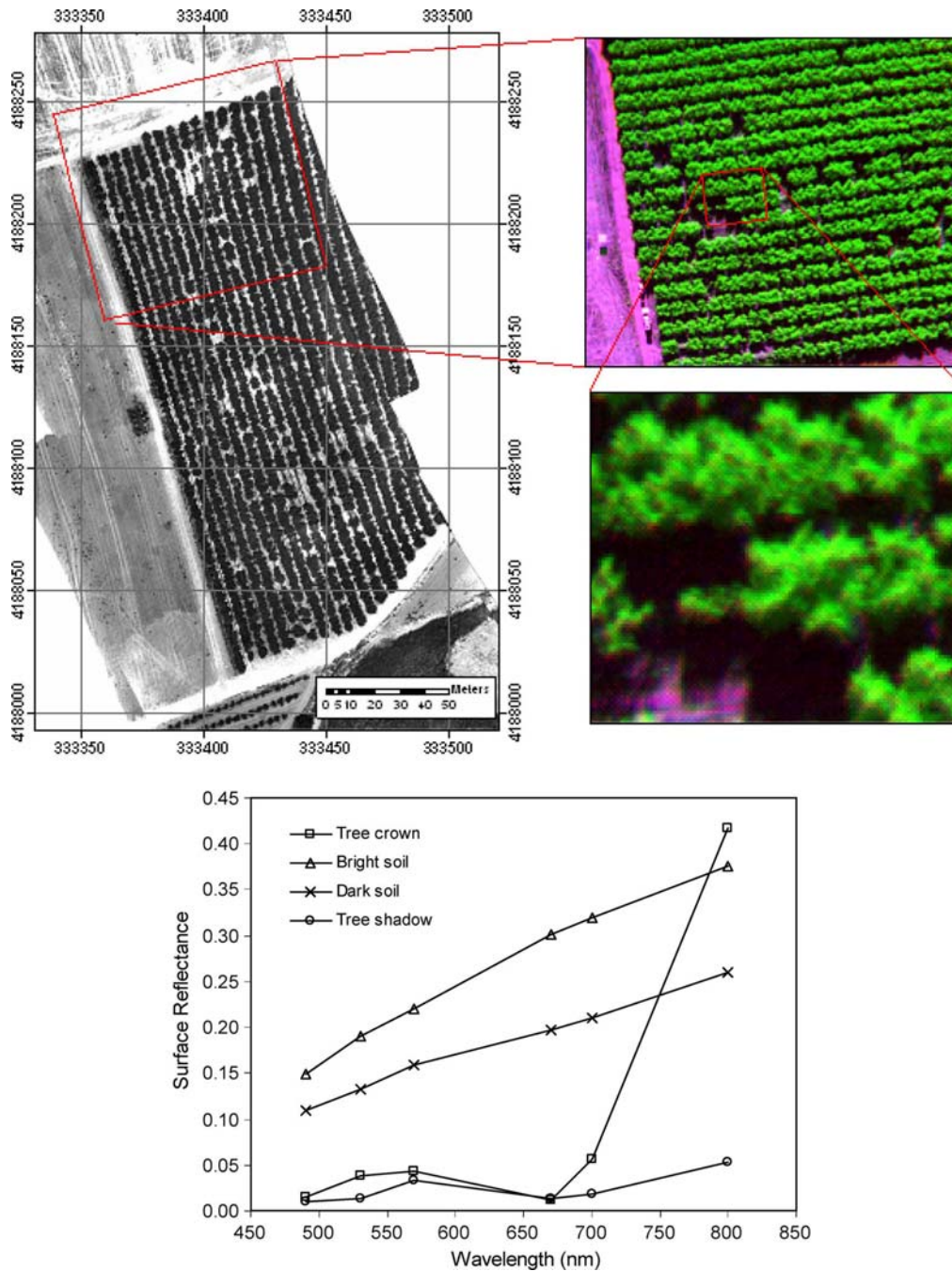


**Figure 1.10.** a) Multispectral ortho-mosaic collected over a peach orchard at 20 cm spatial resolution. The image on the top left is a false color zoom of the study site, showing on the bottom right image the detailed view of the tree crowns at full resolution. b) Spectral reflectance extracted from different targets from the image mosaic.

## 2.5. Study sites

During the validation stage of the remote sensing UAV system, a total of three study sites were selected to conduct airborne campaigns with onboard remote sensing instruments to validate the ability for biophysical parameter retrieval. The detection of water stress in different crops was conducted on study sites with plant water status differences.

A commercial peach orchard near Cordoba (Spain) was studied to assess if water stress levels could be detected with high resolution thermal imagery acquired from the UAV platform. The field studied had part under regulated deficit irrigation, RDI (Fereres & Soriano, 2007) while the other part had ample water supply.

Another study was carried out over a corn variety test field to show the performance of the multispectral camera over herbaceous crops and the use of narrow-band vegetation indices to detect crop water status. The field was divided into 72 individual plots 2.4x10m in size, comprising 24 varieties replicated three times. The field was last irrigated in mid June, and was under water stress in July, at the time of flight acquisitions. The study included measurements of stomatal conductance and leaf water potential in six different cultivars, taken four times during the day and coincident with the four flights that were undertaken on July 6th.

Finally, an olive variety test orchard was flown to assess the capability of the multispectral imagery to retrieve biophysical parameters such as chlorophyll *a+b* content and leaf area index over discontinuous crops at the tree level. The orchard was very heterogeneous as compared to a commercial olive orchard because of the large number of varieties that had been planted.

### **3. Results and Discussion**

Results from the 12 airborne campaigns flown over the peach orchard on July 2007 at solar noon showed thermal variations over the entire area due to variation in irrigation levels. As expected, the canopies of trees under RDI were clearly warmer than those of fully irrigated trees (Figure 1.11), with an average difference of 4.3K between trees supplied with full ET and RDI trees. This experiment demonstrated that low-cost thermal imagers onboard unmanned vehicles successfully estimated absolute surface temperature through radiometric calibration and atmospheric correction methods, enabling the detection of tree water stress levels.

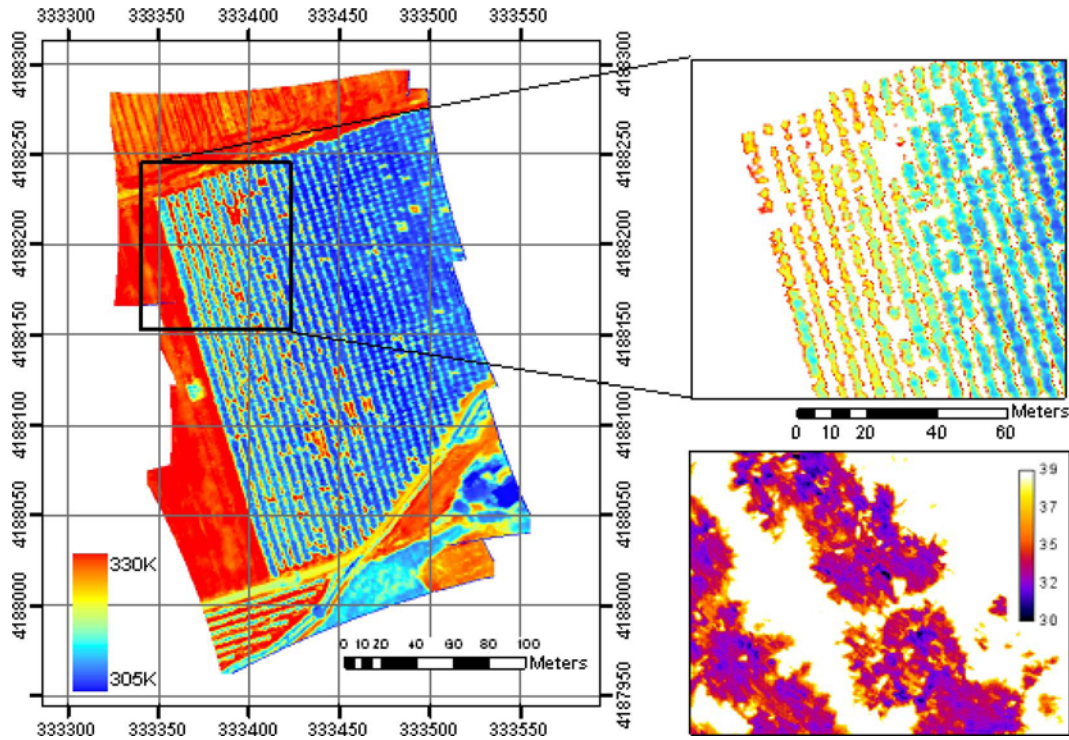
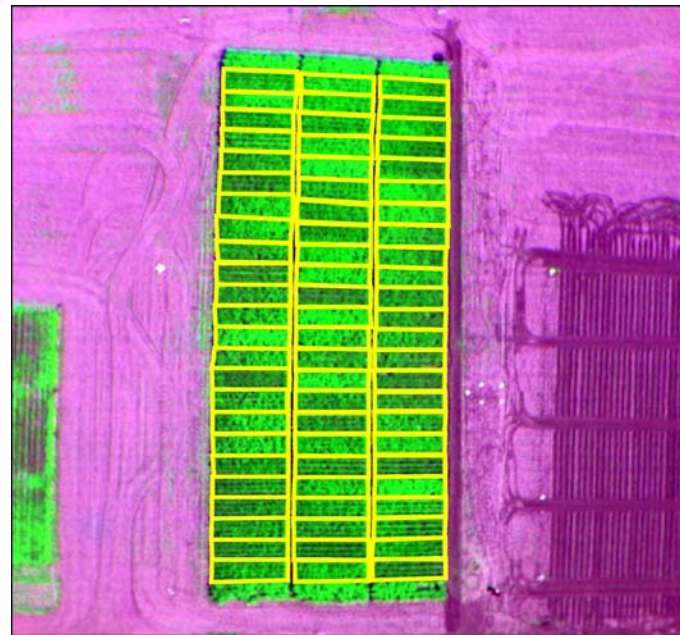
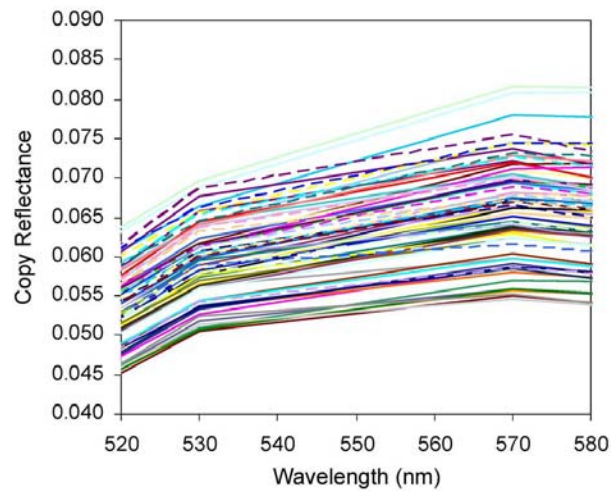


**Figure 1.11.** Thermal ortho-mosaic obtained from the UAV over the peach orchard at 40 cm resolution. The zoomed image on the top shows the water stressed trees (warmer, in red and yellow) as compared with the fully irrigated trees (blue). The bottom right image shows a low altitude image where within-crown thermal variability is observed.

Results on the corn field experiment flown four times on June 6th 2007 with multispectral (Figure 1.12a) and thermal cameras demonstrated that spectral reflectance was successfully calibrated as compared with ground ASD measurements, yielding 1.17% RMSE. Mean spectral reflectance and temperature extracted for each variety plot showed a relationship between the vegetation index proposed as an indicator of stress (PRI) and plot temperature as an indicator of canopy conductance. The reflectance spectra in the PRI region between 520 and 580 nm showed a positive slope between 530 nm and 570 nm (Figure 1.12b) typical of plants under water stress (Suárez, 2007). The physiological indicator of stress (PRI) and the canopy temperature for each plot were constrained to NDVI values ranging between 0.76 and 0.78 to minimize structural and soil effects on the indices.



(a)



(b)

**Figure 1.12.** a) Corn plots of different varieties imaged by the MCA-6 camera onboard the UAV system; b) extracted reflectance spectra in the 530-570 nm spectral region for the calculation of the PRI index used for stress detection.

Results shown on Figure 1.13a prove the lack of relationship between NDVI and canopy temperature for such small range of NDVI values. These results suggest that differences in plot temperature were due to canopy conductance and water stress levels, but not due to structural parameters or differences in ground coverage. On the other hand, physiological indicators of stress such as PRI and canopy temperature showed a good relationship within the same NDVI levels ( $r^2=0.69$ ) (Figure 1.13b), suggesting that both visible (400-700 nm spectral range, PRI) and thermal regions (7.5-13  $\mu\text{m}$ ) were able to detect crop water stress levels from the low cost UAV platform.

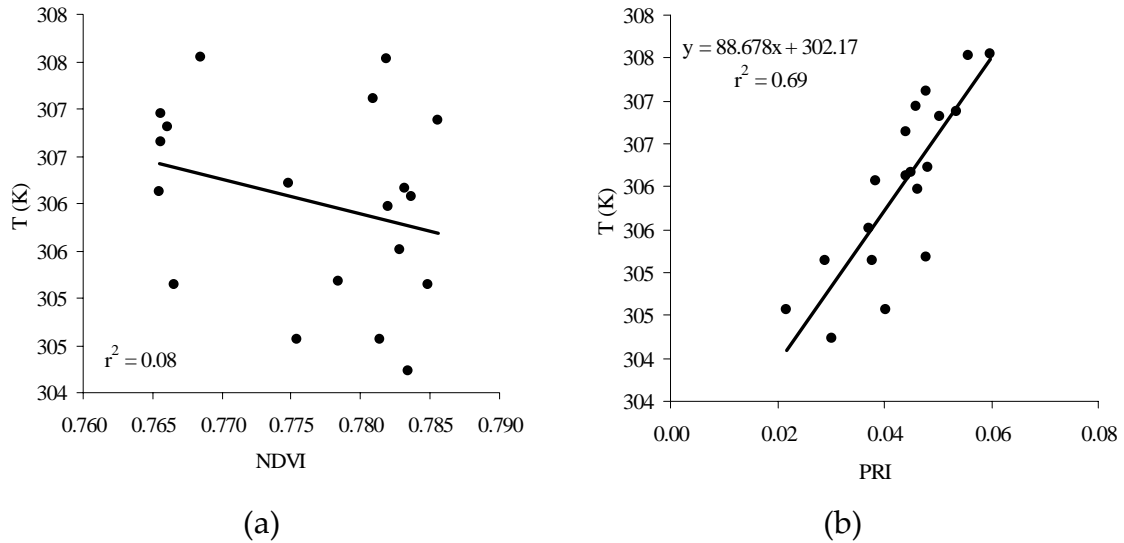


**Figure 1.13.** a) Relationships obtained between the FLIR thermal camera and spectral indices calculated from the multispectral camera over corn blocks under same NDVI levels for a) block T vs NDVI; and b) block T vs PRI. These plots demonstrate the sensitivity of PRI as indicator of water stress.

One important application in plant breeding would be to use the canopy temperature measurements from the UAV platform for screening different genotypes for drought avoidance. This approach was successfully used in wheat sometime ago (Blum et al., 1982) and has been tried in other breeding programs (i.e., Reynolds, 1998), but it has been limited by operational difficulties associated with the use of sensors at ground level. The results obtained from the flights over the corn variety trial illustrate the potential of this platform for genotype screening. Figure 1.14 shows the genotypic variability in canopy temperatures measured from the UAV at four different times on 6 July. On that day there was significant water stress, as indicated by midday leaf water potential values that varied between 1.3 and 1.5 MPa. Canopy temperatures in the morning were quite uniform among corn cultivars, but they started to diverge as the day went on. Figure 1.15 illustrates the genotypic differences between two cultivars that had very similar NDVI but that clearly differed in their stress response. In the morning, both canopies were cooler than the air and the stomatal conductance values were quite high, indicating high transpiration rates. As water stress set in, the stomata close and canopy temperatures increase. By early afternoon, the time of maximum evaporative demand, the stomata are quite closed and the canopies are warmest. However, one genotype is cooler than the other and has higher stomatal conductance, and hence transpiration (Figure 1.15). It should be emphasized that such genotypic differences were detected in our flights among commercial varieties, while differences of greater magnitude should be expected among breeding lines.

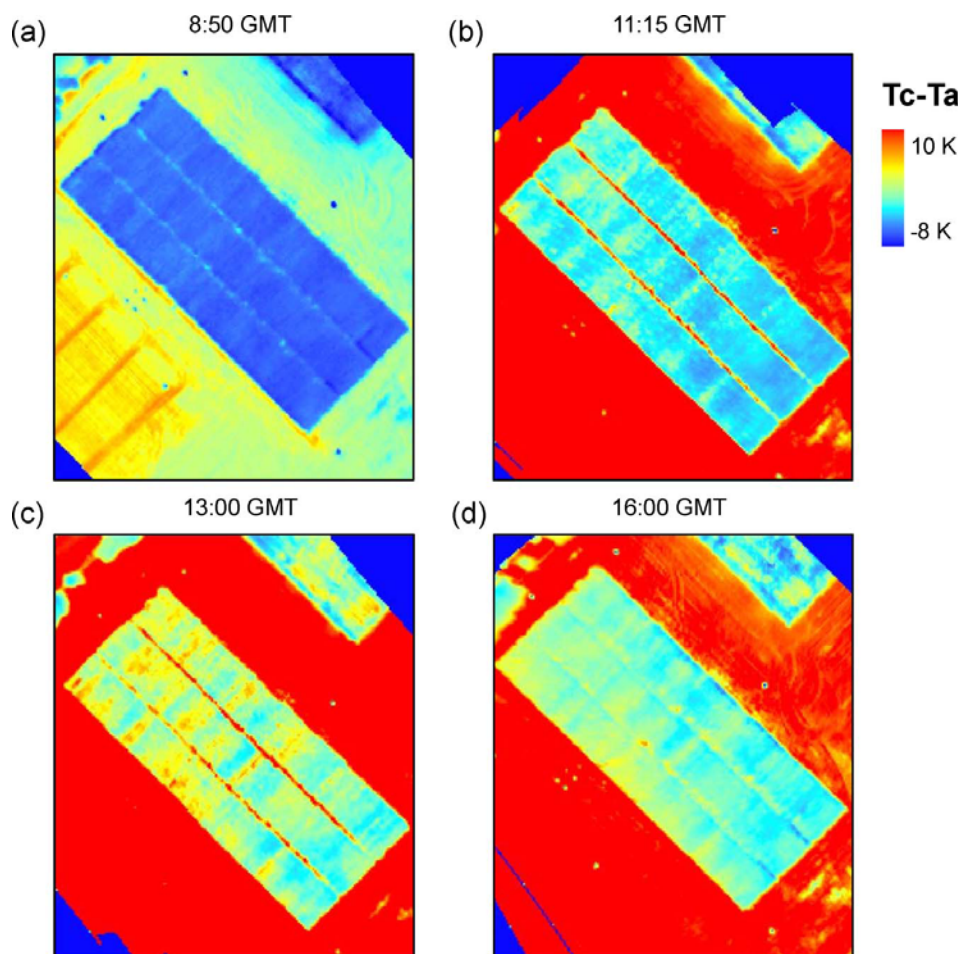


**Figure 1.14.** Thermal images acquired over the corn field at 0.4m pixel resolution showing the Tc-Ta changes at four different times of day. The greatest thermal variability between corn variety plots is obtained at midday, continuing during the afternoon.

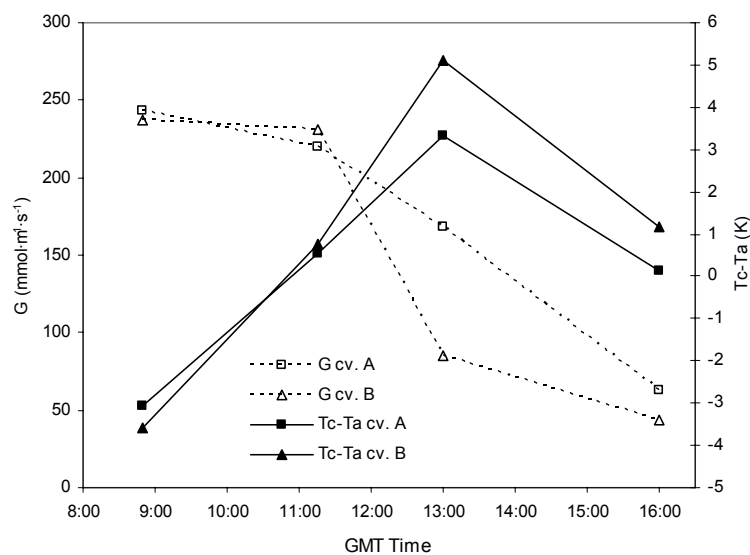


**Figure 1.15.** Diurnal stomatal conductance (G) and canopy Tc-Ta acquired from two corn cultivars. Differences found in the stomatal conductance at noon for both cultivars yielded variations that could be tracked by the thermal imagery.

The estimation of chlorophyll concentration from the multispectral instrument onboard the UAV used the Mahalanobis supervised classification method to extract pure crown regions of interest for each individual tree in the olive and peach orchards. The TCARI/OSAVI chlorophyll index calculated from mean crown spectra extracted from the imagery successfully estimated chlorophyll a+b concentration. A comparison between field measured Cab and airborne-estimated Cab yielded a RMSE of 4.2  $\mu\text{g}/\text{cm}^2$  and  $r^2=0.89$  (Figure 1.16), demonstrating the capabilities of the multispectral MCA-6 camera onboard the UAV platform for estimating chlorophyll content at the crown level.

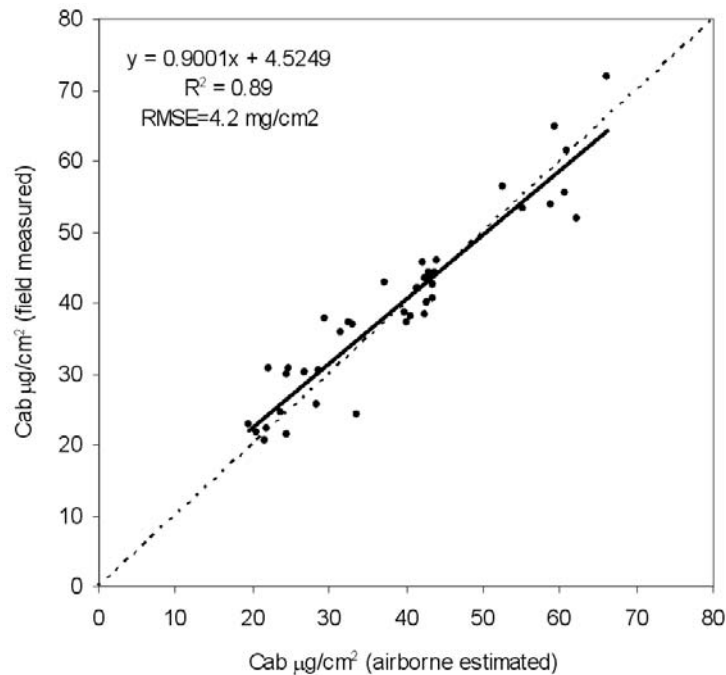


**Figure 1.16.** Ground truth chlorophyll content (Cab) measured in olive and peach trees compared with UAV-estimated Cab through the TCARI/OSAVI index and predictive algorithms.

NDVI and LAI relationships were studied for olive and corn (Figure 1.17a). In the case of olive trees, NDVI was calculated for each individual tree using the mean spectra from the same regions of interest that were used for chlorophyll content estimation. For the corn field, NDVI was calculated using the average spectrum from each block. In both cases NDVI correlated with ground truth LAI ( $r^2=0.5$  for corn;  $r^2=0.88$  for olive trees). The lower correlation in the corn field is probably related to the differential responses of corn canopy architecture to water deficits, as the leaves of some cultivars had rolled and become more erected to reduce plant radiation load. The resulting RMSE for the estimated LAI was 0.16 (Figure 1.17b). From the extracted crown spectra in the olive orchard (Figure 1.18a), maps of mean chlorophyll a+b content (Figure 1.18b) and LAI (Figure 1.18c) were generated using relationships described earlier. The resulting maps show the spatial variability of chlorophyll content and LAI over the orchard obtained from the UAV system.

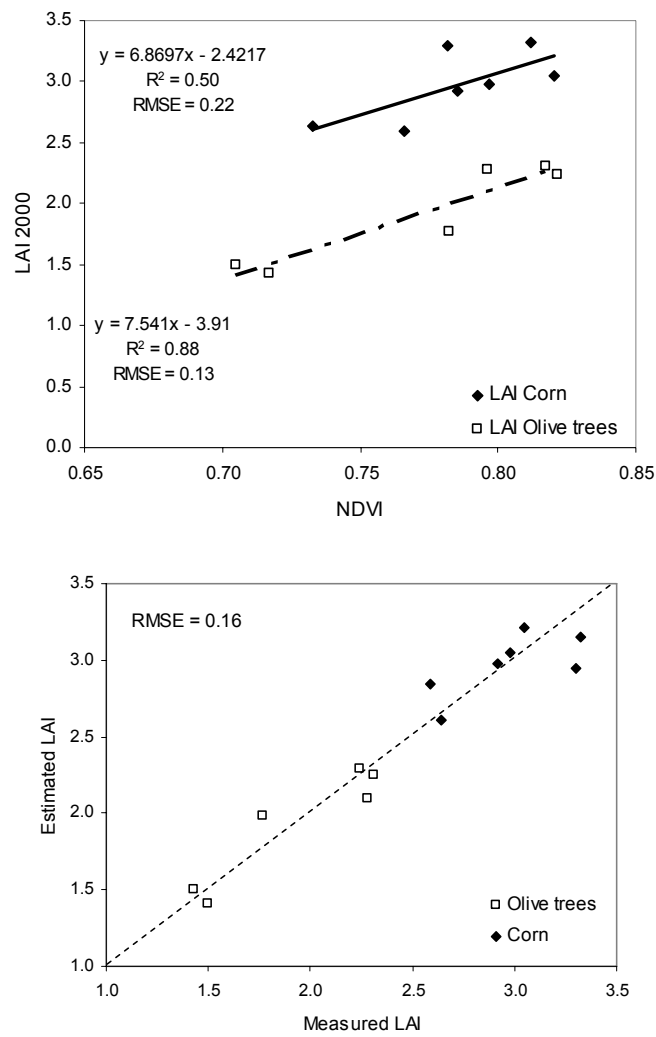


**Figure 1.17.** a) Relationships between NDVI and LAI for corn and olive trees; b) Validation of LAI estimates from the UAV vs ground truth LAI measurements.

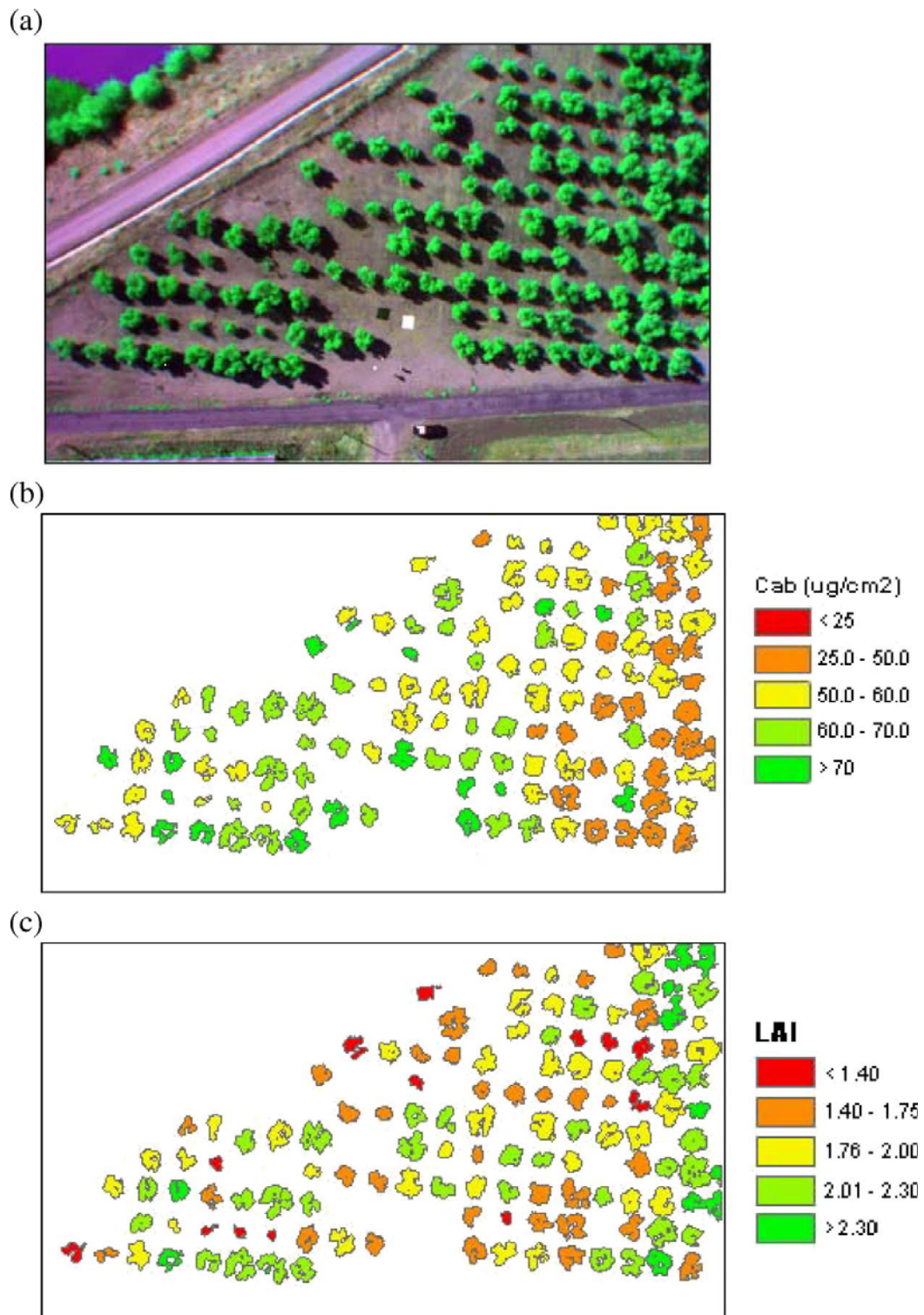


**Figure 1.18.** Sample multispectral imagery acquired over an olive orchard with the MCA 6 camera at 10 nm FWHM bandwidths onboard the UAV platform (0.15 m spatial resolution), showing the chlorophyll content and LAI maps obtained.

## **4. Conclusions**

This work demonstrated the ability to generate quantitative remote sensing products by means of a helicopter-based UAV equipped with commercial off-the-shelf (COTS) inexpensive thermal and multispectral imaging sensors. The low cost and operational flexibility, along with the high spatial, spectral and temporal resolution provided at high turnaround times, make this platform suitable for a number of applications, including precision farming or irrigation scheduling, where time-critical management is required. Laboratory and field calibration methods provided 6-band 10 nm FWHM multispectral imagery with RMSE of 1.17% in ground reflectance and less than 0.2 m spatial resolution. For the thermal camera, atmospheric effects on transmittance and atmospheric thermal path radiation were found very important even for low altitude flights where errors higher than 4 K could be achieved if those effects were not considered. Atmospheric correction methods based on MODTRAN radiative transfer model showed the successful estimation of surface temperature images of 40 cm spatial resolution, yielding RMSE < 1 K.

Appropriate bandset configurations selected for the multispectral camera enabled the calculation of several traditional narrowband vegetation indices (NDVI, TCARI/OSAVI and PRI), which were linked to biophysical parameters using quantitative methods based on physical approaches such as PROSPECT and FLIGHT models. The validation results obtained for the estimation of LAI in corn ( $r^2=0.5$ ) and olive trees ( $r^2=0.88$ ), chlorophyll a+b concentration (RMSE=4.2  $\mu\text{g}/\text{cm}^2$ ;  $r^2=0.89$ ), and the relationships between canopy temperature and stomatal conductance in corn revealed results comparable to those obtained in similar experimental campaigns using currently state-of-art imaging spectrometer or multi-band sensors onboard manned aircraft (Haboudane et al., 2004; Sepulcre-Cantó et al., 2006; Zarco-Tejada et al., 2004), and open way to the use of this platform as a screening tool in drought resistance breeding programs. The photochemical reflectance index (PRI) used for stress detection demonstrated on imagery acquired over corn fields that the vegetation index was well related with canopy temperature ( $r^2=0.69$ ) suggesting its use as a good indicator of water stress.

Photogrammetric techniques were required to register the frame-based imagery to map coordinates. Cameras were geometrically characterized with their intrinsic parameters, achieving location errors within one pixel size. These techniques along with position and attitude data gathered from the autopilot enabled the generation of large mosaics semi-automatically with minimum use of ground control points. Main limitations encountered for this platform were the endurance (20 min) and the low flight speed (30 km/h), limiting the productivity to 70 hectares per flight. However, the operating flexibility of

vertical take off and landing platforms make it ideal for experimental purposes. For large commercial agricultural applications, where hundreds of hectares should be monitored quickly, the use of fixed-wing UAVs with enhanced endurance, moderate cruise speeds and easier operation would be preferred to rotary wing aircrafts. UAV-based remote sensing platforms are expected to fill the gap in the extended use of remote sensing in agriculture. With the cost reduction of autopilots and imaging sensors, it will soon become an invaluable tool to monitor the water status of crops, with the aim of achieving Jackson's envision in the 70's for real-time irrigation scheduling and crop monitoring.

### **Acknowledgments**

Financial support from the Spanish Ministry of Science and Education (MEC) for the projects AGL2005-04049, EXPLORA-INGENIO AGL2006-26038-E/AGR, CONSOLIDER CSD2006-67, is gratefully acknowledged, as well as the Junta de Andalucía - Excelencia AGR-595, and in-kind support provided by Bioiberica through the project PETRI PET2005-0616. Technical support from UAV Navigation and Tetracam Inc. for accommodating changes in the firmware for MCA-6 adapted to UAV operation is also acknowledged. V. González, M. Morales, C. Ruz, G. Sepulcre-Cantó, D. Notario, M. Guillén, C. Trapero and I. Calatrava are acknowledged for measurements and technical support in field campaigns. Special thanks to A. Vera and M. Ruiz Bernier, our UAV human backup pilots.

### **References**

- Adams, M.L.; Norvell, W.A.; Philpot, W.D.; Peverly, J.H. (2000) Toward the discrimination of manganese, zinc, copper, and iron deficiency in 'bragg' soybean using spectral detection methods. *Agronomy Journal*, 92, 268-274.
- Adams, M.L.; Philpot, W.D.; Norvell, W.A. (1999) Yellowness index: an application of spectral second derivatives to estimate chlorosis of leaves in stressed vegetation. *International Journal of Remote Sensing*, 20, 3663-3675.
- Agouris, P.; Schenk, T. (1996) Automated aerotriangulation using multiple image multipoint matching. *Photogrammetric Engineering Remote Sensing*, 62, 703-710.
- Anderson, G.; Everitt, J.; Richardson, A.; Escobar, D. (1993) Using satellite data to map false broomweed (*Ericameria austrotexana*) infestations on South Texas rangelands. *Weed Technology*, 7, 865-871.

Blackmer, T.M.; Schepers, J.S.; Varvel, G.E. (1994) Light reflectance compared with other nitrogen stress measurements in corn leaves. *Agronomy Journal*, 86, 934-938.

Boissard, P.; Pointel, J.G.; Huet, P. (1993) Reflectance, green leaf-area index and ear hydric status of wheat from anthesis until maturity. *International Journal of Remote Sensing*, 14, 2713-2729.

Berk, A.; Anderson, G.; Acharya, P.; Chetwynd, J.; Bernstein, L.; Shettle, E.; Matthew, M.; Adler-Golden, S. (1999) Modtran4 user's manual. .

Blum, A.; Mayer, J.; Gozlan, G. (1982) Infrared thermal sensor of plant canopies as a screening technique for dehydration avoidance in wheat. *Field Crop Research*, 5, 137-146.

Bouguet, J. (2001) Camera calibration toolbox for matlab. [http://www.vision.caltech.edu/bouguetj/calib\\_doc/](http://www.vision.caltech.edu/bouguetj/calib_doc/) . Last visited 07 September, 2009.

Clevers, J.G.P.W.; Buker, C.; Vanleeuwen, H.J.C.; Bouman, B.A.M. (1994) A framework for monitoring crop growth by combining directional and spectral remote-sensing information. *Remote Sensing of Environment*, 50, 161-170.

Cheng, Y. B. and Zarco-Tejada, P. J. and Riano, D. and Rueda, C. A. and Ustin, S. L. (2006) Estimating vegetation water content with hyperspectral data for different canopy scenarios: relationships between AVIRIS and MODIS indexes. *Remote Sensing of Environment*, 105, 354-366.

Cheng, Y.B.; Riano, D.; Zarco-Tejada, P.J.; Ustin, S.L. (2006) Canopy water content estimates with AVIRIS imagery and MODIS reflectance products. *Remote Sensing And Modeling of Ecosystems for Sustainability III*, in Proceedings of SPIE 6298, 629809

Clevers, J.G.P.W. (1997) A simplified approach for yield prediction of sugar beet based on optical remote sensing data. *Remote Sensing of Environment*, 61, 221-228.

Dash, P.; Göttsche, F.M.; Olesen, F.S.; Fischer, H. (2002) Land surface temperature and emissivity estimation from passive sensor data: theory and practice current trends. *International Journal of Remote Sensing*, 23, 2563-2594.

Daughtry, C.S.T.; Walthall, C.L.; Kim, M.S.; de Colstoun, E.B.; McMurtrey, J.E. (2000) Estimating corn leaf chlorophyll concentration from leaf and canopy reflectance. *Remote Sensing of Environment*, 74, 229-239.

Dobrowski, S.; Pushnik, J.; Zarco-Tejada, P.; Ustin, S. (2005) Simple reflectance indices track heat and water stress-induced changes in steady-state chlorophyll fluorescence at the canopy scale. *Remote Sensing of Environment*, 97, 403-414.

Erol, H.; Akdeniz, F. (1996) A multispectral classification algorithm for classifying parcels in an agricultural region. *International Journal of Remote Sensing*, 17, 3357-3371.

Esposito, F. and Rufino, G. and Moccia, A. (2007) 1<sup>st</sup> mini-uav integrated hyperspectral/thermal electro-optical payload for forest fire risk management.

American Institute of Aeronautics and Astronautics, Infotech@Aerospace, 1, 653-665.

Esposito, F. and Rufino, G. and Moccia, A. and Donnarumma, P. and Esposito, M. and Magliulo, V. (2007) An integrated electro-optical payload system for forest fires monitoring from airborne platform. In *Proc. of IEEE Aerospace Conference 2007*, Big Sky, USA, 1-13.

Everaerts, J. (2005) Pegasus - bridging the gap between airborne and spaceborne remote sensing. *New Strategies For European Remote Sensing*, 395-401.

Everitt, J.H. and Anderson, G.L. and Escobar, D.E. and Davis, M.R. and Spencer, N.R. and Andrascik, R.J. (1995) Use of remote sensing for detecting and mapping leafy spurge (*Euphorbia esula*). *Weed Technology*, 9, 599-609.

Fereres, E.; Soriano, M. (2007) Deficit irrigation for reducing agricultural water use. *Journal of Experimental Botany*, 58, 147-159.

Fourty, T.; Baret, F. (1997) Vegetation water and dry matter contents estimated from top-of-the-atmosphere reflectance data: a simulation study. *Remote Sensing of Environment*, 61, 34-45.

Gamon, J.; Penuelas, J.; Field, C. (1992) A narrow-waveband spectral index that tracks diurnal changes in photosynthetic efficiency. *Remote Sensing of Environment*, 41, 35-44.

Grejner-Brzezinska, D. and Toth, C. and Yi, Y. (2005) On improving navigation accuracy of GPS/INS systems. *Photogrammetric Engineering and Remote Sensing*, 71, 377-389.

Grignetti, A. and Salvatori, R. and Casacchia, R. and Manes, F. (1997) Mediterranean vegetation analysis by multi-temporal satellite sensor data. *International Journal of Remote Sensing*, 18, 1307-1318.

Haboudane, D. and Miller, J. R. and Tremblay, N. and Zarco-Tejada, P. J. and Dextraze, L. (2002) Integrated narrow-band vegetation indices for prediction of crop chlorophyll content for application to precision agriculture. *Remote Sensing of Environment*, 81, 416-426.

Haboudane, D.; Miller, J.; Pattey, E.; Zarco-Tejada, P.; Strachan, I. (2004) Hyperspectral vegetation indices and novel algorithms for predicting green LAI of crop canopies: modeling and validation in the context of precision agriculture. *Remote Sensing of Environment*, 90, 352.

Haitao, X. and Lei, T. (2007) An autonomous helicopter system for aerial image collection, in *Proc. ASABE Annu. Int. Meeting, Tech. Papers*, Minneapolis, MN, Jun. 2007. Paper 071136.

Heikkilä, J. & Silvén, O. (1997) A four-step camera calibration procedure with implicit image correction, in *Proc. IEEE Comput. Soc. Conf. CVPR*, San Juan, PR, 1997, 1106-1112.

Herwitz, S.; Johnson, L.; Dunagan, S.; Higgins, R.; Sullivan, D.; Zheng, J. et al. (2004) Imaging from an unmanned aerial vehicle: agricultural surveillance and decision support. *Computers and Electronics in Agriculture*, 44, 49-61.

Herwitz, S.R.; Leung, J.G.; Higgins, R.G.; Dunagan, S.E.; Arvesen, J.C. (2002) Remote command-and-control of imaging payloads using commercial off-the-shelf technology, in *Proc. IEEE IGARSS, 2002*, vol. 5, 2726–2728.

Jackson, R.D.; Idso, S.B.; Reginato, R.J.; Pinter, P.J. (1981) Canopy temperature as a crop water-stress indicator. *Water Resources Research*, 17, 1133-1138.

Jackson, R.D.; Reginato, R.J.; Idso, S.B. (1977) Wheat canopy temperature - practical tool for evaluating water requirements. *Water Resources Research*, 13, 651-656.

Jacquemoud, S.; Ustin, S.L.; Verdebout, J.; Schmuck, G.; Andreoli, G.; Hosgood, B. (1996) Estimating leaf biochemistry using the PROSPECT leaf optical properties model. *Remote Sensing of Environment*, 56, 194-202.

Jacquemoud, S.; Baret, F. (1990) PROSPECT: a model of leaf optical properties spectra. *Remote Sensing of Environment*, 34, 75-91.

Johnson, L.; Herwitz, S.; Dunagan, S.; Lobitz, B.; Sullivan, D.; Slye, R. (2003) Collection of ultra high spatial and spectral resolution image data over California vineyards with a small UAV, in *Proc. Int. Symp. Remote Sens. Environ.*, Honolulu, HI, Nov. 10–14, 2003.

Kerr, Y. H., Lagouarde, J. P., Nerry, F., & Otlé, C. (2004) Land surface temperature retrieval techniques and applications: case of AVHRR. In: *Thermal Remote Sensing*. Florida, USA: CRC Press. pp. 30-109.

Lambers, K.; Eisenbeiss, H.; Sauerbier, M.; Kupferschmidt, D.; Gaisecker, T.; Sotoodeh, S.; Hanusch, T. (2007) Combining photogrammetry and laser scanning for the recording and modelling of the late intermediate period site of Pinchango Alto, Palpa, Perú. *Journal of Archaeological Science*, 34, 1702-1712.

Malthus, T. J. And Madeira, A. C. (1993) High-resolution spectroradiometry - spectral reflectance of field bean-leaves infected by botrytis-fabae. *Remote Sensing Of Environment*, 45, 107-116.

Martin, P.; Zarco-Tejada, P.; Gonzalez, M.; Berjon, A. (2007) Using hyperspectral remote sensing to map grape quality in 'tempranillo' vineyards affected by iron deficiency chlorosis. *VITIS*, 46, 7-14.

Moorthy, I. and Miller, J. R. and Noland, T. L. and Nielsen, U. and Zarco-Tejada, P. J. (2003) Chlorophyll content estimation of boreal conifers using hyperspectral remote sensing, in *Proc. IEEE IGARSS—Learning From Earth's Shapes and Sizes, 2003*, vol. I–VII, pp. 2568–2570

Moran, M. S. and Inoue, Y. and Barnes, E. M. (1997) Opportunities and limitations for image-based remote sensing in precision crop management. *Remote Sensing of Environment*, 61, 319-346.

Moran, M.S. and Maas, S.J. and Pinter Jr, P.J. (1995) Combining remote sensing and modeling for estimating surface evaporation and biomass production. *Remote Sensing Reviews*, 12, 335-353.

North, P.R.J. (1996) Three-dimensional forest light interaction model using a Montecarlo method. *IEEE Transactions on Geosciences and Remote Sensing*, 34, 946-956.

Potdar, M.B. (1993) Sorghum yield modeling based on crop growth-parameters determined from visible and near-ir channel NOAA AVHRR data. *International Journal of Remote Sensing*, 14, 895-905.

PaxLenney, M. and Woodcock, C. E. (1997) The effect of spatial resolution on the ability on to monitor the status of agricultural lands. *Remote Sensing of Environment*, 61, 210-220.

Rasmussen, M.S. (1992) Assessment of millet yields and production in northern burkina-faso using integrated NDVI from the AVHRR. *International Journal of Remote Sensing*, 13, 3431-3442.

Reynolds, M.P. and Singh, R.P. and Ibrahim, A. and Ageeb, O.A.A. and Larqueé-Saavedra, A. and Quick, J.S. (1998) Evaluating physiological traits to complement empirical selection for wheat in warm environments. *Euphytica*, 100, 85-94.

Riaño, D.; Vaughan, P.; Chuvieco, E.; Zarco-Tejada, P.; Ustin, S. (2005) Estimation of fuel moisture content by inversion of radiative transfer models to simulate equivalent water thickness and dry matter content: analysis at leaf and canopy level. *IEEE Transactions on Geoscience and Remote Sensing*, 43, 826.

Roberts, D. A. and Green, R. O. and Adams, J. B. (1997) Temporal and spatial patterns in vegetation and atmospheric properties from AVIRIS. *Remote Sensing of Environment*, 62, 223-240.

Rondeaux, G.; Steven, M.; Baret, F. (1996) Optimization of soil-adjusted vegetation indices. *Remote Sensing of Environment*, 55(2), 95-107.

Rouse J.W.; Haas R.H.; Schell J.A.; Deering D.W.; Harlan J.C. (1974) Monitoring the vernal advancements and retrogradation of natural vegetation. In NASA/GSFC, Greenbelt, MD, p. 371, 1974. Final Report.

Salisbury, J.W.; D'Aria, D.M. (1992) Emissivity of terrestrial materials in the 8-14  $\mu\text{m}$  atmospheric window. *Remote Sensing of Environment*, 42, 83-106.

Sampson, P. H. and Zarco-Tejada, P. J. and Mohammed, G. H. and Miller, J. R. and Noland, T. L. (2003) Hyperspectral remote sensing of forest condition: estimating chlorophyll content in tolerant hardwoods. *Forest Science*, 49, 381-391.

Sampson, P.; Zarco-Tejada, P.; Mohammed, G.; Miller, J.; Noland, T. (2003) Hyperspectral remote sensing of forest condition: estimating chlorophyll content in tolerant hardwoods. *Forest Science*, 49, 381-391.

Sepulcre-Cantó, G.; Zarco-Tejada, P. J.; Sobrino, J. A.; Jimenez-Munoz, J. C.; Villalobos, E. (2005) Spatial variability of crop water stress in an olive grove with high-spatial thermal remote sensing imagery. *Precision Agriculture*, 5, 267-272.

Sepulcre-Cantó, G.; Zarco-Tejada, P.; Jimenez-Munoz, J.; Sobrino, J.; Soriano, M.; Fereres, E. et al. (2007) Monitoring yield and fruit quality

parameters in open-canopy tree crops under water stress. Implications for ASTER. *Remote Sensing of Environment*, 107, 455-470.

Sepulcre-Cantó, G.; Zarco-Tejada, P.; Jimenez-Munoz, J.; Sobrino, J.; de Miguel, E.; Villalobos, F. (2006) Detection of water stress in an olive orchard with thermal remote sensing imagery. *Agricultural and Forest Meteorology*, 136, 31-44.

Serrano, L. and Ustin, S. L. and Roberts, D. A. and Gamon, J. A. and Peñuelas, J. (2000) Deriving water content of chaparral vegetation from aviris data. *Remote Sensing Of Environment*, 74, 570-581.

Sims, D.A. and Gamon, J.A. (2002) Relationships between leaf pigment content and spectral reflectance across a wide range of species, leaf structures and developmental stages. *Remote Sensing of Environment*, 81, 337-354.

Smith G. M.; Milton E. J. (1999) The use of the empirical line method to calibrate remotely sensed data to reflectance. *International Journal of Remote Sensing*, 20, 2653-2662.

Sobrino, J.A.; Li, Z.-L.; Soria, G.; Jimenez, J.C. (2002) Land surface temperature and emissivity retrieval from remote sensing data. *Recent Research Developments on Geophysics*, 4, 21-44.

Sugiura, R.; Noguchi, N.; Ishii, K. (2005) Remote-sensing technology for vegetation monitoring using an unmanned helicopter. *Biosystems Engineering*, 90, 369-379.

Suárez, L. and Zarco-Tejada, P.J. and Sepulcre-Cantó, G. and Pérez-Priego, O. and Miller, J.R. and Jiménez-Muñoz, J.C. and Sobrino, J. (2007) Assessing canopy pri for water stress detection with diurnal airborne imagery. *Remote Sensing of Environment*, 112, 560-575.

Tucker, C. J.; Holben, B. N.; Elgin, J. H.; McMurtrey, J. E. (1980) Relationship of spectral data to grain-yield variation. *Photogrammetric Engineering And Remote Sensing*, 46, 657-666.

Tsai, R.Y. (1987) Versatile camera calibration technique for high-accuracy 3d machine vision metrology using off-the-shelf TV cameras and lenses. *IEEE Transactions on Robotics and Automation*, RA-3, 323-344.

Underwood, E.; Ustin, S.; DiPietro, D. (2003) Mapping nonnative plants using hyperspectral imagery. *Remote Sensing of Environment*, 86, 150-161.

Ustin, S. L.; Roberts, D. A.; Pinzon, J.; Jacquemoud, S.; Gardner, M.; Scheer, G.; Castaneda, C. M.; Palacios-Orueta, A. (1998) Estimating canopy water content of chaparral shrubs using optical methods. *Remote Sensing of Environment*, 65, 280-291.

Villalobos, F. J.; Orgaz, F.; Mateos, L. (1995) Nondestructive measurement of leaf-area in olive (*Olea europaea* L) trees using a gap inversion method. *Agricultural And Forest Meteorology*, 73, 29-42.

Wolf, P.R. (1983) Elements of photogrammetry. New York: McGraw-Hill, 1983.

---

Yamaguchi, Y.; Kahle, A. B.; Tsu, H.; Kawakami, T.; Pniel, M. (1998) Overview of advanced spaceborne thermal emission and reflection radiometer (ASTER). *IEEE Transactions on Geoscience and Remote Sensing*, 36, 1062-1071.

Zarco-Tejada, P. J.; Miller, J. R.; Noland, T. L.; Mohammed, G. H.; Sampson, P. H. (2001) Scaling-up and model inversion methods with narrowband optical indices for chlorophyll content estimation in closed forest canopies with hyperspectral data. *IEEE Transactions on Geoscience and Remote Sensing*, 39, 1491-1507.

Zarco-Tejada, P.; Berjon, A.; López-Lozano, R.; Miller, J.; Martin, P.; Cachorro, V. et al. (2005) Assessing vineyard condition with hyperspectral indices: leaf and canopy reflectance simulation in a row-structured discontinuous canopy. *Remote Sensing of Environment*, 99, 271-287.

Zarco-Tejada, P.; Miller, J.; Harron, J.; Hu, B.; Noland, T.; Goel, N. et al. (2004) Needle chlorophyll content estimation through model inversion using hyperspectral data from boreal conifer forest canopies. *Remote Sensing of Environment*, 89, 189-199.

Zarco-Tejada, P.; Miller, J.; Morales, A.; Berjon, A.; Agüera, J. (2004) Hyperspectral indices and model simulation for chlorophyll estimation in open-canopy tree crops. *Remote Sensing of Environment*, 90, 463-476.



## Capítulo 2

### **Imaging chlorophyll fluorescence with an airborne narrow-band multispectral camera for vegetation stress detection**

**Autores:** Zarco-Tejada, P.J.<sup>a</sup>, Berni, J.A.J.a, Suárez, L.<sup>a</sup>, Sepulcre-Cantó, G.<sup>a</sup>, Morales, F.<sup>b</sup>, Miller, J.R.<sup>c</sup>

<sup>a</sup> *Instituto de Agricultura Sostenible (IAS), Consejo Superior de Investigaciones Científicas (CSIC), Córdoba, Spain*

<sup>b</sup> *Departamento de Nutrición Vegetal, Estación Experimental de Aula Dei (EEAD), Consejo Superior de Investigaciones Científicas (CSIC), Apdo, 13034, 50080 Zaragoza, Spain*

<sup>c</sup> *Dept. of Earth and Space Science and Engineering, York University, Toronto, Canada*

**Publicado en:** *Remote Sensing of Environment*, 113, 1262-1275.

*Si consigo ver más lejos es porque he conseguido auparme a hombros de gigantes.*

Isaac Newton (1643-1727).

## **Resumen**

En este artículo se muestra el avance realizado para la obtención de imágenes de fluorescencia usando la banda de oxígeno atmosférico O<sub>2</sub>-A con filtros de 1nm FWHM (full-width at half-maximum) centradas en 757.5 y 760.5nm. Para ello, imágenes multispectrales obtenidas desde el vehículo aéreo no tripulado (UAV) fueron obtenidas a 150m sobre el suelo en las regiones del térmico, visible e infrarrojo cercano, produciendo imágenes de 15cm de resolución espacial. Los experimentos de campo llevados a cabo simultáneamente en parcelas de olivo, melocotón y naranjo (experimentos de estrés hídrico) y en una parcela de olivar (ensayo de variedades), permitieron que la variabilidad en la emisión de fluorescencia fuese interpretada como una función del estado hídrico. En paralelo, el modelo hoja-cubierta reflectancia-fluorescencia, FluorMOD, fue usado para evaluar la capacidad de obtención de fluorescencia mediante el método *in-filling*, así como mediante índices publicados en la literatura. La fluorescencia obtenida usando el método *in-filling*, el índice derivado D702/D680 y los índices de reflectancia R690/R630, R761-R757 y R761/757 dieron los mejores resultados en el estudio de simulación, mostrándose insensible a la variación de índice de área foliar (LAI). El método *in-filling*, el índice calculado a partir de la derivada de la reflectancia D702/D608 y R761-R757 fueron los índices menos afectados por variaciones de clorofila a+b (C<sub>ab</sub>). Por otra parte, otros índices publicados para la detección de fluorescencia a nivel de hoja y cubierta mostraron alta sensibilidad a la variación de C<sub>ab</sub> y LAI, y por lo tanto fueron considerados menos adecuados para la detección en campo de la fluorescencia. La extracción de la señal de fluorescencia a partir de imagen aerotransportada usando el método *in-filling* fue validada mediante la comparación de medidas de campo de fluorescencia en estado estacionario (*F*<sub>s</sub>) usando los instrumentos PAM-2100 y GFS-3000, confirmando éstas las predicciones de las simulaciones. Los experimentos de estrés hídrico llevados a cabo en olivar y melocotonero demostraron la viabilidad de detectar la fluorescencia clorofílica (*F*) a nivel de árbol a partir de imágenes aéreas submétricas, resultando en coeficientes de determinación  $r^2=0.57$  (olivar) y  $r^2=0.54$  (melocotonero). La estimación de fluorescencia, y su relación con la fotosíntesis se estudió a partir de medidas de asimilación (*A*) en el ensayo de variedades de olivar (sin niveles de estrés hídrico), mostraron resultados consistentes y obteniendo  $r^2=0.71$ .

**Palabras Clave:** Fluorescencia, aerotransportado, FluorMOD, *in-filling*, hyperspectral

**Abstract**

Progress in assessing the feasibility for imaging fluorescence using the O<sub>2</sub>-A band with 1 nm full-width half-maximum (FWHM) bands centered at 757.5 and 760.5 nm is reported in this paper. Multispectral airborne data was acquired at 150 m above ground level in the thermal, visible and near infrared regions yielding imagery at 15 cm spatial resolution. Simultaneous field experiments conducted in olive, peach, and orange orchards (water stress trials), and an olive orchard (variety trial) enabled the detected variability in fluorescence emission to be examined as function of stress status. In a parallel modelling activity the coupled leaf-canopy reflectance-fluorescence model, FluorMOD, was used to assess fluorescence retrieval capability by the *in-filling* method, as well as by fluorescence indices from the published literature. Fluorescence retrievals using the *in-filling* method, the derivative index D702/D680 and reflectance indices R690/R630, R761-R757, and R761/R757 yielded the best results in the simulation study, while demonstrating insensitivity to leaf area index (LAI) variation. The fluorescence *in-filling* method, derivative index D702/D680, and R761-R757 were the indices least affected by chlorophyll *a+b* (Cab) variation. On the other hand, other published indices for fluorescence detection at leaf and canopy levels exhibited high sensitivity to variations in Cab and LAI, and therefore were considered less suitable for in-field fluorescence detection. The fluorescence signal extraction from airborne imagery using the *in-filling* method was validated through comparisons with field-measured steady-state fluorescence (Fs) using the PAM-2100 and GFS-3000 instruments, confirming simulation predictions. The water-stress experiments conducted on olive and peach orchards demonstrated the feasibility of chlorophyll fluorescence (F) extraction at the tree level from the airborne imagery, yielding determination coefficients  $r^2=0.57$  (olive), and  $r^2=0.54$  (peach). Consistent results were obtained between airborne F and ground truth assimilation (A) measured in the olive variety field experiment under no water stress levels, yielding  $r^2=0.71$ .

**Keywords:** Fluorescence, airborne, FluorMOD, *in-filling*, hyperspectral

## **1. Introduction**

The early detection of water stress has been long identified as critical to avoid yield losses in crops, which can be affected even by short-term water stress deficits (Hsiao *et al.*, 1976). Water stress is developed in crops when the evaporative demand exceeds the supply of water from the soil (Slatyer, 1967). A remote sensing indicator for water stress detection was successfully demonstrated in the seventies with near-field thermal infrared radiation (Idso *et al.*, 1978; 1981; Jackson *et al.*, 1977; 1981; Jackson & Pinter, 1981) and more recently with high-resolution airborne thermal imagers flown over orchard crops (Sepulcre-Cantó *et al.*, 2006; 2007). The successful detection of water stress using the thermal region is in response to the canopy transpiration changes, where canopy temperature increases with reductions in evaporative cooling.

In addition to canopy temperature, other physiological and structural indicators have been proposed for remote sensing detection of water stress, such as wilting (Bradford & Hsiao, 1982), loss of leaf area (Bradford & Hsiao, 1982; Wolfe *et al.*, 1983) and chlorophyll content (Björkman & Powles, 1984). Leaf water content is proposed as the amount of water per unit leaf area, and remote sensing indices such as a water band index (WBI) (Peñuelas *et al.*, 1993; 1997), a moisture stress index (MSI) (Rock *et al.*, 1986) or the normalized difference water index (NDWI) (Gao, 1996) have been shown to track water content at the canopy level. Nevertheless, changes in leaf water content only occur at advanced stages of dehydration in many (but not all) species, therefore representing a parameter of limited interest for predicting crop water status. A more valuable goal is to develop *pre-visual* indicators of stress, i.e. before the onset of severe stress. Suggested *pre-visual* indicators of stress are the physiological reflectance index (PRI) which is sensitive to xanthophyll pigment detection under water stress conditions (Thenot *et al.*, 2002; Peguero-Pina *et al.*, 2008; Suarez *et al.*, 2008; Suarez *et al.*, 2009), and solar-induced chlorophyll fluorescence emission (Flexas *et al.*, 1999; 2000; 2002; Moya *et al.*, 2004) due to the strong correlation demonstrated between steady-state chlorophyll fluorescence  $F_s$  and stomatal conductance. In addition, several studies have assessed the relationship of chlorophyll fluorescence with photosynthesis and plant physiological status (Papageorgiou, 1975; Krause and Weis, 1984; Schreiber and Bilger, 1987; Lichtenthaler and Rinderle, 1988; Lichtenthaler, 1992; Larcher, 1994; Schreiber *et al.*, 1994).  $F_v/F_m$ ,  $\Phi_{PSII}$  (Yield),  $qP$ ,  $\Phi_{exc}$ , and NPQ (or  $qN$ ) are the chlorophyll fluorescence parameters most frequently used to characterize the functioning of the photosynthetic apparatus under non-stress and stress conditions (see Morales *et al.*, 1991, 1998, 2000; and Abadía *et al.*, 1999 and Morales *et al.*, 2006 for reviews). Although comparatively steady-state chlorophyll fluorescence  $F_s$  has received much less attention, its potential importance for chlorophyll fluorescence detection using remote sensing

methods has been recently emphasized (Soukupová *et al.*, 2008), along with increasing scientific interest during the past five years.

Several publications have described reflectance indices potentially related to incremental effects of fluorescence emission as an addition to leaf and canopy reflected signal. In particular, indices related to fluorescence emission bands at 685 and 740 nm have been proposed to assess the relationship between apparent reflectance and chlorophyll fluorescence at both leaf and canopy levels (Zarco-Tejada *et al.*, 2000a; 2000b), while attempting to minimize structural effects and chlorophyll content sensitivity to thereby derive robust fluorescence indices.

At the laboratory level, results in diurnal studies have shown that optical indices  $R_{680}/R_{630}$ ,  $R_{685}/R_{630}$ ,  $R_{687}/R_{630}$  and  $R_{690}/R_{630}$  were sensitive to  $F_v/F_m$  measured in leaves. Such indices which are sensitive to changes in the curvature in the red reflectance region as a response to the effects of both PSI and PSII fluorescence emission on leaf reflectance also showed a correlation with diurnal changes in  $F_v/F_m$  (Zarco-Tejada *et al.*, 2000a; 2000b). At the canopy level in the laboratory and under natural light conditions, red edge indices were assessed for detection of chlorophyll fluorescence, including red edge spectral derivative indices  $D_{730}/D_{706}$ ,  $DP_{21}$  ( $D\lambda_p/D_{703}$ ), where  $\lambda_p$  is the inflection point of the reflectance spectrum in the red edge spectral region, and the curvature index  $R_{683}^2/(R_{675}\cdot R_{691})$ , which are both also related with chlorophyll a+b (Cab) content. In subsequent studies Zarco-Tejada *et al.* (2000b; 2003) suggested that a *double peak* feature in the 690-710 nm spectral region seen in the derivative reflectance was possibly due to the combined effects of fluorescence emission and low Cab content on stressed vegetation, implying potentially important applications in vegetation stress detection using passive hyperspectral remote sensing methods. Reflectance difference measures and derivative indices  $D_{705}/D_{722}$ ,  $DP_{22}$  ( $D\lambda_p/D_{720}$ ), and  $DPR_1$  ( $D\lambda_p/D\lambda_p+12$ ), were associated with water and heat stress conditions, observed during the recovery after the diurnal experiment (Zarco-Tejada *et al.*, 2003).  $DP_i$ , calculated as  $(D_{688}\cdot D_{710})/D_{697}^2$ , and the area of the double-peak feature,  $Adp$ , were shown to track steady-state fluorescence  $F_s$  variation during both short and long-term stress induction stages in these canopy-level laboratory experiments.

Recent studies have demonstrated the fluorescence *in-filling* of the  $O_2$ -A atmospheric oxygen absorption band at 760 nm, as a detectable radiance signal at the near-canopy levels (Evain *et al.*, 2004; Moya *et al.*, 2004; Liu *et al.*, 2005; Pérez-Priego *et al.*, 2005). At the airborne and far-field scales, Maier *et al.* (2002) and Zarco-Tejada *et al.* (2004) reported the potential detection of the solar-induced fluorescence signal on apparent reflectance obtained from airborne sensors *Reflective Optics System Imaging Spectrometer* (ROSIS) and *Compact Airborne Spectrographic Imager* (CASI) based on the *in-filling* of fluorescence in

the 760 nm atmospheric oxygen absorption band. However, no field validations were available in these studies to fully support the hypothesis presented.

On the modeling side, chlorophyll fluorescence effects on apparent reflectance at the leaf level were simulated with the *Fluorescence-Reflectance-Transmittance* (FRT) model (Zarco-Tejada *et al.*, 2000a) and with the *Stochastic model for Leaf Optical Properties* (Maier *et al.*, 1999; Maier, 2000). However, it was recognized that for simulation of chlorophyll fluorescence effects on apparent reflectance at the canopy-level one needed to account for canopy scattering, within-canopy light level changes and viewing geometry effects. In response to this need, an integrated leaf-canopy model, the *Vegetation Fluorescence Canopy Model* (FluorMOD), was developed through a project funded by the European Space Agency (ESA) (<http://www.ias.csic.es/fluormod>). The FluorMOD project (Miller *et al.*, 2004) coordinated the development of a leaf model FluorMODleaf (Pedrós *et al.*, 2004; 2008) to simulate leaf fluorescence and a linked leaf-canopy model FluorSAIL (Verhoef, 2005) to simulate canopy fluorescence and scattered radiance, which were linked through an integrated interface FluorMODgui (Zarco-Tejada *et al.*, 2006). This linked leaf-canopy FluorMOD model can be used to simulate diurnal effects of natural fluorescence on apparent canopy reflectance under varying viewing geometries, atmospheric characteristics and illumination dependence. Although the model requires further validation and refinement, currently FluorMOD can be used as a tool for understanding trends in leaf and canopy effects on fluorescence emission as function of viewing geometry and leaf and canopy inputs.

To make progress on the current status of our understanding of the potential for detection of solar-induced fluorescence signals in the presence of vegetation reflectance signatures, new research efforts requiring high spatial resolution imagery acquired at high spectral resolution are needed to validate fluorescence-sensitive red edge indices and *in-filling* signals for canopy chlorophyll fluorescence detection. The most definitive assessment of the viability of methods to retrieve the weak fluorescence signal can be made with high resolution imagery targeting pure vegetation crowns without canopy architecture/closure effects, which it turns out are consistent with the assumptions made in developing the FluorMOD model. In addition, if frequent imagery acquisition is available to capture diurnal changes in water stress through short-term studies, as suggested in Berni *et al.* (2009) who used *unmanned aerial vehicle* (UAV) platforms for operational remote sensing in agricultural applications, then experimental research can examine above-canopy fluorescence detection methods as a function of changing stress status. This manuscript describes the results of such research aimed at making such progress through both simulation studies and airborne measurements. The FluorMOD reflectance-fluorescence model was used to provide an assessment

of the suitability and sensitivity of fluorescence reflectance indices, as well as the *in-filling method*. This was complimented by data from airborne and field research to provide an assessment of the feasibility of detecting and imaging fluorescence using 1 nm FWHM bands at 757.5 and 760.5 nm with 15 cm spatial resolution, with a comparison to temperature changes detected with a thermal imager of 40 cm resolution onboard an UAV platform.

## 2. Materials and Methods

### 2.1. Assessing the sensitivity of fluorescence indices and the *in-filling method* using the FluorMOD simulation model

#### 2.1.1. Chlorophyll fluorescence detection with the *in-filling method*

The method to detect fluorescence emission based on the *in-filling method* was reported by McFarlane *et al.* (1980) in measurements of solar-induced natural fluorescence in vegetation canopies using the Fraunhofer H- $\alpha$  line at 656 nm, and Carter *et al.* (1990, 1996a; 2004) using H- $\alpha$  and the O<sub>2</sub>-B atmospheric bands in leaf measurements. They also investigated the relationship between fluorescence and vegetation temperature at the image level as an indicator of plant stress (Carter *et al.*, 1996b). More recent studies provided evidence for fluorescence *in-filling* of the O<sub>2</sub>-A atmospheric oxygen absorption band at 760 nm, as a detectable feature in the radiance spectra at the near-canopy levels (Evain *et al.*, 2004; Moya *et al.*, 2004; Liu *et al.*, 2005; Pérez-Priego *et al.*, 2005). The *in-filling method* uses the canopy radiance from *fluorescing* (vegetation) and *non-fluorescing* (soil) targets *in* and *out* of the oxygen line at 760.5 nm, defined as  $L_i^v, L_i^n, L_o^v, L_o^n$  respectively, to calculate reflectance R and fluorescence F (Equations 2.1 and 2.2).

$$R = \frac{L_o^v - L_i^v}{L_o^n - L_i^n} \quad [2.1]$$

$$F = L_i^v - R \cdot L_i^n \quad [2.2]$$

This method was successfully used by Meroni *et al.* (2008a) at the leaf level, and at a canopy level by Moya *et al.* (2004) and Meroni *et al.* (2008b), showing that fluorescence emission can be detected using the O<sub>2</sub>-A band at the leaf level and on a corn canopy under diuron herbicide penetration. Also, experiments conducted with narrow-band spectrometers (0.065 nm FWHM) (Pérez-Priego *et al.*, 2005) showed that the observed canopy-level fluorescence *in-filling* with the O<sub>2</sub>-A band at 760.5 nm was able to track the water stress status in orchard trees, demonstrating a link between *steady-state* chlorophyll

fluorescence ( $F_s$ ,  $F_t$ ) and *in-filling* of the 760 nm apparent reflectance of individual trees.

At the airborne scale, Maier *et al.* (2002) proposed an approach based on the *in-filling* method for the detection of the solar-induced fluorescence signal on apparent reflectance obtained from the airborne sensor *Reflective Optics System Imaging Spectrometer* (ROSIS) to estimate the *in-filling* of the 760 nm atmospheric oxygen absorption band by fluorescence emission. The method for *far-field* fluorescence detection through *in-filling* at the 690 and 762 nm oxygen bands requires the variables for the radiation flow (Maier *et al.*, 2002; Zarco-Tejada *et al.*, 2004). This method includes the influence of atmospheric transmittance between the target and the sensor along the view direction ( $T_v$ ), the path radiance ( $L^{path}$ ), and the global irradiance ( $E_G$ ) at the scene target. The radiance *in* and *outside* the 762 nm oxygen absorption feature for non-fluorescing targets ( $L_o^n, L_i^n$ ) are defined as,

$$L_o^n = \left( \frac{R_n E_{Go}}{\pi} \right) T_{Vo} + L_o^{path} \quad [2.3]$$

$$L_i^n = \left( \frac{R_n E_{Gi}}{\pi} \right) T_{Vi} + L_i^{path} \quad [2.4]$$

with the relationship between  $L_i^n$  and  $L_o^n$  as,

$$L_i^n = k_1 \cdot L_o^n + k_2 \quad [2.5]$$

where,

$$k_1 = \frac{T_{Vi} E_{Gi}}{T_{Vo} E_{Go}} ; k_2 = L_i^{path} - k_1 \cdot L_o^{path} \quad [2.6]$$

In the case of fluorescing targets, such as vegetation, the radiance *in* and *outside* the oxygen absorption band are,

$$L_o^v = \left( \frac{R_v E_{Go}}{\pi} + L_f \right) \cdot T_{Vo} + L_o^{path} \quad [2.7]$$

$$L_i^v = \left( \frac{R_v E_{Gi}}{\pi} + L_f \right) \cdot T_{Vi} + L_i^{path} \quad [2.8]$$

with the relationship between  $L_i^v$  and  $L_o^v$  as,

$$L_i^v - k_3 \cdot L_f = k_1 \cdot L_o^v + k_2 \quad [2.9]$$

where  $k_1$  and  $k_2$  are as in [6] and ,

$$k_3 = T_{vi} - k_1 \cdot T_{vo} \quad [2.10]$$

Therefore, coefficients  $k_1$  and  $k_2$  can be calculated from [2.5] using a set of non-fluorescing targets, enabling the calculation of fluorescence  $L_f$  from [2.9] for fluorescing targets, such as vegetation.

### 2.1.2. Fluorescence retrieval assessment using FluorMOD simulation

Through the FluorMOD project (Miller *et al.*, 2004) a linked leaf-canopy model was developed that simulates chlorophyll fluorescence emission. The leaf model, FluorMODleaf (Pedrós *et al.*, 2004) is linked to a canopy model, FluorSAIL (Verhoef, 2005), incorporating an excitation-fluorescence matrix, computed externally by means of the leaf-level fluorescence model, to simulate the fluorescence effects on the canopy signature (detailed information on the linked leaf-canopy models can be found in Zarco-Tejada *et al.* (2006)).

The inputs to the leaf model are the number of layers in PROSPECT (N); chlorophyll a+b content in  $\mu\text{g}/\text{cm}^2$  ( $C_{ab}$ ); water equivalent thickness in cm ( $C_w$ ); dry matter content in  $\mu\text{g}$  ( $C_m$ ); fluorescence quantum efficiency ( $F_i$ ); leaf temperature in degrees Celsius (T); species temperature dependence (S) (after Agati, 1998); and stoichiometry of PSII to PSI reaction centers (Sto), which depends on species and light conditions during plant growth. The canopy model requires the viewing zenith angle in degrees (Vza), relative azimuth angle in degrees (Raz), the canopy leaf area index (LAI), the hot spot parameter (h), and the leaf inclination distribution function (LIDF) parameters,  $LIDF_a$  and  $LIDF_b$ . In addition, the canopy model requires a soil spectrum, and four outputs from the leaf model: leaf reflectance without fluorescence (RN), leaf transmittance without fluorescence (TN), and the upward (FuN) and downward (FdN) fluorescence matrices.

The FluorMOD model was used in this study to assess the sensitivity of reflectance indices described earlier, as a function of fluorescence emission, leaf chlorophyll concentration, and canopy leaf area index. The model simulates irradiance (E) and canopy radiance (L) at 1 nm resolution (Figure 2.1), reproducing the fluorescence *in-filling* at O<sub>2</sub>-A and O<sub>2</sub>-B bands using atmospheric, leaf and canopy inputs (Table 2.1). The simulated leaf fluorescence, both reflected and transmitted (Figure 2.2a), provides the expected effects at leaf level in the 650-850 nm spectral region (Zarco-Tejada *et al.*, 2000a; 2003) as extracted by the reflectance difference method (Figure 2.2b).

**Table 2.1.** FluorMOD model inputs used in this study to assess the sensitivity of reflectance indices using atmospheric, leaf and canopy inputs.

<b>Atmospheric Parameters</b>			
Atmospheric file			FLUORMOD30V23.MEP
Irradiance	PAR dependence parameters:		PARb=0.0035; PARre=0.005
Visibility			23 km
Solar zenith angle			30°
Viewing zenith angle			0°
Relative azimuth angle			0°
<b>Leaf Inputs</b>			
N	1.8	Fi	0.06
Cab	30 µg/cm <sup>2</sup>	T	10°C
Cw	0.025 cm	S	broad bean
Cm	0.01 g/cm <sup>2</sup>	Sto	1.5
<b>Canopy Inputs</b>			
Leaf area index			4
LIDF parameter a			-0.5
LIDF parameter b			-0.5
Hot spot parameter			0.1
Soil spectrum			

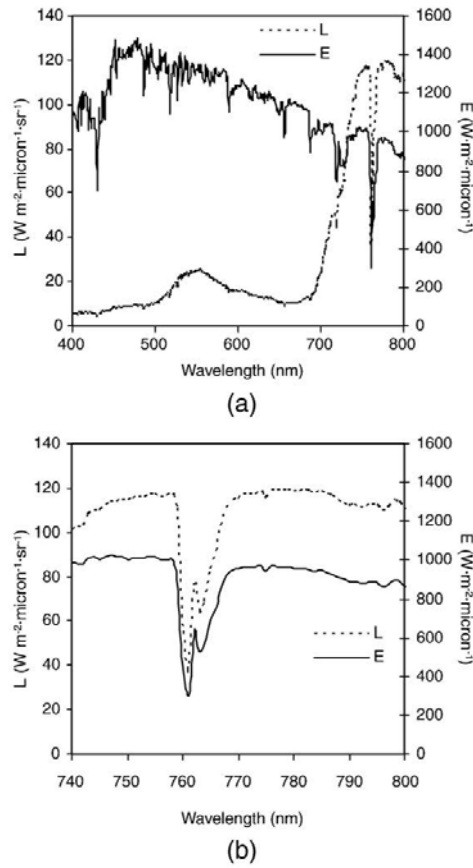


**Figure 2.1.** FluorMOD model simulation of irradiance (E) and canopy radiance (L) at 1 nm resolution in the 400-800 nm range (a) and 740-800 nm (b), reproducing the fluorescence in-filling at O2 A and O2-B bands using atmospheric, leaf and canopy inputs from Table 2.1.

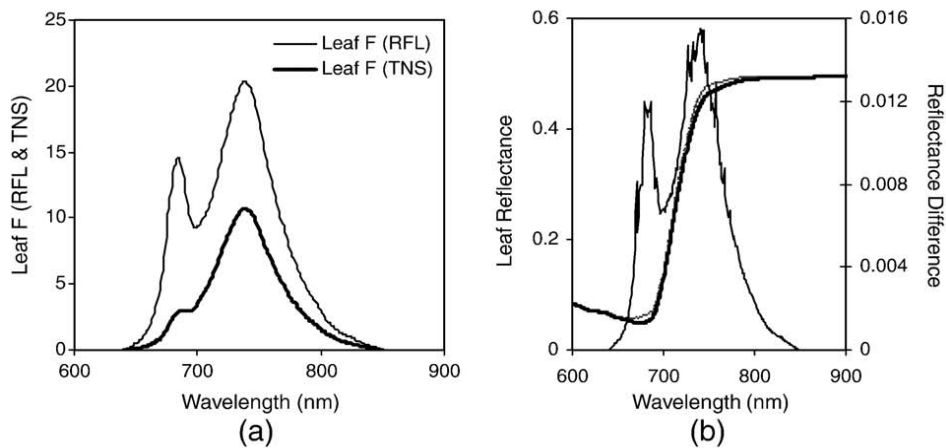


**Figure 2.2.** (a) FluorMOD leaf fluorescence, both reflected (RFL) and transmitted (TNS), for a simulated leaf with  $F_i=0.049$  and  $Cab=43 \mu\text{g}/\text{cm}^2$ ; (b) leaf reflectance with added simulated fluorescence (thin line) and without fluorescence (thick line), showing the reflectance difference

The simulated irradiance and canopy radiance with and without fluorescence effects (inputs from Table 2.1) enables the assessment of the fluorescence peak experimentally observed in canopy reflectance (Figure 2.3a; b). Canopy-level fluorescence effects are observed along the red edge region and particularly as an *in-filling peak* centered at 760.5 nm (Figure 2.3b) when compared with the canopy reflectance without fluorescence effects. The fluorescence radiance (Figure 2.3c) superimposed on the apparent canopy reflectance can be extracted by a reflectance difference calculation (Figure 2.3d), showing larger effects due to fluorescence emission at the 760 nm oxygen band (ca. 3% in this simulation example) as compared with the fluorescence emission for the rest of the spectral region (ca. 1.8% at the 735 nm band).

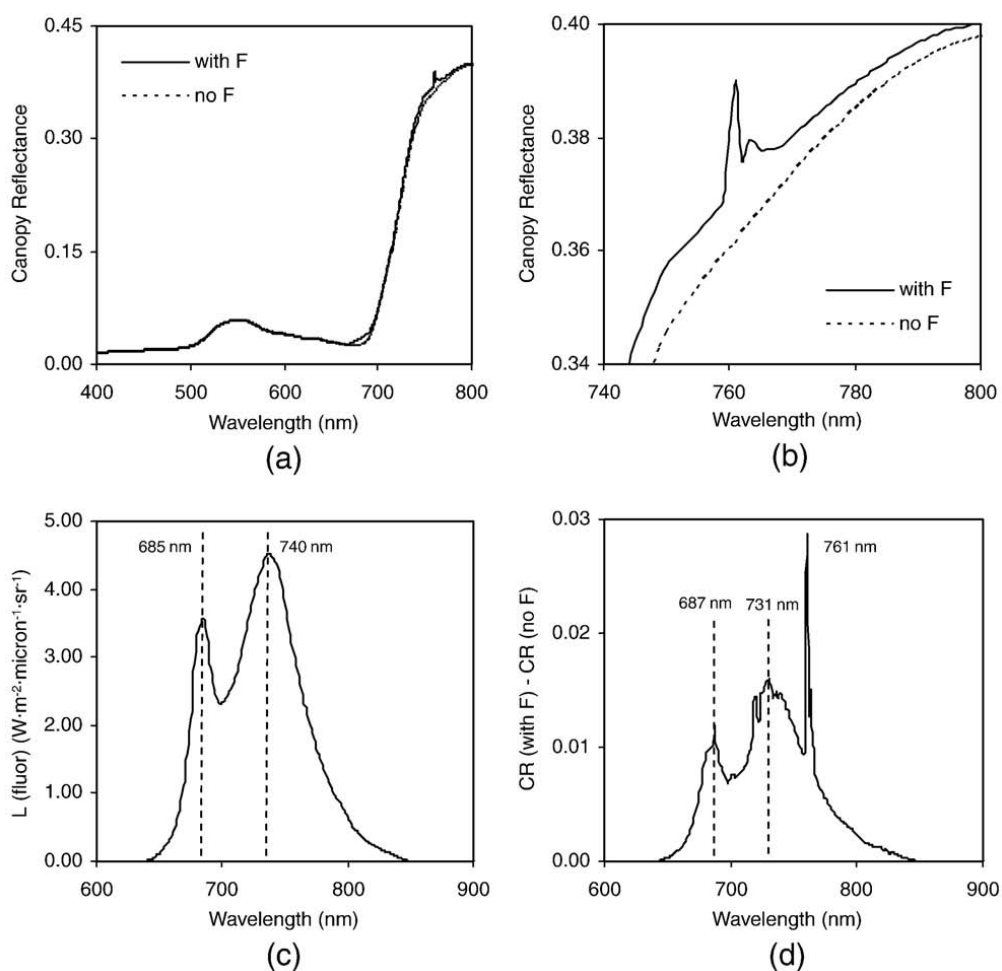


**Figure 2.3.** Simulated canopy reflectance in the 400-800 nm range (a) and 740-800 nm (b) with (with F) and without (no F) fluorescence effects (inputs from Table 2.1). Fluorescence radiance ( $\text{W}\cdot\text{m}^{-2}\cdot\text{micron}^{-1}\cdot\text{sr}^{-1}$ ) (c) added to the canopy reflectance is extracted by reflectance difference calculation (d).

The effects of chlorophyll fluorescence on derivative reflectance could also be assessed using FluorMOD for comparison with previous results obtained experimentally in the laboratory or under natural light conditions. The fluorescence radiance corresponding to  $F_i=0.049$ ,  $C_{ab}=43 \mu\text{g}/\text{cm}^2$  and  $LAI=3.6$

(other inputs from Table 2.1) (Figure 2.4a) was used to simulate the derivative canopy reflectance with and without fluorescence effects (Figure 2.4b). Results indicate that the *double-peak* feature previously observed experimentally (Zarco-Tejada *et al.*, 2003) is reproduced in these simulations of the canopy derivative reflectance when fluorescence effects are included. For a more detailed simulation study, the FluorMOD model was used to assess the expected fluorescence effects and fluorescence retrieval capability as function of input parameters  $F_i$ ,  $C_{ab}$  and LAI on: i) the fluorescence *in-filling* method; ii) reflectance indices; and iii) derivative indices; results are reported in Section 3.1.

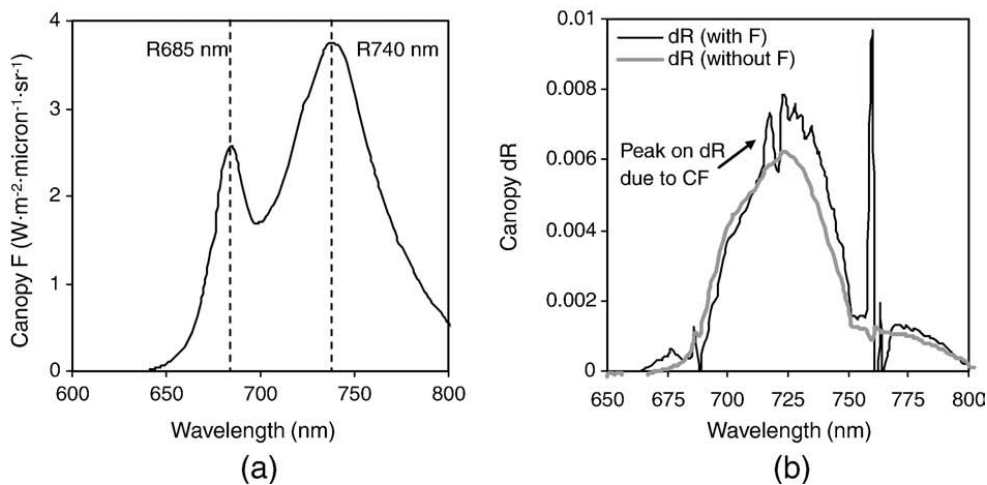


**Figure 2.4.** Simulated fluorescence radiance corresponding to  $F_i=0.049$ ,  $C_{ab}=43 \mu\text{g}/\text{cm}^2$  and  $\text{LAI}=3.6$  (other inputs from Table 2.1) (a) used to simulate the derivative canopy reflectance with and without fluorescence effects (b), showing a *double-peak* feature previously observed experimentally in Zarco-Tejada *et al.* (2003).

## 2.2. Field experiments and airborne campaigns

An airborne multispectral camera with two 1 nm FWHM filters in the 757.5 and 760.5 nm bands, and four 10 nm FWHM bands in the 400-800 nm spectral region was flown over 4 study sites, at 15 cm spatial resolution. Three orchards (peach, orange and olive groves) were used for deficit irrigation experiments to produce a gradient in water stress levels. In addition, a variety trial olive orchard was selected to provide a gradient in chlorophyll concentration and photosynthesis as function of genetic variety conditions.

### 2.2.1. Field data collection

Study sites were located in southern Spain, consisting of *Olea europaea* L. cv. 'Arbequino' (olive), *Prunus persica* L. Batsch cv. 'Baby Gold 8' (peach) and *Citrus sinensis* L. cv. 'Lanelate' (orange) groves planted in regular patterns under drip irrigation. One of the *Olea europaea* L. study sites consisted of a rain-fed variety test field, representing a very heterogeneous grove because of the

large number of varieties planted in comparison to a typical commercial olive orchard. The climate of the area is Mediterranean with an average annual rainfall of 650 mm, concentrated from autumn to spring, and a reference evapotranspiration (ET) of 1390 mm.

The olive, peach and orange orchards belong to a network of study sites irrigated under regulated deficit irrigation (RDI) (Fereres and Soriano, 2007). The olive orchard was irrigated with three drip treatments randomly applied within an area of 6 rows of 18 olive trees (2646 m<sup>2</sup>): i) irrigated at 3.2 mm/day (well irrigated treatment, C); ii) 0.8 mm/day (deficit treatment, S1); and iii) an intermittent treatment, with 1.3 mm/day from 7 May to 15 July and from 24 September to 7 October, stopping irrigation from 15 July to 24 September (deficit treatment, S2). The peach orchard had part of the field under regulated deficit irrigation while the other part had an ample water supply. The RDI part of the orchard received no irrigation until the period of rapid expansion of fruit growth (Phase III), irrigation over full ET for one week and then with constant doses at full ET until harvest. The orange orchard was divided into plots under RDI and full ET irrigation, where the RDI plot received 65% of the water relative to the full ET part of the field.

A Scholander pressure bomb (PWSC Model 3000, Soilmoisture equipment Corp., California, USA) was used to measure leaf water potential weekly on selected trees in each orchard at noon. Stomatal conductance was measured weekly with a leaf steady-state porometer (model PMR-4, PP Systems, Hitchin Herts, Great Britain). Leaf chlorophyll fluorescence measurements were conducted under field conditions using the *Pulse-Amplitude-Modulated Fluorometer* PAM-2100 (Heinz Walz GMBH, Effeltrich, Germany), measuring at the time of flight acquisitions steady-state F<sub>s</sub> fluorescence on 30 leaves per tree on 8 trees (olive orchard), 10 trees (peach orchard), 8 trees (orange orchard), and 13 trees (olive variety field), respectively. Leaf photosynthesis, stomatal conductance and fluorescence were measured using the *Portable Gas Exchange Fluorescence System* GFS-3000 (Heinz Walz GMBH, Effeltrich, Germany) on 2 leaves per tree on 10 trees of the olive variety trial orchard at the time of airborne image acquisition.

### **2.2.2.- Airborne campaigns**

An *unmanned aerial vehicle* (UAV) platform was developed to carry a payload with thermal and multispectral imaging sensors for remote sensing operations (Berni *et al.*, 2009). The multispectral sensor used in this study was a 6-band multispectral camera (MCA-6, Tetracam, Inc., California, USA). The camera consists of 6 independent image sensors and optics with user-configurable spectral filters. The image resolution is 1280x1024 pixels with 10-bit radiometric resolution and optics focal length of 8.5 mm, yielding an angular

FOV of  $42.8^\circ \times 34.7^\circ$  and 15 cm pixel spatial resolution at 150 m flight altitude. The detector used is a CMOS sensor with pixel size  $5.2 \times 5.2 \mu\text{m}$ , image area  $6.66 \text{ mm} \times 5.32 \text{ mm}$ , operated in a progressive scan mode, at 54 dB signal-to-noise ratio, with  $< 0.03\%$  fixed pattern noise, 28 mV/s dark current, and 60 dB dynamic range. Multispectral images acquired over each study site enabled tree identification for field validation purposes on the olive, peach, orange and olive variety trial fields. Different bandsets were selected depending on the objectives adopted for the remote sensing study, including 25 mm diameter bandpass filters of 10 nm FWHM (Andover Corporation, NH, USA), with center wavelengths at 490 nm, 530 nm, 550 nm, 570 nm, 670 nm, 700 nm, 750 nm, and 800 nm, and two 1 nm FWHM filters centered at 760.5 and 757.5 nm bands for fluorescence *in-filling* measurements. Filter transmission measurements were conducted with a Li-Cor 1800-12 Integrating Sphere (Li-Cor, Inc., Lincoln, NE, USA), coupled by a 200  $\mu\text{m}$  diameter single mode fiber to an Ocean Optics model HR2000 spectrometer (Ocean Optics Inc., Dunedin, FL, USA), with a 2048 element detector array, 0.05 nm sampling interval and 0.065 nm spectral resolution in the 678.76-774.05 nm range. Measurements of the 1 nm filters yielded transmissions of 49.2 % and 46.8 %, and bandpasses FWHM=1.57 nm (center wavelength 760.47 nm), and FWHM=1.6 nm (center wavelength 757.42 nm), respectively. For the 10 nm filters measurements yielded ca. 60% transmission and 10.4 nm FWHM.

Study sites were also imaged with the airborne platform using a thermal camera to derive surface temperature of each tree under study. The thermal imager used was the Thermovision A40M (FLIR, USA) equipped with a  $40^\circ$  FOV lens and connected to computer via IEEE-1394 protocol. The image sensor is a Focal Plane Array (FPA) based on uncooled microbolometers with a resolution of  $320 \times 240$  pixels and spectral response in the range  $7.5\text{-}13 \mu\text{m}$ , yielding  $38 \times 38 \mu\text{m}$  pixel size in the  $7.5\text{-}13 \mu\text{m}$  region, with 0.08 K sensitivity at 303 K. The camera delivers digital raw images at 16 bits of *at-sensor* calibrated radiance with a dynamic range of 233 K – 393 K. The sensor implements an internal calibration for *non-uniformity correction* (NUC) and internal temperature calibration. Thermal images from each study site were acquired at 40 cm pixel resolution enabling the retrieval of pure crown average temperature from each tree under study.

Image atmospheric correction and calibration methods were conducted to generate spectral reflectance and surface temperature, respectively. Multispectral image calibration was conducted using the empirical line method (Smith and Milton, 1999) by placing two  $2 \times 2 \text{ m}$  levelled dark and white targets in a central location within the flight path of the UAV platform. Field spectral measurements were taken on the calibration targets with an ASD Field Spectrometer (FieldSpec Handheld Pro, ASD Inc., CO, USA) in the 350-1050 nm

spectral range at the time of image acquisition. The ASD Field Spectrometer was first calibrated using a Spectralon (SRT-99-180, LabSphere, NH, USA) white panel, therefore enabling the calculation of white and dark panel reflectance spectra to be used later for the empirical line calibration method. Calibrated multispectral reflectance imagery at 10 nm FWHM was obtained (Figure 2.5a), while targeting pure components such as crown, shaded and sunlit soil spectra (Figure 2.5b). Field validation campaigns for reflectance retrieval yielded an RMSE=1.17% (n=90) after empirical line methods were applied at each flight time (Berni *et al.*, 2009).

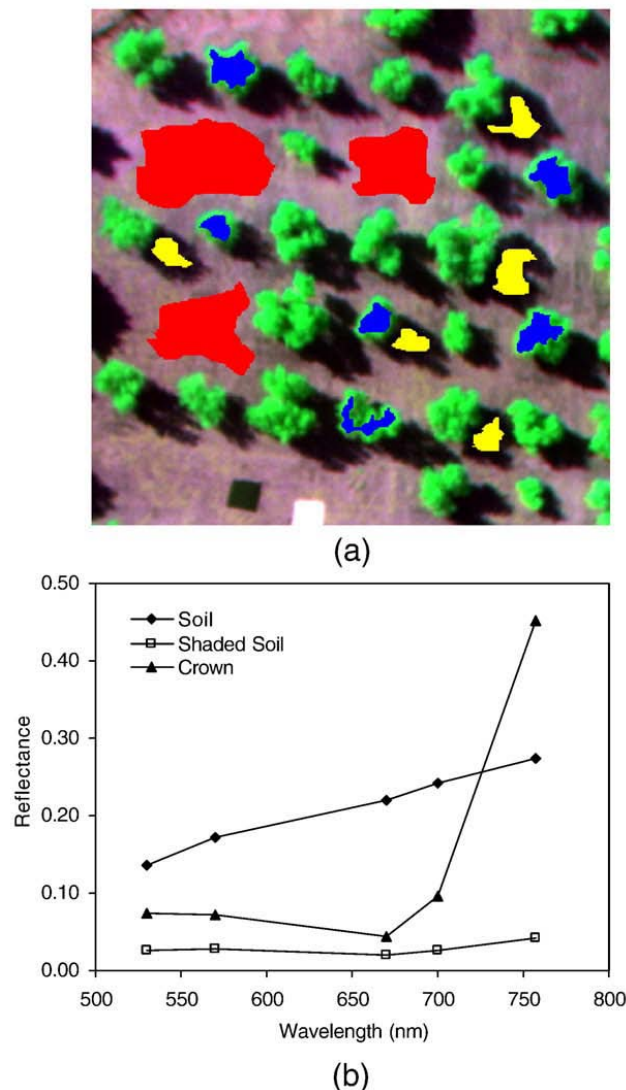


**Figure 2.5.** Multispectral airborne images acquired at 15 cm spatial resolution over each study site on olive orchard (a), peach (b), orange (c) and olive variety trial field (d) with 1 nm FWHM bandwidths on bands used for fluorescence retrievals. Color composite images built from bands 570 nm, 670 nm, and 800 nm.

The 1 nm FWHM multispectral camera bands centered at 760.5 and 757.5 nm later used for the fluorescence *in-filling* retrieval method were calibrated using the Ocean Optics model HR2000 spectrometer (Ocean Optics Inc.,

Dunedin, FL, USA) at 0.065 nm spectral resolution in the 678.76-774.05 nm spectral range. The HR2000 instrument was calibrated to irradiance ( $E_g$ ) in the laboratory with a cosine corrector-diffuser illuminated by the LS-1-CAL calibrated tungsten halogen NIST-traceable light source (Ocean Optics, Dunedin, FL, USA), and calibrated to radiance (L) with the Spectralon panel (Labsphere, North Sutton, USA). Diurnal measurements of the Spectralon (SRT-99-180, LabSphere, NH, USA) white panel radiance were conducted in the field at the time of flight acquisitions (Figure 2.6a) at 0.065 nm spectral resolution in the O<sub>2</sub>-A spectral region (756-774 nm), yielding white and dark target radiance used for airborne image calibration at 760.5 and 757.5 nm bands (Figure 2.6b). Calibrated images at 10 nm FWHM (Figure 2.7a), and 1 nm bandwidth at 757.5 nm (Figure 2.7b) and 760.5 nm (Figure 2.7c) were used to extract radiances from tree crown (fluorescing) and soil (non-fluorescing) targets used to estimate crown chlorophyll fluorescence using the *in-filling* method.

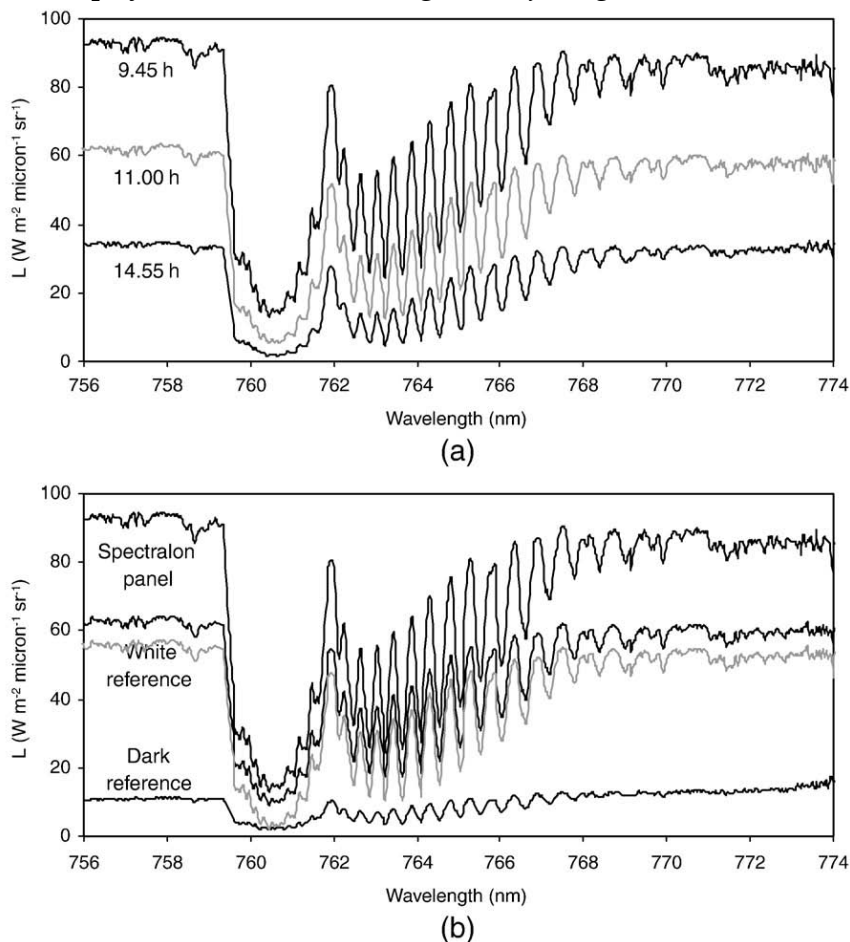


**Figure 2.6.** Diurnal measurements of the white spectralon reference panel radiance conducted at the time of flight acquisitions (a) at 0.065 nm spectral resolution in the O<sub>2</sub>-A spectral region (756-774 nm). White and dark target radiance used for airborne image calibration at 760.5 and 757.5 nm bands (b).

Surface temperature was obtained applying atmospheric correction methods to thermal imager data based on MODTRAN radiative transfer model. Local atmospheric conditions were determined by air temperature, relative

humidity and barometric pressure measurements at the time of flight using a portable weather station (Model WXT510, Vaisala, Finland) and were used as input into the MODTRAN model. A single-layer atmosphere with uniform conditions was considered for the simulations since the variation for the typical UAV flight altitude (150-200 m) could be neglected. Atmospheric correction methods conducted showed the successful estimation of surface temperature images of 40 cm spatial resolution, yielding RMSE < 1 K (Berni *et al.*, 2009).

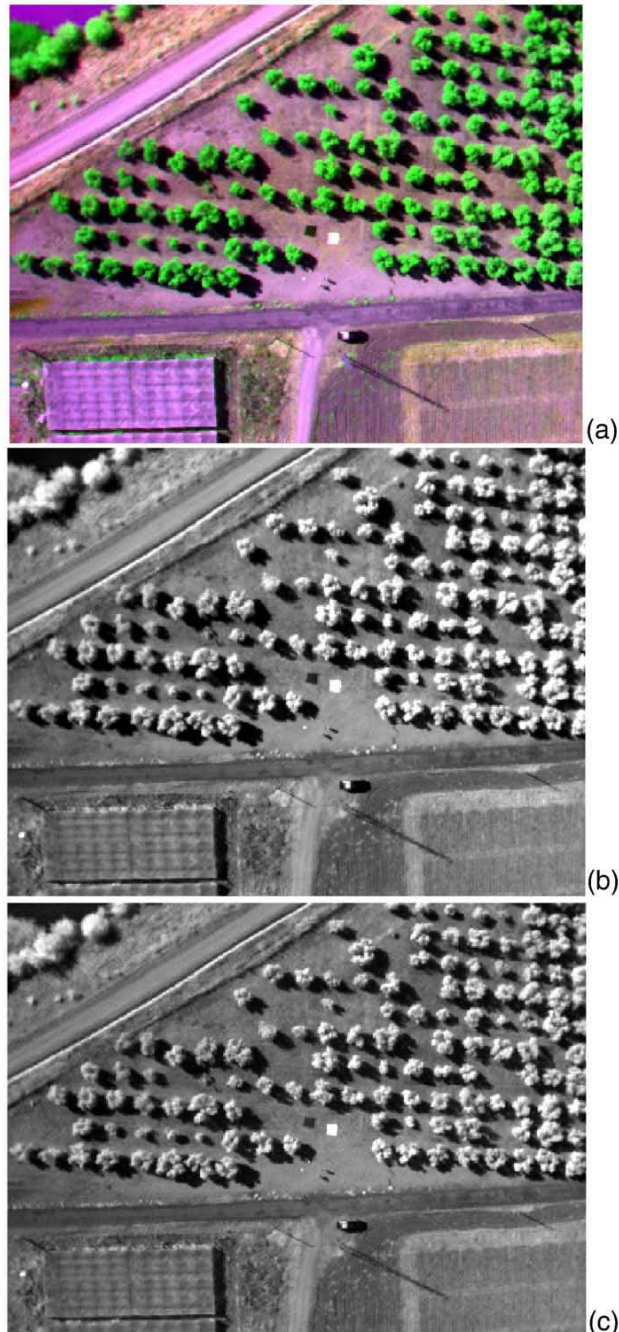


**Figure 2.7.** Calibrated images at 10 nm FWHM (a), and 1 nm FWHM at 757.5 nm (b) and 760.5 nm (c) used to extract crown radiance (fluorescing) and soil radiance (non-fluorescing) targets to estimate crown chlorophyll fluorescence using the *in-filling* method.

### 3. Results

#### 3.1. Simulation Results

The FluorMOD model was used to generate spectra using random input parameters  $F_i$  (0.03-0.06), Cab (30-80  $\mu\text{g}/\text{cm}^2$ ), and LAI (2-4). Leaf fluorescence emission (Figure 2.8a) and leaf reflectance (Figure 2.8b) show a wide range of responses to both fluorescence and chlorophyll content variation in the generated set of synthetic spectra. Fluorescence, chlorophyll and leaf area index effects could be observed on the synthetic canopy radiance generated (Figure 2.9a) and on the simulated canopy reflectance (Figure 2.9b). Canopy derivative reflectance calculations from the synthetic spectra simulated by FluorMOD for the spectra without (Figure 2.9c) and with (Figure 2.9d) fluorescence effects demonstrated the red edge peak shift toward longer wavelengths due to the variation of the chlorophyll content (Figure 2.9c) and the *double-peak* feature observed on the derivative spectra when fluorescence effects are included (Figure 2.9d).

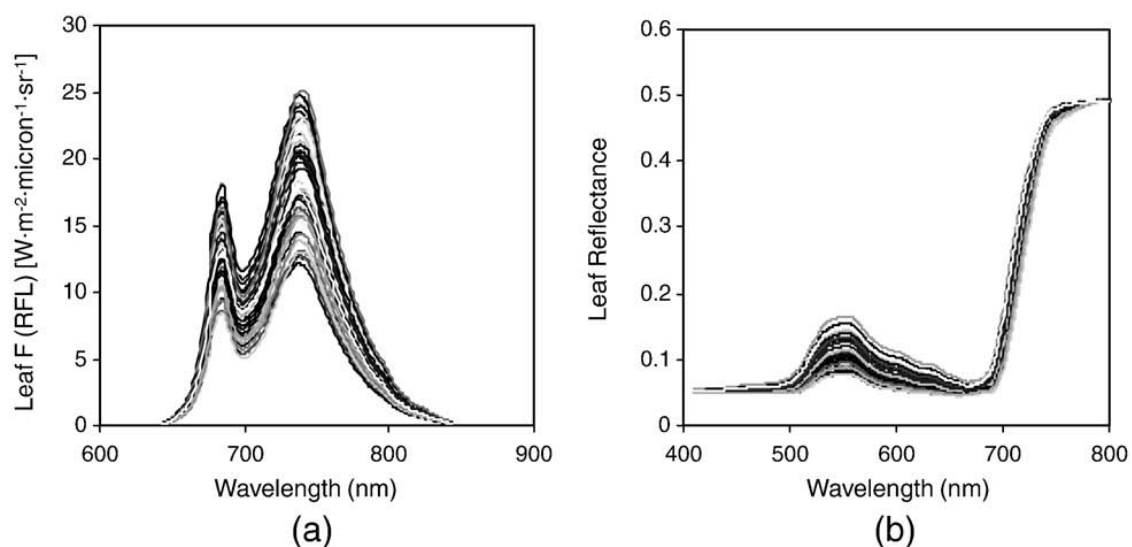


**Figure 2.8.** Synthetic leaf spectra generated with FluorMOD using random input parameters  $F_i$  (0.03-0.06), Cab (30-80  $\mu\text{g}/\text{cm}^2$ ), and LAI (2-4). Leaf fluorescence emission [ $\text{W}\cdot\text{m}^{-2}\cdot\text{micron}^{-1}\cdot\text{sr}^{-1}$ ] (a) and leaf reflectance (b) show a wide range of both fluorescence and chlorophyll content variation.

This set of random synthetic spectra simulated by FluorMOD as function of fluorescence efficiency ( $F_i$ ), leaf chlorophyll concentration (Cab) and canopy leaf area index (LAI) for canopy radiance (Figure 2.9a), canopy reflectance (Figure 2.9b) and canopy derivative reflectance (Figure 2.9d) were used to retrieve fluorescence ( $F$ ) using the *in-filling* method, and to calculate reflectance and derivative reflectance indices sensitive to chlorophyll fluorescence (Table 2.2). The retrieved fluorescence using the *in-filling* method ( $F$ ), and the reflectance and derivative reflectance indices were compared with the canopy radiance fluorescence ( $L(F)_{761}$ ) simulated by FluorMOD. In addition, the

fluorescence retrieval (F) and fluorescence-sensitive indices were compared with input parameters  $F_i$ , Cab and LAI, in order to assess the sensitivity of the retrieved fluorescence (F) and the calculated indices with leaf chlorophyll content and leaf area index (Table 2.2).

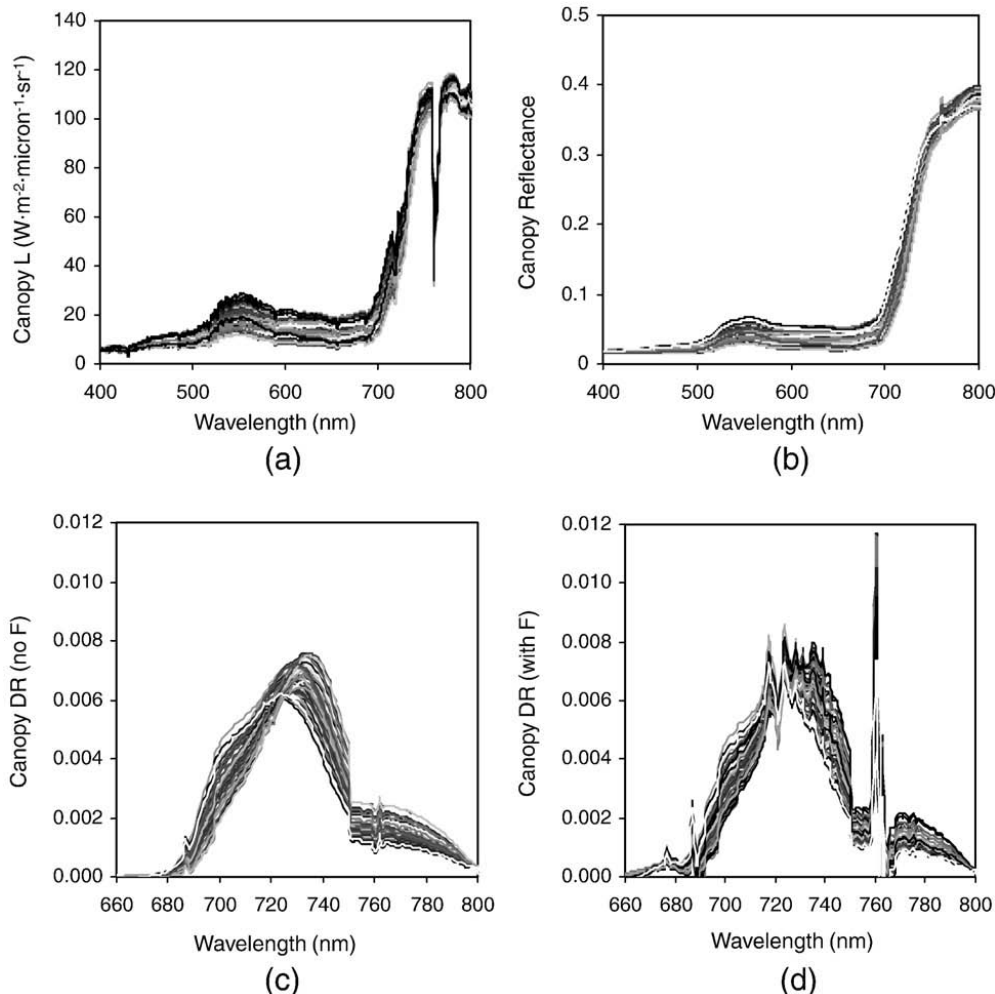


**Figure 2.9.** Simulations conducted with FluorMOD model for parameters  $F_i$  (0.03-0.06), Cab (30-80  $\mu\text{g}/\text{cm}^2$ ), and LAI (2-4) for canopy radiance (a) and canopy reflectance (b). Simulated canopy derivative reflectance without fluorescence (c) and with fluorescence (d) show a peak at 721 nm due to fluorescence effects, a *double-peak* feature previously observed experimentally in Zarco-Tejada *et al.* (2003).

The fluorescence retrievals using the *in-filling* method (F) ( $r^2=0.82$ ) (Figure 2.10a), derivative index  $D702/D680$  ( $r^2=0.78$ ) (Figure 2.10b) and reflectance indices  $R690/R630$  ( $r^2=0.71$ ) (Figure 2.10c),  $R761-R757$  ( $r^2=0.86$ ) (Figure 2.10d), and  $R761/R757$  ( $r^2=0.78$ ) yielded the best results in the simulation study. These indices were found to be insensitive to LAI variation ( $r^2$  with LAI ranged from 0.03 to 0.08), with low Cab sensitivity for the fluorescence *in-filling* method ( $r^2=0.33$  for Cab vs. F),  $D702/D680$  ( $r^2=0.27$  for Cab vs. the index),  $R761-R757$  ( $r^2=0.26$  for Cab vs. the index).

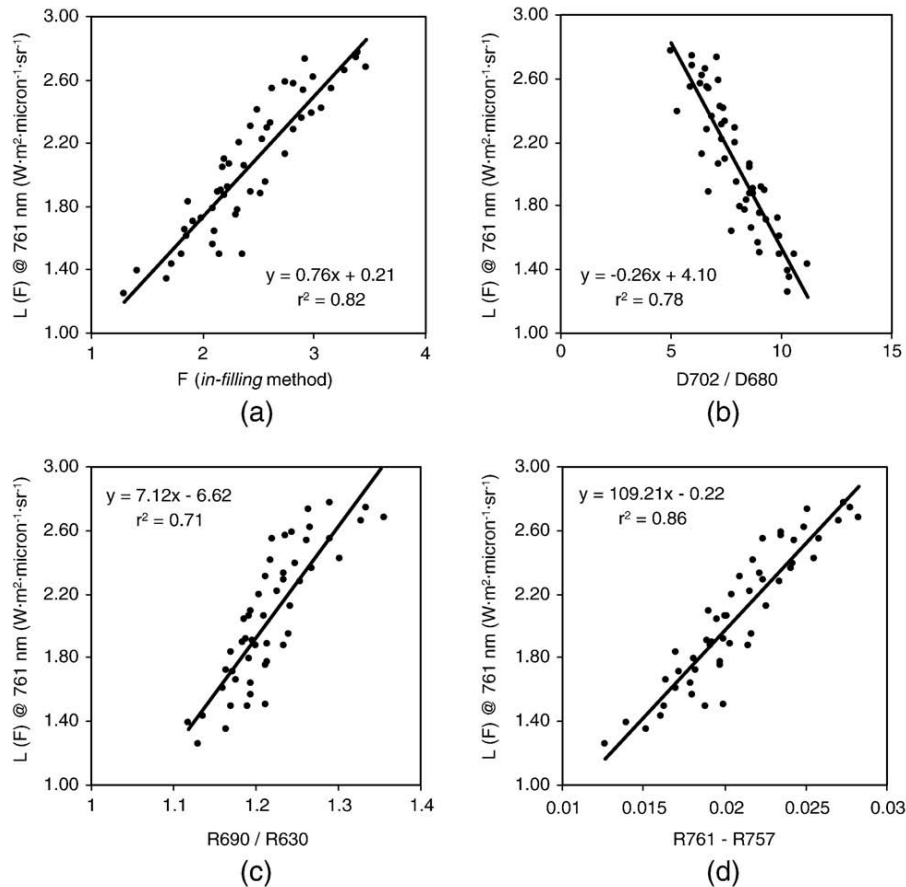


**Figure 2.10.** Fluorescence retrievals from the synthetic canopy reflectance simulations using the *in-filling* method (F) (a), derivative index D702/D680 (b), and reflectance indices R690/R630 (c), and R761-R757 (d).

On the other hand, through this simulation study, other indices generally accepted for fluorescence detection at leaf and canopy levels were found to show high sensitivity to LAI and Cab variations; in particular, R740/R685, R740/R850, R685/R850, R740/R630 were highly affected by LAI ( $r^2$  ranging between 0.89 and 0.97) with little sensitivity to fluorescence. Indices D705/D722, D730/D706, DPi, R735/R850, R680/R630, R685/R630, and the curvature index  $R683^2/(R675 \cdot R691)$  were highly affected by Cab ( $r^2$  ranging between 0.67 and 0.92).

**Table 2.2.** Relationships (determination coefficients calculated as the square of the Pearson product-moment correlation coefficient) obtained between FluorMOD inputs and fluorescence estimates using the *in-filling* method (F), reflectance and derivative reflectance indices sensitive to chlorophyll fluorescence. The synthetic random spectra were generated varying fluorescence efficiency (Fi), leaf chlorophyll concentration (Cab) and canopy leaf area index (LAI).

	Fi	Cab	LAI	Fi·Cab·LAI	Fi·LAI	Fi·Cab	Cab·LAI	L(F) <sub>761</sub>
<i>In-filling</i> method								
<b>F</b>	0.69	<b>0.33</b>	<b>0.05</b>	0.83	0.56	0.81	0.37	<b>0.82</b>
Derivative Indices								
<b>D702/D680</b>	0.78	<b>0.27</b>	<b>0.039</b>	0.46	0.24	0.79	0.07	<b>0.78</b>
D705/D722	0	0.85	0.049	0.41	0	0.38	0.74	0
D730/D706	0	0.92	0.05	0.56	0.04	0.54	0.8	0.04
D735/D680	0.24	0.44	0.12	0.11	0.01	0.03	0.59	0.13
D761/D757	0.58	0.19	0.09	0	0.09	0	0.29	0.41
DPI (D688-D710)/D697 <sup>2</sup>	0.19	0.73	0	0.59	0.08	0.86	0.41	0.26
Reflectance Indices								
<b>R761-R757</b>	0.72	<b>0.26</b>	<b>0.08</b>	0.82	0.64	0.74	0.34	<b>0.85</b>
R750/R710	0	0.54	0.37	0.66	0.21	0.3	0.98	0.04
<b>R690/R630</b>	0.56	<b>0.34</b>	<b>0.07</b>	0.89	0.57	0.75	0.44	<b>0.71</b>
R735/R850	0	0.78	0.16	0.59	0.08	0.41	0.92	0.02
<b>R761/R757</b>	0.65	<b>0.4</b>	<b>0.03</b>	0.84	0.49	0.86	0.39	<b>0.78</b>
R740/R685	0.03	0	0.97	0.15	0.35	0.02	0.34	0
R740/R850	0	0	0.99	0.21	0.49	0	0.35	0.01
R685/R850	0.02	0.02	0.89	0.25	0.34	0	0.5	0
R740/R630	0	0.03	0.92	0.4	0.5	0.01	0.59	0.03
R680/R630	0.27	0.75	0	0.66	0.1	0.87	0.44	0.35
R685/R630	0.35	0.67	0	0.76	0.2	0.89	0.47	0.46
CUR R683 <sup>2</sup> /(R675·R691)	0.27	0.74	0	0.79	0.2	0.85	0.59	0.37

This simulation study demonstrates the retrieval capability of the *in-filling* method even when other common effects such as variations in chlorophyll content and leaf area index are considered. Moreover, it shows that some fluorescence-sensitive indices published in the literature are highly affected by chlorophyll and structural effects.

### **3.2. Experimental results**

Fluorescence extracted per tree from the airborne imagery using the *in-filling* method with the 1 nm FWHM 757.5 and 760.5 nm bands was compared with field-measured chlorophyll fluorescence data on the four orchards. The water-stress experiments conducted on olive and peach orchards demonstrated the feasibility of chlorophyll fluorescence extraction at the tree level from the

airborne imagery, yielding determination coefficients  $r^2=0.57$  (Figure 2.11a, olive), and  $r^2=0.52$  (Figure 2.12, peach). In both cases fluorescence extracted from airborne imagery using the *in-filling* method was compared with field-measured steady-state fluorescence (Fs) using the PAM-2100 instrument. In order to address potential structural effects on fluorescence retrievals from the airborne imagery, such as the influence of tree LAI, crown NDVI was extracted and shown to exhibit no relationship with crown fluorescence extracted from the imagery ( $r^2=0.05$ ; Figure 11b; olive), demonstrating the sensitivity of R757.5 and R760.5 nm bands to fluorescence and the absence of crown LAI influences.

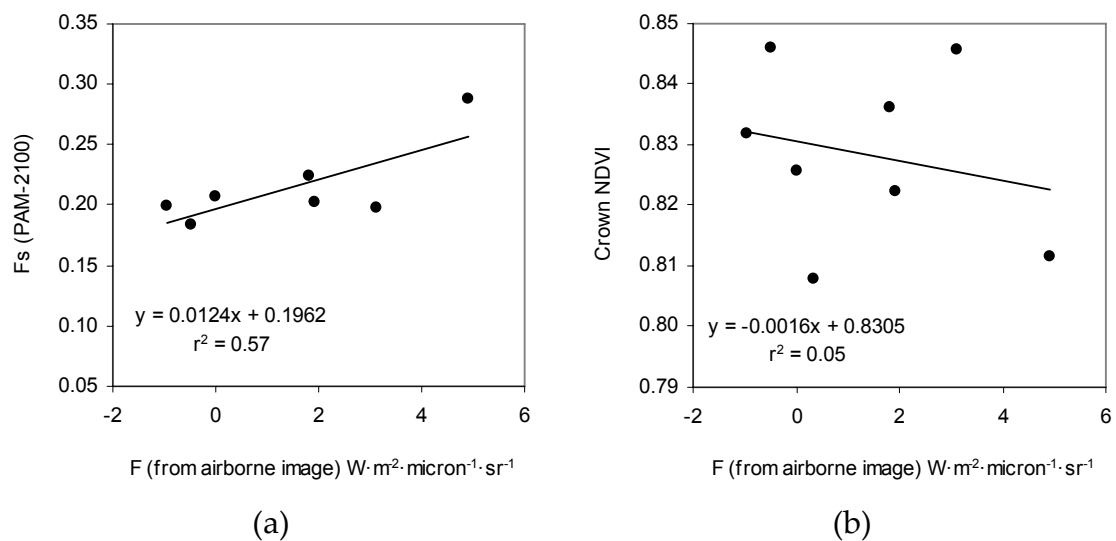


**Figure 2.11.** Relationship obtained between ground-truth Fs (PAM-2100) and fluorescence extracted from the airborne image using the *in-filling* method in a water-stress experiment conducted on an olive orchard (a); crown NDVI showed no relationship with crown fluorescence extracted from the imagery (b) to dismiss structural effects on the fluorescence retrieval.

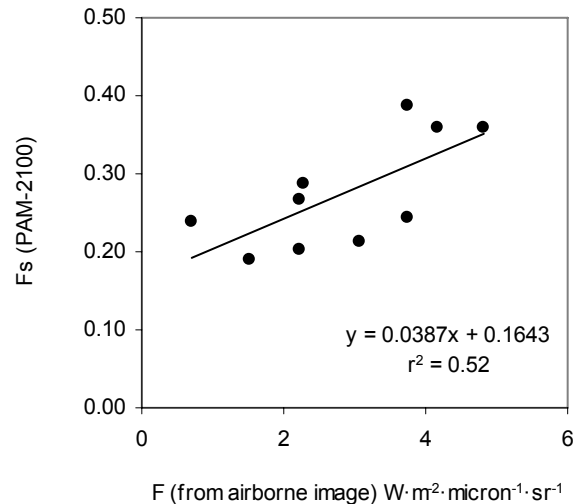


**Figure 2.12.** Relationship obtained between ground-truth  $F_s$  (PAM-2100) and fluorescence extracted from the airborne image using the *in-filling* method in a water-stress experiment conducted on a peach orchard.

The consistency of airborne fluorescence retrievals from trees under water stress condition (higher  $F$  values on full irrigated than deficit-watered trees) was compared with the mean crown temperature estimated from the airborne imagery. The full irrigated peach trees yielded  $F=3.8 W \cdot m^2 \cdot \mu m^{-1} \cdot sr^{-1}$  and crown temperature  $T=309.2 K$ , while deficit irrigation trees yielded  $F=2.2 W \cdot m^2 \cdot \mu m^{-1} \cdot sr^{-1}$  and crown temperature  $T=310.49 K$ . Therefore, full-irrigated trees yielded higher  $F$  and lower  $T$  than deficit-irrigation trees, as expected under water stress conditions (Pérez-Priego *et al.*, 2005; Sepulcre-Cantó *et al.*, 2006). Negative values found in some of the fluorescence *in-filling* estimates when  $F$  is close to 0 (low fluorescence signals) were due to noise levels being similar to the low signals measured, as well as potential image registration displacements between the 757.5 and 760.5 nm bands.

The multispectral airborne images collected at 7.40, 11.00 and 12.50 GMT over the orange orchard showed a consistent trend for both airborne fluorescence  $F$  and field-measured fluorescence using the PAM-2100 instrument (Figure 13). In all cases airborne-estimated  $F$  and PAM-2100  $F_s$  from trees under stress (labelled as 1, 3, 5 in Figure 2.13) yielded lower values than well-irrigated trees (labelled as 2, 4, 6 in Figure 2.13) when collected at the same time. In addition, a decrease in chlorophyll fluorescence over the diurnal interval was consistent with the diurnal change experimentally observed in photosynthesis in the trees under stress, yielding  $r^2=0.6$  (data not shown) between airborne  $F$  and assimilation ( $A$ ) measured in the field with the GFS-3000 instrument.

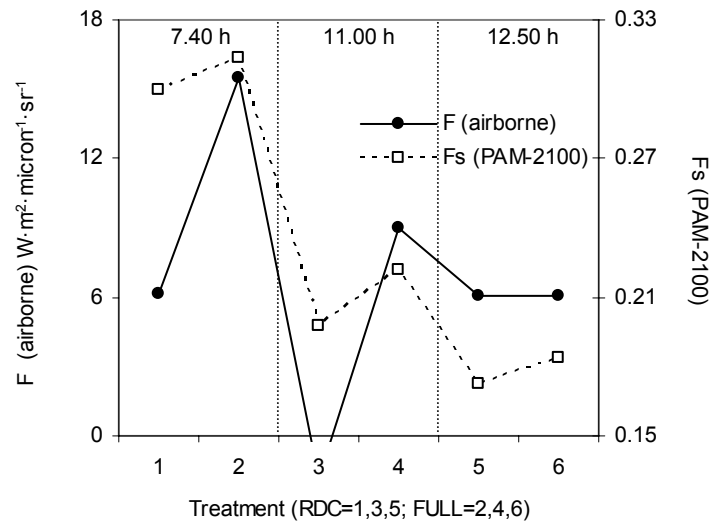


**Figure 2.13.** Diurnal trend for both airborne fluorescence (F) and field measured fluorescence (Fs) using the PAM-2100 instrument acquired at 7.40, 11.00 and 12.50 GMT. Water-stress trees (labelled as 1, 3, 5) yielded lower values than well-irrigated trees (labelled as 2, 4, 6).

Similar results were obtained between airborne F and ground truth assimilation measured in the olive variety field experiment under no water stress levels, yielding  $r^2=0.71$  (Figure 2.14a), and  $r^2=0.54$  between airborne F and Yield (Figure 2.14b). Quenching parameters,  $qP$  and  $qN$  measured with PAM-2100 were related with airborne F, yielding  $r^2=0.29$  and  $r^2=0.21$  respectively, suggesting a link with both photochemical and non-photochemical quenching. This link was further investigated assessing the relationships between airborne F and estimated chlorophyll content with crown T, yielding  $r^2=0.53$  (Figure 2.14c) and  $r^2=0.49$  (Figure 2.14d), respectively. These results demonstrate the physiological link between airborne estimated F and T, and it suggests a successful retrieval of fluorescence at the crown level using the fluorescence *in-filling* method. Results shown in Figure 2.14 are all consistent, except for the direct relationship found between F and T. The hypothesis that could clarify this F vs. T relationship may be explained by the confounding effects caused on both F and T by the different varieties in the trial, which showed variability in Cab and LAI.

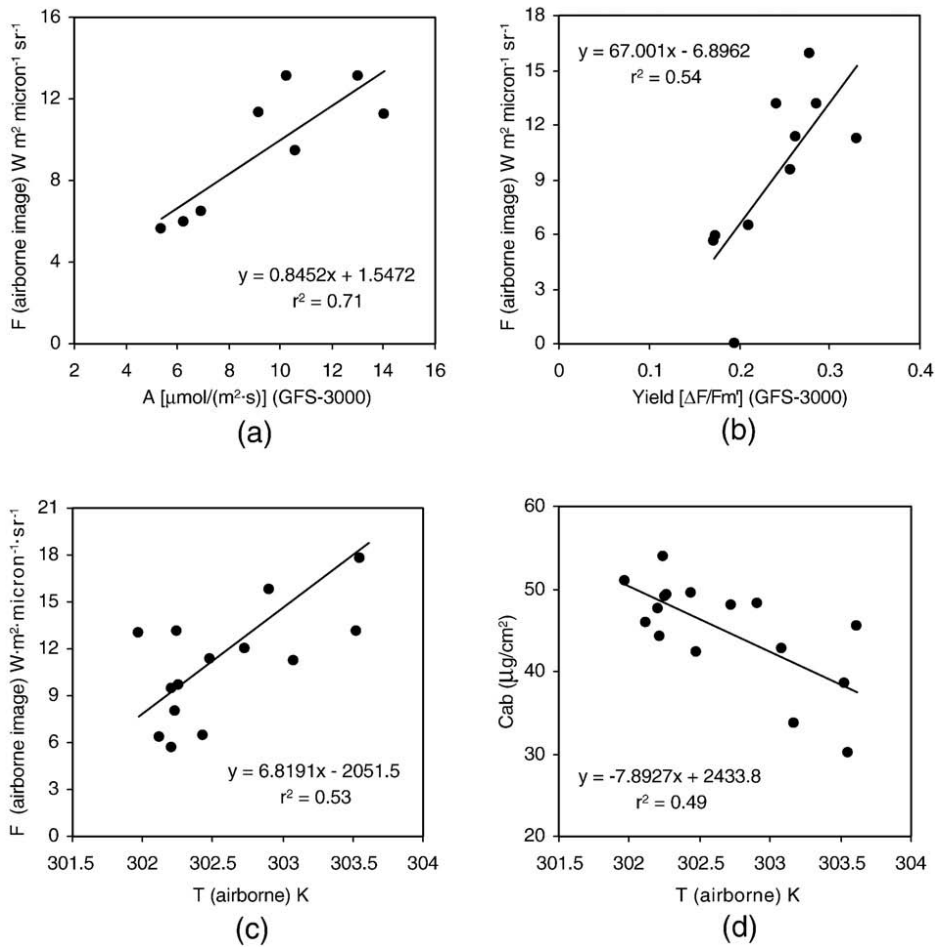


**Figure 2.14.** Results obtained between airborne fluorescence estimates and ground truth assimilation (a) and yield (b) measured in the olive variety trial experiment. Relationships obtained between airborne crown temperature and airborne fluorescence (c) and airborne-estimated chlorophyll content (d).

An image of the fluorescence *in-filling* acquired at 15 cm pixel resolution from the multispectral image (Figure 2.15a) using the *in-filling* method at the crown level was produced, showing the spatial variability of the vegetation fluorescence *in-filling* within the orchard (Figure 2.15b).

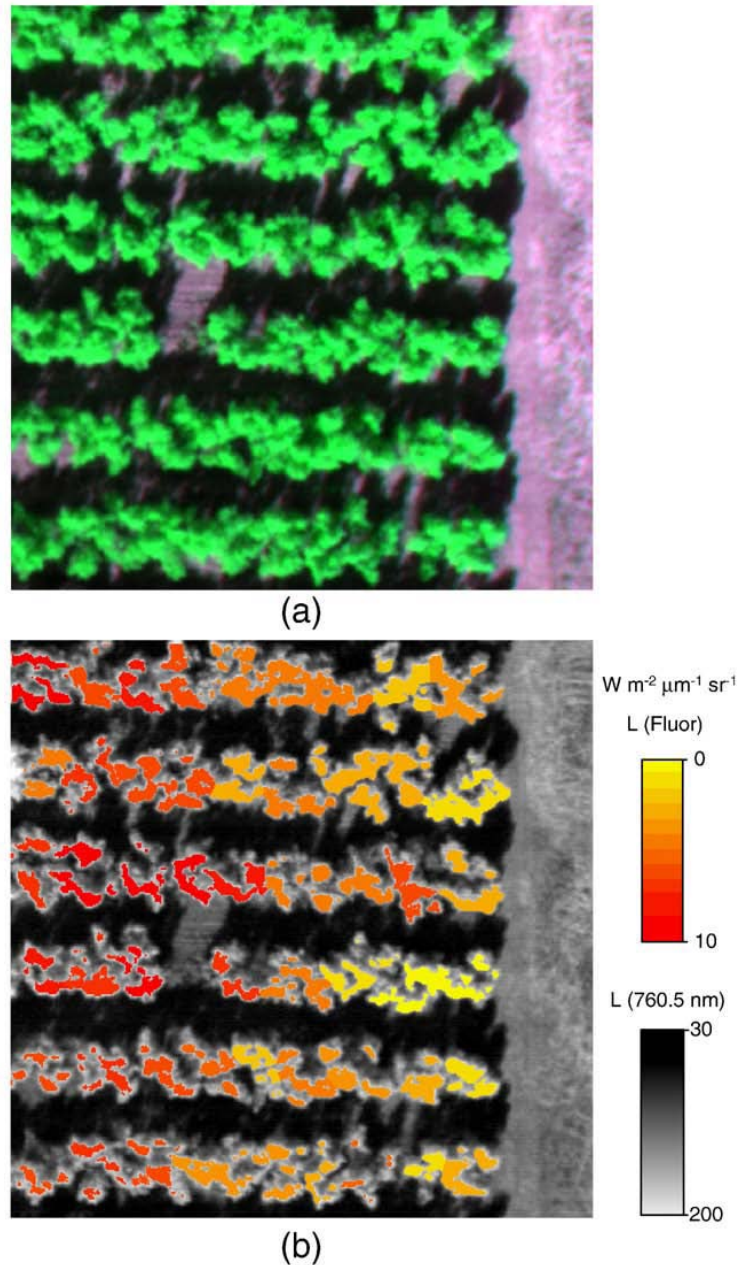


**Figure 2.15.** Image of the fluorescence estimates acquired at 15 cm pixel resolution using the *in-filling* method at the crown level from the multispectral image (a), showing the spatial variability of the vegetation fluorescence *in-filling* within the orchard (b).

#### **4. Conclusions**

The work reported in this manuscript demonstrates that imaging solar-induced chlorophyll fluorescence emission using the *in-filling* method is feasible. The multispectral camera used 1 nm FWHM bands located at 757.5 and 760.5 nm, at 15 cm pixel resolution while flown at 150 m above the crop canopies. Field experiments conducted in olive, peach, orange (water stress trials), and olive orchard (variety trial) generated fluorescence emission variability as function of the stress status. Chlorophyll fluorescence detection was conducted from the 1 nm FWHM radiance imagery at the crown level, targeting pure vegetation pixels to avoid background and shadow effects. Both spatial variability of fluorescence emission within the orchard as function irrigation supplies, as well as diurnal experiments demonstrated successful fluorescence retrieval capability and consistent estimates of fluorescence using the *in-filling* method applied to the airborne imagery.

Simulations with the FluorMOD model were used to assess fluorescence retrieval capability of both the *in-filling* method and published fluorescence-reflectance indices using a random set of synthetic spectra and variation of inputs including fluorescence efficiency, leaf chlorophyll content and canopy leaf area index. Canopy radiance, reflectance and derivative reflectance were used to assess the retrieval capability of fluorescence. The results of the simulation study proposed that fluorescence retrievals are best done using the *in-filling* method, the derivative index D702/D680 and reflectance indices R690/R630, R761-R757, and R761/R757. The above-mentioned indices were insensitive to LAI variation ( $r^2$  with LAI ranging from 0.03 to 0.08), with low Cab sensitivity for the fluorescence *in-filling* method, D702/D680, and R761-R757. On the other hand, other published indices generally accepted for fluorescence detection at leaf and canopy levels were demonstrated in this simulation study to exhibit high sensitivity with Cab and LAI. In particular, R740/R685, R740/R850, R685/R850, R740/R630 were highly affected by LAI ( $r^2$  ranging between 0.89 and 0.97) with little sensitivity to fluorescence. Indices D705/D722, D730/D706, DPi, R735/R850, R680/R630, R685/R630, and the curvature index  $R683^2/(R675 \cdot R691)$  were highly affected by Cab. The simulation study demonstrated the retrieval capability of the *in-filling* method even when other common effects such as chlorophyll content and leaf area index effects are considered. Moreover, other fluorescence-sensitive indices published in the literature are highly affected by chlorophyll and structural effects, and care must be taken when using indices in field conditions that are potentially affected by such undesired leaf and canopy effects.

The FluorMOD fluorescence model enabled the simulation of the fluorescence effects on canopy derivative reflectance, assessing previous results obtained experimentally in the laboratory or under natural light conditions.

Canopy derivative reflectance calculated from the synthetic spectra simulated without and with fluorescence effects demonstrated the red edge peak shift toward longer wavelengths due to the variation of the chlorophyll content and the *double-peak* feature observed on the derivative spectra when fluorescence effects are included. This result confirms laboratory experiments conducted in Zarco-Tejada *et al.* (2003) and later discussed in le Maire *et al.* (2004).

This manuscript validated fluorescence extraction from airborne imagery using the *in-filling* method with comparisons to field-measured steady-state fluorescence ( $F_s$ ) using the PAM-2100 instrument. In addition, to address potential structural effects on fluorescence retrievals from the airborne imagery, such as the influence of tree LAI, extracted crown NDVI was shown to have no relationship with crown fluorescence extracted from the imagery ( $r^2=0.05$ ), demonstrating the sensitivity of R757.5 and R760.5 nm bands to fluorescence and an absence of crown LAI influences. The consistency of airborne fluorescence retrievals from trees under water stress condition using the methods reported in the manuscript (higher  $F$  values on fully-irrigated compared to deficit watered trees) was assessed against crown temperature, another physiological indicator of water stress linked with fluorescence emission. Retrievals from the airborne imagery showed an inverse relationship between crown fluorescence and temperature, as expected in water-stressed trees (lower  $F$  and higher  $T$  in water stressed trees). Fluorescence emission retrievals were also related with assimilation measures conducted in the field at the time of the airborne acquisitions.

The manuscript demonstrates that fluorescence retrievals from vegetation canopies can be conducted operationally using multispectral cameras of 1 nm FWHM bands centered at 757.5 and 760.5 nm, supported by inferences from a simulation study with FluorMOD model. The validated methods enable the generation of fluorescence images at 15 cm resolution acquired at 150 m above the ground for vegetation stress detection. A similar demonstration of operational feasibility of fluorescence retrievals with a suitable imaging spectrometer using the specific reflectance indices identified in the simulation study with FluorMOD as reported here remains to be done in future research.

### **Acknowledgements**

Financial support from the Spanish Ministry of Science and Education (MEC) for the projects AGL2005-04049, EXPLORA-INGENIO AGL2006-26038-E/AGR, and CONSOLIDER CSD2006-67, is gratefully acknowledged, as well as the Junta de Andalucía - Excelencia AGR-595, and in-kind support provided by Bioiberica through the project PETRI PET2005-0616. Technical support from UAV Navigation and Tetracam Inc. for the accommodation of airborne requirements are also acknowledged. V. González Dugo, M. Morales, C. Ruz, D. Notario, M. Guillén, C. Trapero, A. Vera and M. Ruiz Bernier are acknowledged for scientific and technical support in field and airborne campaigns.

---

## References

- Abadía, J., Morales, F., Abadía, A. (1999). Photosystem II efficiency in low chlorophyll, iron-deficient leaves. *Plant Soil*, 215, 183-192.
- Agati G. (1998). Response of the in vivo chlorophyll fluorescence spectrum to environmental factors and laser excitation wavelength, *Pure and Applied Optics*, 7, 797-807.
2009. Berni, J.A.J., Zarco-Tejada, P.J., Suarez, L., Fereres, E., Thermal and Narrow-band Multispectral Remote Sensing for Vegetation Monitoring from an Unmanned Aerial Vehicle. *IEEE Transactions on Geoscience and Remote Sensing*, 47, (3), 722-738.
- Björkman, O., Powles, S.B. (1984). Inhibition of photosynthetic reactions under water stress: interaction with light level. *Planta*, 161, 490-504.
- Bradford, K.J., Hsiao, T.C. (1982). Physiological responses to moderate water stress. In: Encyclopedia of plant physiology, N.S., vol. 12B: Physiological plant ecology II: Water relations and carbon assimilation, pp. 263-324, Lange, O.L., Nobel, P.S., Osmond, C.B., Ziegler, H., eds. Springer, Berlin Heidelberg New York.
- Carter, G. A., Theisen, A. F. & Mitchell, R. J. (1990). Chlorophyll fluorescence measured using the Fraunhofer line-depth principle and relationship to photosynthetic rate in the field. *Plant, Cell and Environment*, 13, 79-83.
- Carter, G. A., Jones, J. H., Mitchell, R. J. & Brewer, C. H. (1996a). Detection of solar-excited chlorophyll a fluorescence and leaf photosynthetic capacity using a Fraunhofer line radiometer. *Remote Sensing of Environment*, 55, 89-92.
- Carter, G. A., Cibula, W. G., and Miller, R. L. (1996b). Narrow-band reflectance imagery compared with thermal imagery for early detection of plant stress. *Journal of Plant Physiology*, 148, 515-522.
- Carter, G. A., Freedman, A., Keabian, P. L., and Scott, H. E. (2004). Use of a prototype instrument to detect short-term changes in solar-excited leaf fluorescence. *International Journal of Remote Sensing*, 25, 1779-1784.
- Evain, S., Flexas, J. & Moya, I. (2004). A new instrument for passive remote sensing: 2. Measurement of leaf and canopy reflectance changes at 531 nm and their relationship with photosynthesis and chlorophyll fluorescence. *Remote Sensing of Environment*, 91, 175-185.
- Fereres, E., & Soriano, M. (2007). Deficit Irrigation For Reducing Agricultural Water Use. *J. Exp. Bot.*, 58, 147-159.
- Flexas, J., Escalona, J.M. & Medrano, H. (1999). Water stress induces different levels of photosynthesis and electron transport rate regulation in grapevines. *Plant Cell and Environment*, 22, 39-48.

Flexas, J., J.-M. Briantais, Cerovic, Z., Medrano, H., & Moya, I. (2000). Steady-State and maximum chlorophyll fluorescence responses to water stress in grapevine leaves: a new remote sensing system. *Remote Sensing of Environment*, 73, 282-297.

Flexas, J., Escalona, J.M., Evain, S., Gulias, J., Moya, I., Osmond, C.B. & Medrano, H. (2002). Steady-state chlorophyll fluorescence (Fs) measurements as a tool to follow variations of net CO<sub>2</sub> assimilation and stomatal conductance during water-stress in C-3 plants. *Physiologia Plantarum*, 114(2), 231-240.

Gao, B.C. (1996). NDWI-A normalized difference water index for remote sensing of vegetation liquid water from space. *Remote Sensing of Environment*, 58, 257-266.

Hsiao, T.C., Fereres, E., Acevedo, E., Henderson, D.W. Water stress and dynamics of growth and yield of crops. *Water and Plant life: Problems and modern approaches*, 1976, Springer.

Idso, S.B., Jackson, R.D. & Reginato, R.J. (1978). Extending the "degree day" concept of phenomenological development to include water stress effects. *Ecology*, 59, 431-433.

Idso, S.B., Jackson, R.D., Pinter, P.J., Reginato, R.J. & Hatfield, J.L. (1981). Normalizing the stress-degree-day parameter for environmental variability. *Agricultural and Forest Meteorology*, 24, 45-55.

Jackson R.D., Idso, S.B., Reginato R.J. & Ehrier, W.L. (1977). Crop temperature reveals stress. *Crop soils*, 29, 10-13.

Jackson, R.D. & Pinter Jr., P.J. (1981). Detection of water stress in wheat by measurement of reflected solar and emitted thermal IR radiation. In: *Spectral Signatures of Objects in Remote Sensing*, Institut National de la Recherche Agronomique, Versailles, France, pp. 399-406.

Jackson, R. D., Idso S. B., Reginato R. J. & Pinter, P. J. (1981). Canopy Temperature As Crop Water-Stress Indicator. *Water Resources Research*, 17, 1133-1138.

Krause, G. H. & Weis, E. (1984). Chlorophyll fluorescence as a tool in plant physiology. II. Interpretation of fluorescence signals. *Photosynthesis Res.*, 5, 139-157.

Larcher, W. (1994). Photosynthesis as a tool for indicating temperature stress events, In *Ecophysiology of photosynthesis*, (Schulze, E. D. and Caldwell, M. M., Ed.), Springer, Berlin, pp. 261-277.

Le Maire, G., François, C. & Dufrêne, E. (2004). Towards universal broad leaf chlorophyll indices using PROSPECT simulated database and hyperspectral reflectance measurements. *Remote Sensing of Environment*, 89, 1-28.

Lichtenthaler, H. K. & Rinderle, U. (1988). The role of chlorophyll fluorescence in the detection of stress conditions in plants. *CRC Crit. Rev. Anal. Chem.*, 19 (Suppl. 1), 529-585.

Lichtenthaler, H. K. (1992). The Kautsky effect: 60 years of chlorophyll fluorescence induction kinetics. *Photosynthetica*, 27, 45-55.

Liu, L., Zhang, Y., Wang, J., Zhao, C. (2005). Detecting Solar-Induced Chlorophyll Fluorescence From Field Radiance Spectra Based on the Fraunhofer Line Principle. *IEEE Transactions on Geoscience and Remote Sensing*, 43, 827-832.

Maier S.W. (2000), Modeling the Radiative Transfer in Leaves in the 300 nm to 2.5  $\mu\text{m}$  Wavelength Region taking into Consideration Chlorophyll Fluorescence - The Leaf Model SLOPE. PhD Thesis - Technische Universität München (München), 124 pp.

Maier S.W., Lüdeker W., Günther K.P. (1999). SLOP: A revised version of the stochastic model for leaf optical properties. *Remote Sensing of the Environment*, 68(3), 273-280.

Maier, S.W., Günther, K.P. & Stellmes, M., (2002). Remote Sensing and Modelling of Solar Induced Fluorescence, 1st Workshop on Remote Sensing of Solar Induced Vegetation Fluorescence, Noordwijk, Netherlands.

McFarlane, J. C., Watson, R. D., Theisen, A. F., Jackson, R. D., Ehrler, W. L., Pinter Jr., P. J., Idso, S. B. & Reginato, R. J. (1980). Plant stress detection by remote measurement of fluorescence. *Applied Optics*, 19, 3287-3289.

Meroni, M., Picchi, V., Rossini, M., Cogliati, S., Panigada, C., Nali, C., Lorenzini, G., & Colombo, R. (2008a), Leaf level early assessment of ozone injuries by passive fluorescence and PRI. *International Journal of Remote Sensing*, 29:17, 5409- 5422.

Meroni, M., Rossini, M., Picchi, V., Panigada, C., Cogliati, S., Nali, C., & Colombo, R. (2008b). Assessing steady-state fluorescence and PRI from hyperspectral proximal sensing as early indicators of plant stress: the case of ozone exposure. *Sensors*, 8, 1740-1754.

Miller, J.R., Berger, M., Alonso, L., Cerovic, Z., Goulas, Y., Jacquemoud, S., Louis, J., Mohammed, G., Moya, I., Pedros, R., Moreno, J.F., Verhoef, W., Zarco-Tejada, P.J. (2004), Progress on the development of an integrated canopy fluorescence model, 2003 - *International Geoscience and Remote Sensing Symposium, IGARSS'03*, pp. 601-603 Vol.1, ISBN 0-7803-7929-2 - 0-7803-7930-6, Toulouse (France), 21-25 / 7 /2004.

Morales, F., Abadía, A., Abadía, J. (1991), Chlorophyll fluorescence and photon yield of oxygen evolution in iron-deficient sugar beet (*Beta vulgaris* L.). *Plant Physiology*, 97, 886-893.

Morales, F., Abadía, A., Abadía, J. (1998). Photosynthesis quenching of chlorophyll fluorescence and thermal energy dissipation in iron-deficient sugar beet leaves. *Australian Journal of Plant Physiology*, 25, 403-412.

Morales, F., Abadía, A., Abadía, J. (2006), Photoinhibition and photoprotection under nutrient deficiencies, drought and salinity. In *Photoprotection, Photoinhibition, Gene Regulation, and Environment*. Eds. B.

Demmig-Adams, W.W. Adams III & A.K. Mattoo. Springer, The Netherlands, pp. 65-85.

Morales, F., Belkhodja, R., Abadía, A., Abadía, J. (2000), Photosystem II efficiency and mechanism of energy dissipation in iron-deficient, field grown pear trees (*Pyrus communis* L.). *Photosynthesis Research*, 63, 9-21.

Moya, I., Camenen, L., Evain, S., Goulas, Y., Cerovic, Z.G., Latouche, G., Flexas, J., Ounis, A. (2004), A new instrument for passive remote sensing 1. Measurements of sunlight-induced chlorophyll fluorescence. *Remote Sensing of Environment*, 91, 186-197.

Papageorgiou, G. (1975). Chlorophyll fluorescence: An intrinsic probe of photosynthesis, In *Bioenergetics of Photosynthesis*, (Govindjee, Ed.), Academic Press, New York, pp. 319-371.

Pedrós, R., Jacquemoud S., Goulas Y., Louis J., Moya, I. (2004). A new leaf fluorescence model, *2nd International Workshop on Remote Sensing of Vegetation Fluorescence*, 17-19 Nov. Montreal, Canada.

Pedrós R, Moya I, Goulas Y, Jacquemoud S. (2008), Chlorophyll fluorescence emission spectrum inside a leaf, *Photochem Photobiol Sci.*, 7(4):498-502.

Peguero-Pina, J.J., Morales, F., Flexas, J., Gil-Pelegrín, E. & Moya, I. (2008). Photochemistry, remotely sensed physiological reflectance index and depoxidation state of the xanthophyll cycle in *Quercus coccifera* under intense drought. *Oecologia* 156(1), 1-11.

Peñuelas, J., Filella, I., Biel, C., Serrano, L., & Save, R. (1993). The reflectance at the 950– 970 nm region as an indicator of plant water status. *International Journal of Remote Sensing*, 14, 1887–1905.

Peñuelas, J., Llusia, J., Piñol, J. & Filella, I. (1997). Photochemical reflectance index and leaf photosynthetic radiation-use-efficiency assessment in Mediterranean trees. *International Journal of Remote Sensing*, 18, 2863-2868.

Pérez-Priego, O., Zarco-Tejada, P.J., Sepulcre-Cantó, G, Miller, J.R., & Fereres, E. (2005). Detection of Water Stress in Orchard Trees with a High-Resolution Spectrometer through Chlorophyll Fluorescence *in-filling* of the O<sub>2</sub>-A band, *IEEE Transactions on Geoscience and Remote Sensing*, 43, 2860-2869.

Rock, B. N., Vogelmann, J. E., Williams, D.L., Vogelmann, A. F. & Hoshizaki, T. (1986). Remote detection of forest damage. *Biosciencie*, 36, 439-455.

Schreiber, U. & Bilger, W. (1987). Rapid assessment of stress effects on plant leaves by chlorophyll fluorescence measurements, In *Plant response to stress*, (Tenhunen, J. D. and Catarino, E. M., Ed.), Springer-Verlag, Berlin, Germany, pp. 27-53

Schreiber, U., Bilger, W. & Neubauer, C. (1994), Chlorophyll fluorescence as a non-destructive indicator for rapid assessment of in vivo photosynthesis. *Ecol. Stud.* , 49-70.

Smith, G. M. & Milton, E. J. (1999). The Use of the Empirical Line Method to calibrate Remotely Sensed Data To Reflectance. *International Journal of Remote Sensing*, 20, 2653-2662.

Sepulcre-Cantó, G., Zarco-Tejada, P.J., Jiménez-Muñoz, J.C., Sobrino, J.A., de Miguel, E., & Villalobos, F.J., (2006). Within-field thermal variability detection as function of water stress in *Olea europaea* L. orchards with high spatial remote sensing imagery. *Agricultural and Forest Meteorology*, 136, 31-44.

Sepulcre-Cantó, G., Zarco-Tejada, P.J., Jiménez-Muñoz, J.C., Sobrino, J.A., Soriano, M.A., Fereres, E., Vega V., and Pastor, M. (2007). Monitoring yield and fruit quality parameters in open-canopy tree crops under water stress. Implications for ASTER. *Remote Sensing of Environment*, 107, 455-470.

Slatyer, J. O. (1967). *Plant-Water Relationships*. New York and London: Academic press. 366p.

Soukupová, J., Cséfalvay, L., Urban, O., Kosvancová, M., Marek, M., Rascher, U., Nebdal, L. (2008). Annual variation of the steady-state chlorophyll fluorescence emission of evergreen plants in temperate zone. *Functional Plant Biology*, 35, 63-76.

Suarez, L., Zarco-Tejada, P.J., Sepulcre-Cantó, G., Pérez-Priego, O., Miller, J.R., Jiménez Muñoz, J.C. y Sobrino, J. (2008) Assessing Canopy PRI for Water Stress detection with Diurnal Airborne Imagery. *Remote Sensing of Environment*, 112, 560-575.

Suarez, L., Zarco-Tejada, P.J., Berni, J.A.J., González-Dugo, V., Fereres, E. (2009), Modelling PRI for Water Stress Detection using Radiative Transfer Models, *Remote Sensing of Environment*, 113, 730-744.

Thenot, F., Méthy, M. & Winkel, T. (2002). The Photochemical Reflectance Index (PRI) as a water-stress index. *International Journal of Remote Sensing*, 23(23), 5135-5139.

Verhoef, W. (2005), Extension of SAIL to model solar-induced canopy fluorescence spectra, *2nd International Workshop on Remote Sensing of Vegetation Fluorescence*, 17-19 Nov. 2004, Montreal, Canada.

Wolfe, D.W., Fereres, E., Voss, R.E. (1983). Growth and yield response of two potato cultivars to various levels of water applied. *Irrigation Science*, 3, 211-222.

Zarco-Tejada, P.J., Miller, J.R., Mohammed, G.H., Noland, T.L. (2000a). Chlorophyll Fluorescence effects on vegetation apparent reflectance: I. Leaf-level measurements and simulation of reflectance and transmittance spectra. *Remote Sensing Environment*, 74(3), 582-595.

Zarco-Tejada, P.J., Miller, J.R., Mohammed, G.H., Noland, T.L., Sampson, P.H. (2000b), Chlorophyll Fluorescence effects on vegetation apparent reflectance: II. Laboratory and hyperspectral airborne experiments. *Remote Sensing of Environment*, 74(3), 596-608.

Zarco-Tejada, P.J., Pushnik, J., Dobrowski, S., Ustin, S.L. (2003). Steady-state chlorophyll a Fluorescence detection from canopy derivative reflectance

and Double-Peak Red-Edge effects. *Remote Sensing of Environment*, 84(2), 283-294.

Zarco-Tejada, P.J., Miller, J.R., Haboudane, D., Tremblay, N., Apostol, S. (2004). Detection of chlorophyll fluorescence in vegetation from airborne hyperspectral CASI imagery in the red edge spectral region. 2003 - *International Geoscience and Remote Sensing Symposium, IGARSS'03*, pp. 598- 600 Vol.1, ISBN 0-7803-7929-2 - 0-7803-7930-6, Toulouse (France), 21-25/7/2004

Zarco-Tejada, P.J., Miller, J.R., Pedrós, R., Verhoef, W. , Berger, M. (2006) FluorMODgui V3.0 - A Graphic User Interface for the Leaf and Canopy Simulation of Chlorophyll Fluorescence, *Computers & Geosciences*, 32, 577-591.

## Capítulo 3

### **Mapping canopy conductance and CWSI in olive orchards using high resolution thermal remote sensing imagery.**

**Autores:** Berni, J.A.J.<sup>a</sup>, Zarco-Tejada, P.J.<sup>a</sup>, Sepulcre-Cantó, G.<sup>a</sup>, Fereres, E.<sup>a,b</sup>, Villalobos, F.J.<sup>a,b</sup>

<sup>a</sup> *Instituto de Agricultura Sostenible (IAS), Consejo Superior de Investigaciones Científicas (CSIC), Córdoba, Spain*

<sup>b</sup> *Departamento de Agronomía, Universidad de Córdoba (UCO), Córdoba, Spain*

**Publicado en:** *Remote Sensing of Environment*, 113, 2380-2388.

*Las ideas no duran mucho. Hay que hacer algo con ellas.*

Santiago Ramón y Cajal (1852-1934).

## **Resumen**

La caracterización de propiedades biofísicas relacionadas con el agua en vegetación heterogénea está limitada por la falta de resolución espacial de las imágenes de satélite y por las limitaciones físicas de las observaciones puntuales en tierra. En este trabajo se han aplicado modelos basados en la temperatura de la cubierta estimada a partir de imágenes térmicas de alta resolución para calcular la conductancia de la cubierta ( $G_c$ ) y un índice de detección de estrés llamado *Crop Water Stress Index* (CWSI) en olivar. El modelo de  $G_c$  requiere la simulación de la radiación neta ( $R_n$ ) y la resistencia aerodinámica ( $r_a$ ) en función de la velocidad del viento y la estructura de la cubierta. En ambos casos, los modelos de  $R_n$  y  $r_a$  han sido validados frente a medidas y datos publicados de olivar. Los valores modelizados de  $G_c$  en árboles con diferente estado hídrico se han relacionado bien con las estimaciones de  $G_c$  obtenidas a partir de medidas de conductancia estomática en los mismos árboles. El modelo usado para el cálculo de CWSI ha tenido en cuenta no sólo el déficit de presión de vapor, sino también la radiación neta y la velocidad del viento, parámetros que se sabe que afectan a la diferencia de temperatura entre la cubierta y el aire. Los valores calculados de CWSI para árboles bien regados y con déficit hídrico se han relacionado bien con medidas de potencial hídrico medido en los mismos árboles. La metodología aplicada en este manuscrito ha sido usada para validar la estimación teórica de líneas base necesarias para el cálculo del CWSI, comparándose posteriormente con las estimadas empíricamente. Las imágenes térmicas de alta resolución espacial obtenidas durante dos años con el sensor *Airborne Hyperspectral Scanner* (AHS) y desde un vehículo aéreo no tripulado (UAV) han sido usadas para mapear  $G_c$  y el CWSI de un olivar con distintos tratamientos de riego. La metodología desarrollada permite el análisis espacial del uso del agua en cubiertas heterogéneas y la caracterización espacial del estrés hídrico, lo que permitiría potenciales aplicaciones para la mejora del manejo del riego usando imágenes térmicas de alta resolución.

**Palabras Clave:** conductancia estomática, CWSI, estrés hídrico, aerotransportado, UAV, vehículo aéreo no tripulado.

**Abstract**

The characterization of field properties related to water in heterogeneous open canopies is limited by the lack of spatial resolution of satellite-based imagery and by the physical constraints of point observations on the ground. We apply here models based on canopy temperature estimated from high resolution airborne imagery to calculate tree canopy conductance ( $G_c$ ) and the crop water stress index (CWSI) of heterogeneous olive orchards. The  $G_c$  model requires the simulation of net radiation ( $R_n$ ) and the aerodynamic resistance ( $r_a$ ) as a function of windspeed and canopy structure. In both cases, the  $R_n$  and  $r_a$  models were tested against measurements and published data for olive orchards. Modeled values of  $G_c$  of trees varying in water status correlated well with  $G_c$  estimates obtained from stomatal conductance measurements in the same trees. The model used to calculate the *Crop Water Stress Index* (CWSI) took into account, not only the vapor pressure deficit but the  $R_n$  and the windspeed as well, parameters known to affect the temperature differences between the air and the tree canopy. The calculated CWSI for water deficit and well irrigated olive trees correlated with the water potential measured on the same trees. The methodology applied in this manuscript was used to validate the estimation of theoretical baselines needed for the CWSI calculations, comparing against traditional empirical baseline determination. High resolution thermal imagery obtained with the *Airborne Hyperspectral Scanner* (AHS), and from an Unmanned Aerial Vehicle (UAV) for two years was used to map  $G_c$  and CWSI of an olive orchard where different irrigation treatments were applied. The methodology developed here enables the spatial analysis of water use within heterogeneous orchards, and the field characterization of water stress, leading to potential applications in the improvement of orchard irrigation management using high resolution thermal remote sensing imagery.

**Keywords:** stomatal conductance, CWSI, water stress, airborne, UAV.

## **1. Introduction**

The established method for detecting water stress of crops in the field uses a pressure chamber to measure the xylem water potential of individual leaves in selected plants (Hsiao, 1990; Shackel et al., 1997). Another water stress indicator is based on measuring stomatal conductance with leaf diffusion porometers. Both methods provide point observations which are not free of measuring errors (Hsiao, 1990) and are very time consuming, limiting the number of individuals that can be monitored to accurately characterize a field. Water stress induced stomatal closure reduces transpiration rate, thus reducing evaporative cooling and increasing leaf temperature that could be tracked by thermal infrared thermometers and imagers. This approach at detecting water stress became very popular in the 1970's and 80's with the advent of hand-held thermometers (Tanner, 1963; Fuchs & Tanner, 1966; Idso et al., 1978; Idso et al., 1981; Jackson et al., 1977a; Jackson et al., 1977b; Jackson et al., 1981; Jackson, 1982) and led to the development of a normalized index to overcome the effects of other environmental parameters affecting the relation between stress and plant temperature. The index was termed the *Crop Water Stress Index* (CWSI) (Idso et al., 1981; Jackson et al., 1981), and consisted in relating the actual difference between canopy and air temperatures ( $T_c$  and  $T_a$ , respectively) to the difference between the  $T_c-T_a$  values of a non-water stressed baseline (NWSB), and an upper  $T_c-T_a$  limit, both being a function of the atmospheric vapor pressure deficit (VPD) (Idso et al., 1981). A CWSI ranging from 0 to 1 is thus obtained which was found to be proportional to the stress level in many crops, provided that NWSB values are known for the crop and local conditions. Many NWSB equations were published in the past for different crops (Idso, 1982; Nakayama & Bucks, 1983; Glenn et al., 1989; Wanjura et al., 1990; Sepaskhah & Kashefipour, 1994; Yazar et al., 1999; Testi et al., 2008). A major reason for the interest in the CWSI was the possibility of measuring it remotely, thus avoiding time consuming techniques used for detecting stress at the field or farm levels.

However, the use of CWSI as a stress indicator has not been widely adopted for two main reasons (Cohen et al., 2005): (i) temperature remotely sensed from readily available satellite platforms or airborne sensors lacks the necessary spatial resolution for the accurate separation of canopy temperature from the sunlit and shaded soil background; (ii) the different equations of NWSB published are site dependent, since the VPD normalization procedure used for obtaining the CWSI does not account for differences in net radiation and aerodynamic resistance which are known to affect the index (Hipps et al., 1985; Jackson et al., 1988; Jones, 1999). Avoiding the first issue is not easy, since currently available satellite thermal imagery is limited to Landsat TM and ASTER scanners, yielding 120 m and 90 m, respectively, and MODIS or AVHRR, with 1 km pixel size. The medium-low spatial resolution of such

satellite thermal scanners makes mapping water stress only potentially suitable for regional scales if successfully accounting for canopy heterogeneity (Moran et al., 1994; Norman et al., 1995). Alternatively, airborne thermal imagery has been proved suitable for mapping water stress on discontinuous canopies (Sepulcre-Cantó et al., 2006; Sepulcre-Cantó et al., 2007), provided that the spatial resolution allows the detection of isolated tree crowns (<2 m pixel size). However, the cost and operational complexity of airborne platforms make its extensive use in agriculture very limited (Berni et al., 2009). New thermal imaging sensors onboard unmanned aerial platforms provide sub-meter spatial resolution (Herwitz et al., 2004; Sugiura, 2005; Berni et al., 2009) enabling the retrieval of pure canopy temperature, thus minimizing soil thermal effects. High resolution thermal imagery would make possible the retrieval of energy fluxes from pure vegetation on open canopies, such as tree orchards, where most remote sensing based methodologies do not perform well. Nevertheless, atmospheric effects and atmospheric transmittance should be considered even for low altitude platforms aimed at keeping temperature measurement errors below 1K (Berni et al., 2009).

If high-resolution canopy temperature can be accurately monitored then the extensive use of CWSI may be a practical option. New theoretical and practical approaches have been proposed to overcome the need for the empirical retrieval of the NWSB needed in the CWSI calculation. The use of theoretical equations of CWSI based on the energy balance equation (Jackson et al., 1988) is limited by the need to estimate net radiation and aerodynamic resistance, but it allows the calculation of canopy conductance (Smith, 1988; Leinonen et al., 2006; Lhomme & Monteny, 2000). Most recent works overcome this problem by using dry and wet references that account for the CWSI upper and lower limits, respectively, allowing the estimation of CWSI with a minimum of meteorological measurements (Jones et al., 2002; Cohen et al., 2005; Grant et al., 2007; Möller et al., 2007). However the use of such reference surfaces is a clear limitation for the practical and extensive use of this methodology.

This manuscript validates a methodology to map the spatial distribution of CWSI and the canopy conductance of a field from very high spatial resolution thermal imagery and in situ atmospheric variables. This approach is particularly suitable for monitoring areas of medium size (in the order of hundred of hectares) using unmanned aircrafts that could provide frequent visits and short turnaround times to detect water stress for irrigation scheduling. The methodology presented here does not require the use of reference surfaces and relies on physical models to estimate all input variables of the energy balance equations.

## **2. Model Approach for estimating Canopy Conductance**

The model departs from the assumption that pure vegetation surface temperature can be retrieved from thermal imagery if the spatial resolution enables to discriminate pure crown pixels from sunlit and shadowed soil pixels. Furthermore, at-sensor radiometric temperature is converted to surface temperature by means of atmospheric and emissivity corrections.

Assuming that the energy stored in the foliage and the energy used in the photosynthetic processes are negligible, the energy balance in the canopy foliage is written as:

$$R_n^c = H_c + \lambda E_c \quad [3.1]$$

where  $R_n$  is the net radiation,  $H_c$  the sensible heat flux into the air, and  $\lambda E$  is the latent heat flux. The subscript c denotes that only the canopy energy fluxes are considered.

The terms  $H_c$  and  $\lambda E_c$  can be expressed as:

$$H_c = \rho C_p \cdot \frac{(T_c - T_a)}{r_a} \quad [3.2]$$

$$\lambda E_c = \frac{\rho \cdot C_p \cdot (e_c^* - e_a)}{\gamma \cdot (r_a + r_c)} \quad [3.3]$$

where  $\rho$  is the air density;  $C_p$  the specific heat of air;  $T_c$  and  $T_a$  are respectively the temperature of the canopy and air; and  $r_a$  is the aerodynamic resistance;  $\gamma$  is the saturated vapor pressure at the canopy temperature;  $e_a$  is the actual vapor pressure of air;  $\gamma$  the psychrometric constant; and  $r_c$  is the canopy resistance to vapor transport.

Combining Equations (3.1)-(3.3),  $r_c$  is calculated as:

$$r_c = \frac{r_a (e_c^* - e_a)}{\gamma \left( \frac{r_a R_n}{\rho C_p} - (T_c - T_a) \right)} - r_a \quad [3.4]$$

To solve this equation,  $T_a$  and  $e_a$  can be retrieved from a weather station whereas  $\rho C_p$  and  $\gamma$  are calculated from  $T_a$  and atmospheric pressure.  $T_c$  can be measured by means of thermal infrared sensors, or in a larger scale it is obtained from thermal imagery. Although net radiation can be measured locally using a net radiometer, this instrument is not generally available and a parameterization is needed to estimate net radiation from local weather

variables, as presented below. Also, aerodynamic resistance depends mainly on wind speed and canopy structure, but it is also affected by buoyancy effects when  $T_c > T_a$  and needs to be modeled based on weather parameters. The accuracy of the estimated canopy conductance is function of the input parameters used, with some authors providing sensitivity analyses for these parameters. They remark the importance of the errors in net radiation, temperature and vapor pressure deficit (Leinonen et al., 2006) but also the importance of aerodynamic resistance in water stressed crops (Rana & Kterji, 1998).

### 2.1. Net Radiation Modeling

The radiation balance over the foliage can be described as:

$$R_n = (1 - \alpha_c) \cdot R_s^\downarrow - \varepsilon_c \cdot \sigma \cdot T_c^4 + \varepsilon_c \cdot R_L^\downarrow \quad [3.5]$$

where  $R_n$  is the net radiation,  $\alpha_c$  is the total shortwave surface albedo;  $R_s^\downarrow$  is the solar shortwave irradiance;  $\varepsilon_c$  is the surface broadband emissivity;  $\sigma$  is the Stefan-Boltzmann constant; and  $R_L^\downarrow$  is the longwave incoming irradiance from the atmosphere. In this equation  $R_s$  can be measured by means of a pyranometer, available in most of the agro meteorological weather stations, the broadband emissivity for pure vegetation can be assumed as 0.98 (Monteith & Unsworth, 2008). However, special attention must be paid to surface albedo and incoming longwave radiation.

Downwelling longwave radiation can be measured with longwave radiometers (pyrgeometers), which are rare in weather stations. An alternative is the use of radiative transfer models such as MODTRAN (Berk et al., 1999) but a good knowledge of the atmospheric profile is required. Several methods have been developed during the past century in order to estimate from surface weather variables with reasonable results (for a review see Crawford & Duchon, 1999). These techniques are based on the Stefan Boltzmann law, using the effective emissivity and temperature of the overlying atmosphere according to:

$$R_L^\downarrow = \varepsilon_{atm} \cdot \sigma \cdot T_{atm}^4 \quad [3.6]$$

Given the difficulty to estimate  $\varepsilon_{atm}$  and  $T_{atm}$ , the developed methods parameterize from the measured air temperature and vapor pressure at surface level. Several authors have published relationships of sky emissivity for clear days ( $\varepsilon_{clear}$ ) as a function of  $T_a$  and/or vapor content (see review by Kjaersgaard et al., 2007). Most of these models have been developed with specific datasets

from a region which limits its general use. An additional problem occurs when non clear-sky conditions are present, since the presence of clouds and aerosols increases. A solution proposed by Crawford & Duchon (1999) is the use of the cloud fraction term (*clf*) to correct the emissivity on clear conditions, defining *clf* as

$$clf = 1 - s \quad [3.7]$$

where *s* is the fraction of the measured shortwave irradiance over the potential clear sky irradiance, which can be estimated by radiative transfer models like MODTRAN (Berk et al., 1999) used in this study.

$$R_L^\downarrow = [clf + (1 - clf) \cdot \varepsilon_{clear}] \cdot \sigma \cdot T_{am}^4 \quad [3.8]$$

The emissivity for clear days has been calculated using the model proposed by Brusaert (1975) and adapted by Crawford (1999).

Surface albedo can be measured directly by albedometers over the surface of interest, which is not operational for larger-scale applications. Since broadband albedo can be defined as the integration of the reflectance for all the wavelengths of the shortwave spectrum, some authors proposed the use of discrete bands from multispectral imaging sensors (Brest & Goward, 1987; Liang, 2001) using weighting coefficients for each specific band. Broadband albedo depends not only on the surface characteristics but also on atmospheric conditions such as turbidity and cloudiness, and the solar zenith angle. For clear days, the main driver for albedo is the solar zenith angle (Liang, 2001). Therefore if albedometer measurements are available for a number of clear sky days, the albedo can be determined as a function of the solar zenith angle.

## **2.2. Aerodynamic Resistance Modeling**

Aerodynamic resistance becomes a very important parameter in the energy balance equations when estimating sensible heat flux and latent heat flux using remote sensing measurements. Many authors have published different parameterizations to model aerodynamic resistance with different levels of simplification and empiricism (see review in Liu et al., 2007).

In this study, the model of Viney (1991) has been used given the simplicity of that parameterization and good results according to Liu et al. (2007). That model is valid for stable and non-stable conditions, which are very common in olive tree orchards in summer, where the canopy temperature can be several degrees above the air temperature.

The zero plane displacement (*d*) and the roughness lengths (*z<sub>0</sub>*), which depend on canopy dimensions and architecture, can be estimated using wind

profiles and momentum flux measurements. However very simple empirical functions of canopy height ( $h$ ) have been proposed, such as  $d=0.66h$  and  $z_0=0.13h$  (Brutsaert, 1982; Monteith & Unsworth, 2008). Nevertheless, these values were proposed for uniform cropping surfaces or dense forests with a closed canopy, and may not apply to sparse and heterogeneous canopies. Verhoef (1997) demonstrated that Raupach's analytical treatment of drag and drag partition on rough surfaces using dimensional analysis performed well even on sparse canopies, and that values of  $d/h$  and  $z_0/h$  could be obtained as a function of the frontal area index and the canopy structure. We have applied Raupach's methodology to the study site and the following relationships were obtained:  $d=0.732h$  and  $z_0=0.113h$ . These values are close to the values given by Monteith and Unsworth (2008) and Brutsaert (1982), and are also in accordance with those obtained by Villalobos (2000) for an olive orchard.

### 2.3. Modelling CWSI

An analytical solution for the CWSI may be obtained once that  $r_c$  and the potential canopy resistance for a non water stressed crop ( $r_{cp}$ ) are known (Jackson et al., 1981):

$$CWSI = 1 - \frac{E}{E_p} = \frac{\gamma(1 + r_c / r_a) - \gamma^*}{\Delta + \gamma(1 + r_c / r_a)} \quad [3.9]$$

where  $\Delta$  is the slope of the saturation vapor pressure temperature relationship and,

$$\gamma^* = \gamma(1 + r_{cp} / r_a) \quad [3.10]$$

Since  $r_c$  can be calculated from Equation 4 using the methodology described above, a CWSI map could be generated from high spatial resolution thermal imagery. The method would require in-situ meteorological measurements and physical models used to estimate  $R_n$  and  $r_a$ . As the spatial resolution used in this study (40 cm pixel size) enables isolating the tree crown temperature from the soil background, there is no need for using vegetation indices to estimate the fraction vegetation cover as required in ET models (see Moran et al., 1994). Additionally, the proposed methodology based on physical models does not require the need for a reference surface, as proposed on recent studies for CWSI estimation (Jones et al., 2002; Cohen et al., 2005; Grant et al., 2007; Möller et al., 2007).

Estimates of  $r_{cp}$  have been published for many crops, also for the case of olive trees (Moriana et al., 2002; Testi et al., 2006), Additionally, theoretical

models of canopy resistance may be used to estimate this parameter, e.g. Jarvis (1976).

### **3. Materials and Methods**

#### **3.1. Field data collection**

The study site was located in southern Spain, consisting on a 4 ha olive orchard (*Olea europaea* L cv. 'Arbequino') planted at 7.0 × 3.5 m, with rows oriented in the NS direction, an average crown height of 5m and a leaf area index (LAI) of 1.4 when the measurements were performed. Therefore, the LAI within the area covered by the tree crowns would be over 3.0, a value found in most annual crops to ensure almost full radiation interception by the canopy (Ritchie, 1972).

The climate of the area is Mediterranean with an average annual rainfall of 650 mm, concentrated from autumn to spring, and a reference evapotranspiration of 1390 mm. This olive orchard has been the site for previous ET and irrigation-related studies (Iniesta et al., 2009; Testi et al., 2004; Moriana & Fereres, 2002). The experiment monitored had three different drip-irrigation treatments within an area of 6 rows of 18 olive trees each (2646 m<sup>2</sup>). The treatments were: i) a control (FI) that applied 2.8 mm/day equivalent to full ET; ii) a sustained deficit irrigation (SDI) that applied 0.7 mm/day or 25% of FI; and iii) a regulated deficit irrigation (RDI) treatment which applied, 1.2 mm/day from 14 June to 5 July and from 6 September to 19 October, and no irrigation from 5 July to 6 September (see Iniesta et al., 2009).

Ten infrared temperature (IRT) sensors (model IRTS-P, Apogee, Logan, UT, USA) were placed 1 m above the trees from the three irrigation treatments (Sepulcre-Cantó et al., 2006), recording the mean temperature at 5-minute intervals in 3 dataloggers (model CR10X, Campbell Sci., Logan, UT, USA). Two additional sensors were placed over bare soil, recording temperature at the same time intervals over sunny and shaded soil. Air temperature and humidity were measured above the canopy with an air temperature and humidity probe (model HMP45C, Vaisala, Helsinki, Finland) placed 1 m above the canopy (approx. 6 m above the ground).

A high precision albedometer (model CM7B, Kipp & Zonen, Delft, NL) and a net pyrgometer (model CG2, Kipp & Zonen, Delft, NL) were installed 1 m above one tree to measure continuously downward and upward shortwave and longwave radiation fluxes to calculate surface albedo. Weather data were retrieved from an automated weather station located on an irrigated grass (*Festuca arundinacea* L.) plot of 1.5 ha, situated 500 m east of the olive orchard.

Data was recorded on a 10 minute basis, including wind speed and direction at 2 m height, air temperature and humidity at 1.5 m, and solar radiation.

Leaf stomatal conductance was measured weekly around 10:30 GMT during the summer of 2005, and on 23 August, 2007 at 13:30 GMT with a steady-state porometer (model PMR-4, PP Systems, Hitchin Herts, Great Britain). On every one of the 10 monitored trees, 5 well illuminated and fully expanded, middle aged leaves were selected and identified in order to do the measurements on the same leaves during 2005, while different leaves were selected in 2007. It is well known that scaling up leaf measurements of stomatal conductance to canopy conductance is not straightforward (Baldochi et al., 1991; Lhomme, 1991; Furon et al., 2007). Here, we assumed that the measured canopy resistance was represented by the resistance of the population of sunlit leaves with their measured resistances in parallel. For this reason only sunlit leaves were measured with the porometer, and the average leaf resistance measurements were compared against the estimates of canopy conductance calculated with the model (Eq. 3.4).

Leaf water potential was measured on the monitored trees with a pressure chamber (PWSC Model 3000, Soilmoisture equipment Corp., California, USA) on 26 August, 2007 at 13:30 GMT, following the procedure described in Sepulcre-Cantó (2006).

### 3.2. Airborne Campaigns

An airborne campaign was conducted by the Spanish Aerospace Institute (INTA) with the Airborne Hyperspectral Scanner (AHS). The AHS sensor was flown over the olive orchard at 3 different times (7:30 GMT, 9:30 GMT, 12:30 GMT) on 16 July 2005 at 1000 m altitude above ground level (AGL), obtaining 6000×2000 m<sup>2</sup> images at 2 m spatial resolution (Figure 1a). The AHS sensor has 80 spectral bands in the 0.43 - 12.5  $\mu\text{m}$  spectral range. The 80 bands are distributed in 4 spectral regions (VIS/NIR, SWIR, MWIR and TIR) with a field of view (FOV) of 90° and a 2.5 mrad instantaneous field of view (IFOV). A full description of the AHS bands, calibration methods, and the radiometric and atmospheric correction procedures can be found in Sobrino et al., (2006).

Another set of images were collected from an unmanned aerial vehicle (UAV) platform which was developed to carry a payload with thermal and multispectral imaging sensors for remote sensing operation (Berni et al., 2009). The study site was scanned with the UAV carrying a thermal camera on 23 August 2007 at an altitude of 150 m AGL (Figure 3.1b). The thermal imager used was the Thermovision A40M (FLIR, USA). The image sensor is a Focal Plane Array (FPA) based on uncooled microbolometers with a resolution of

320x240 pixels, 38 x 38  $\mu\text{m}$  pixel size and spectral response in the range of 7.5 – 13  $\mu\text{m}$ , yielding a sensitivity of 0.08 K at 303 K. The camera was equipped with a 40° FOV lens, which delivered 40 cm spatial resolution imagery at the flight altitude, enabling the retrieval of pure crown temperature from each tree under study (Figure 3.1c).

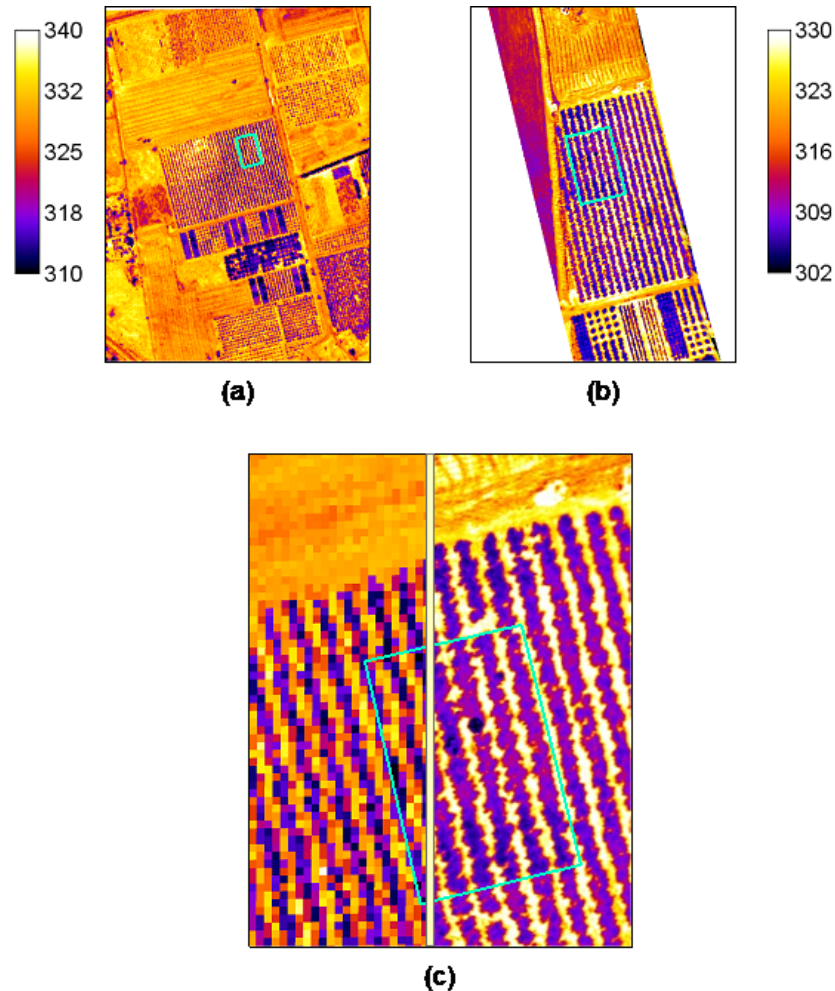


**Figure 3.1.** Airborne thermal imagery acquired over the study site: a) AHS image collected at 12:30GMT on 16 July 2005; b) UAV image collected at 13:30 GMT on 23 August 2007; c) image detail showing the spatial resolution differences of AHS (2m) against the UAV (40cm). The spatial resolution of the UAV imagery shows individual tree crown, enabling pure crown temperature extraction.

Airborne AHS and UAV thermal imagery were processed applying geometric, radiometric and atmospheric corrections. AHS image atmospheric correction was conducted using the MODTRAN-4 radiative transfer code (Berk et al., 1999). In situ atmospheric profiles were conducted at 7:00 and 12:00 GMT on 16 July 2005 for AHS atmospheric correction. Land surface temperature (LST) was retrieved from AHS thermal infrared data acquired in 2004 and 2005 using the split-window algorithm described in Sobrino et al. (2006). For the

UAV imagery, surface temperature was obtained applying atmospheric correction methods based on the MODTRAN radiative transfer model. Local atmospheric conditions such as air temperature, relative humidity and barometric pressure were measured at the time of flight with a portable weather station (Model WXT510, Vaisala, Finland) and used as input into MODTRAN. A single-layer atmosphere with uniform conditions was considered for the simulations since the variation for the typical UAV flight altitude (150-200 m) could be neglected. Optical path transmissivity and thermal radiance were calculated for every pixel on the image, taking into account the flight elevation and the effects introduced by the wide field of view and camera tilt angles. Additionally, the mosaicking process selects only the most nadir part of the overlapping images, limiting the viewing angle and thus avoiding directional effects and thermal hotspot. The atmospheric correction methods showed a RMSE < 1 K in a validation with ground measured temperature over three different targets at different times of the day (Berni et al., 2009).

## 4. Results and Discussion

### 4.1. Model Performance

Data from the albedometer on clear days was plotted for different solar zenith angles ( $\theta$ ) resulting in a relationship between  $\cos(\theta)$  and albedo (eq. 3.11) with  $r^2=0.83$  and a RMSE=0.044:

$$\alpha_c = 0.1268 \cdot \cos(\theta)^{-0.4356} \quad [3.11]$$

Downwelling longwave radiation was estimated using  $e_a$  and  $T_a$  to calculate the clear sky atmospheric emissivity. The cloudiness factor ( $clf$ ) was calculated using the measured shortwave radiation and the estimated potential irradiance. However, poor results were obtained when the cloudiness factor was applied with the 10 minute interval dataset; using a daily average  $clf$  improved estimates, even on almost-clear days (RMSE=7.96 W/m<sup>2</sup>, MBE=-0.78 W/m<sup>2</sup>). Finally, net radiation was estimated for a number of selected dates and compared with the direct measurements from the albedometer and net pyrgeometer, showing a good fit between estimated and measured net radiation (RMSE= 22.53 W/m<sup>2</sup>, MBE=9.04 W/m<sup>2</sup>).

Aerodynamic resistance was calculated using 10 minute data with the methodology proposed in Section 2.2. Canopy temperature and meteorological data were used to calculate  $H_c$  and  $\lambda E_c$  by means of Equations 3.2 and 3.3, showing in Figure 3.2 the calculations for the day of the AHS airborne flight (197). As expected, fully irrigated trees showed higher  $\lambda E_c$  and lower  $H_c$  as

compared with the deficit irrigation trees. Figure 3.2b shows RDI and SDI treatments, observing that  $\lambda E_c$  starts to decline soon after 8:00 GMT with a strong reduction after noon, while  $\lambda E_c$  fluxes for the FI trees were maintained all along the midday, starting to decrease when net radiation was reduced. For  $G_c$ , canopy resistance was calculated using Equation 3.4, deriving  $G_c$  as the inverse of  $r_c$  (Monteith & Unsworth, 2008).

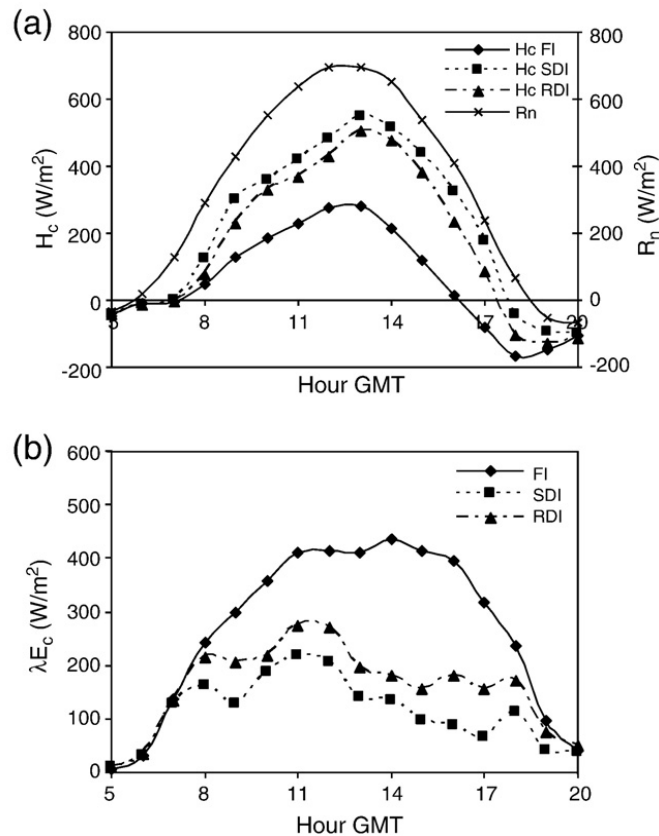


**Figure 3.2.** Diurnal course of net radiation ( $R_n$ ), sensible heat ( $H_c$ ) and latent heat ( $\lambda E_c$ ), hourly averaged for each treatment on DOY 197.

The diurnal course of canopy conductance curve for each treatment (Figure 3.3) reflects a pattern similar to the response as a function of water deficits of olive stomata shown in Moriana et al. (2002), and to the  $G_c$  behavior reported in Villalobos et al. (2000) and in Orgaz et al. (2007).

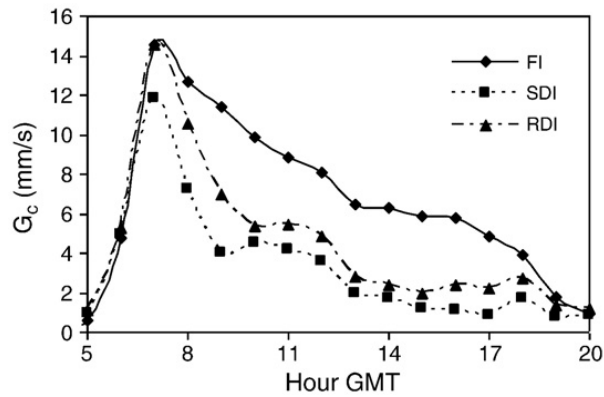


**Figure 3.3.** Hourly averaged estimations for simulated canopy conductance on DOY 197 using Eq. 3.4.

The pattern shows a sudden increase in  $G_c$  early in the morning, a progressive decline as a result of stomata closure during the central hours of the day, and very low values with the absence of solar radiation at the end of the day. Figure 3.3 also depicts the effects of water deficits on  $G_c$  values of each treatment, showing that deficit irrigated trees closed stomata sooner than the control trees as their canopy conductance values were lower, even approaching to zero after midday.

Figure 3.4 shows the behavior of the estimated  $G_c$  at noon during summer 2005 for each treatment, observing that full irrigated trees (FI) yielded greater  $G_c$  compared with the deficit irrigated trees (RDI and SDI), reaching the maximum differences during mid July to August. Three arrows (shown in Figure 3.4) indicate rainfall events that took place during summer 2005, noting after each rain event the increase in  $G_c$ , especially after May 12 (day of the year 132).

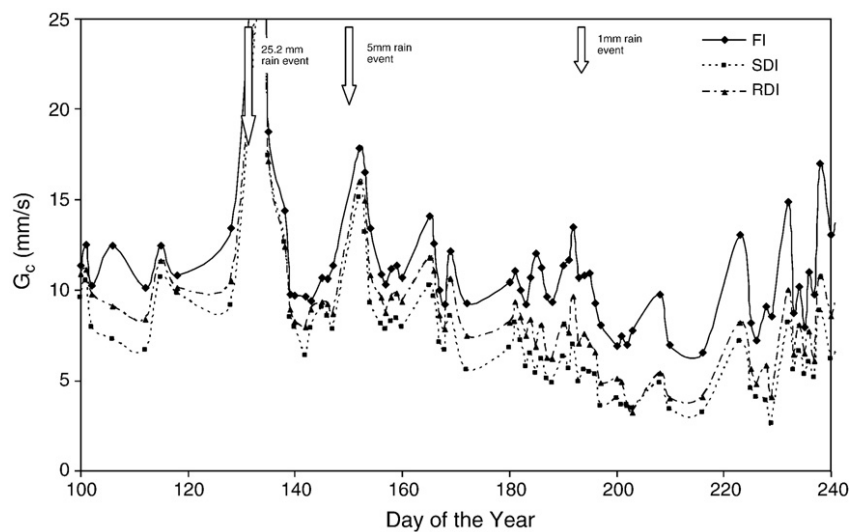


**Figure 3.4.** Seasonal variation of canopy conductance ( $G_c$ ) for the three different irrigation treatments obtained from the infrared sensor temperature at 12:00GMT during summer 2005.

## 4.2. Model Validation using ground thermal sensors

Two tests were conducted to assess the performance of the model against measurements with IRT sensors: a) comparing model estimates against canopy conductance measurements at different times from a single day; and b) comparing the model estimates for different dates at noon along summer 2005. Single day model estimates presented on Figure 3.5a show a relationship with  $r^2=0.63$  (slope = 1.17 and intercept=1.05) and a RMSE=2.63 mm/s. In the case of the validation for different dates, shown on Figure 3.5b, the determination coefficient ( $r^2=0.68$ ) suggests a reasonable model performance for different weather conditions. A large scatter for estimated  $G_c$  was found for low values of measured conductance. This could be explained by the large variability inherent to the leaf porometer measurement method and the scaling up from leaf to canopy levels. The assumption made was that the measured leaves represent the average population of the whole tree; however, since only a limited number of leaves can be measured for each tree, the resulting  $G_c$  could differ from the actual tree  $G_c$ . Unfortunately, measuring a larger number of leaves per tree, within a short time, is not possible for leaf porometry and therefore other methods, such as trunk sap flow or eddy covariance should be used to estimate actual  $G_c$ , which deserves further research. Nevertheless, these results suggest that thermal monitoring using point IRT sensors could be used to track canopy conductance and latent heat flux on isolated trees.

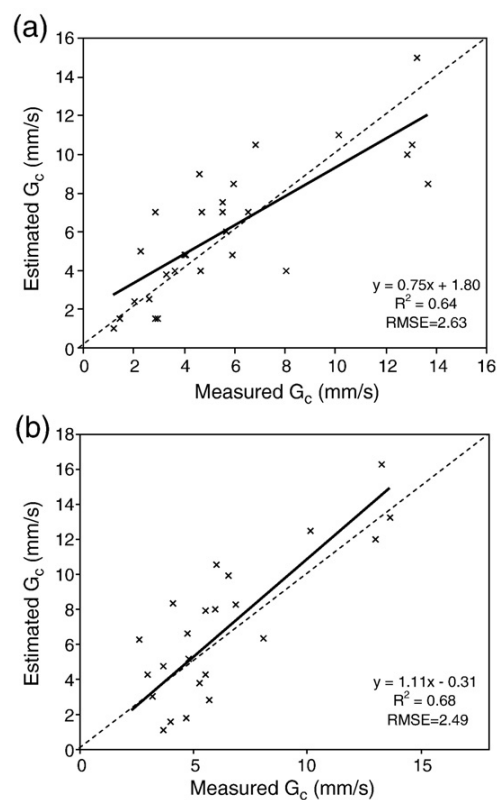


**Figure 3.5.** Relationship obtained between the measured canopy conductance ( $G_c$ ) and the estimated  $G_c$  for a) individual tree measurements at three times (7:30GMT, 9:30GMT and 12:30GMT) on 16 July 2005 (n=30), and b) treatment averages during summer of 2005 (n=25).

### 4.3. Model Validation using airborne remote sensing thermal imagery

The proposed methodology was applied to airborne thermal calibrated imagery collected in 2005 and 2007 campaigns. The required inputs for the model, latitude, longitude, day of the year and GMT time, enabled the calculation of net radiation for clear days; air temperature and relative humidity, actual solar radiation from the pyranometer and wind speed over grass. Canopy height, reference height,  $z_0/h$  and  $d/h$  can also be introduced in order to model the aerodynamic resistance. The 2 m resolution AHS thermal imagery was processed using an NDVI mask to extract pure crown temperature (as explained in Sepulcre-Cantó et al. (2006)) at the three times of day when the sensor was flown: 7:30, 9:30, and 12:30 GMT. The algorithm was applied to the masked images, estimating canopy conductance for each individual tree. Figure 6 shows the validation of the estimated values versus the field measured  $G_c$ , showing that the estimations for 7:30 and 9:30 GMT are close to the 1:1 line with a RMSE of 2.25 and 1.80 mm/s, respectively. However, the estimation conducted from the 12:30 GMT flight resulted in an overestimation of  $G_c$  as compared to the field measurements. The expected behavior would be an underestimation of  $G_c$  or even negative values as a consequence of the surrounding warm soil and pixel mixing. However, the good correlation between the estimated and the measured  $G_c$  values ( $r^2=0.59$ ), suggests a bias in the radiometric calibration or atmospheric correction of the AHS thermal imagery.

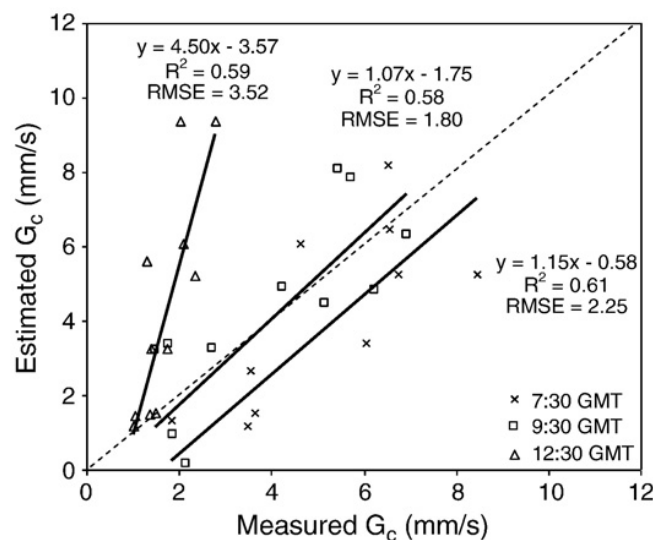


**Figure 3.6.** Relationship obtained for the field-measured leaf stomatal conductance and from the AHS imagery estimates for individual trees at the different times (7:30GMT, 9:30GMT and 12:30GMT) on DOY 197, 2005.

For the higher spatial resolution UAV thermal imagery acquired in 2007 summer campaign, individual tree crowns were delineated clearly due to the higher spatial resolution of the imagery (40 cm pixel size). The resulting estimated canopy conductance image (Figure 3.7) shows the well watered trees

(FI treatment) with higher canopy conductance, with lower  $G_c$  values corresponding to deficit irrigated trees (RDI and SDI treatments). Single-tree estimated  $G_c$  values were manually extracted from the imagery, identifying the trees where field measurements were conducted.

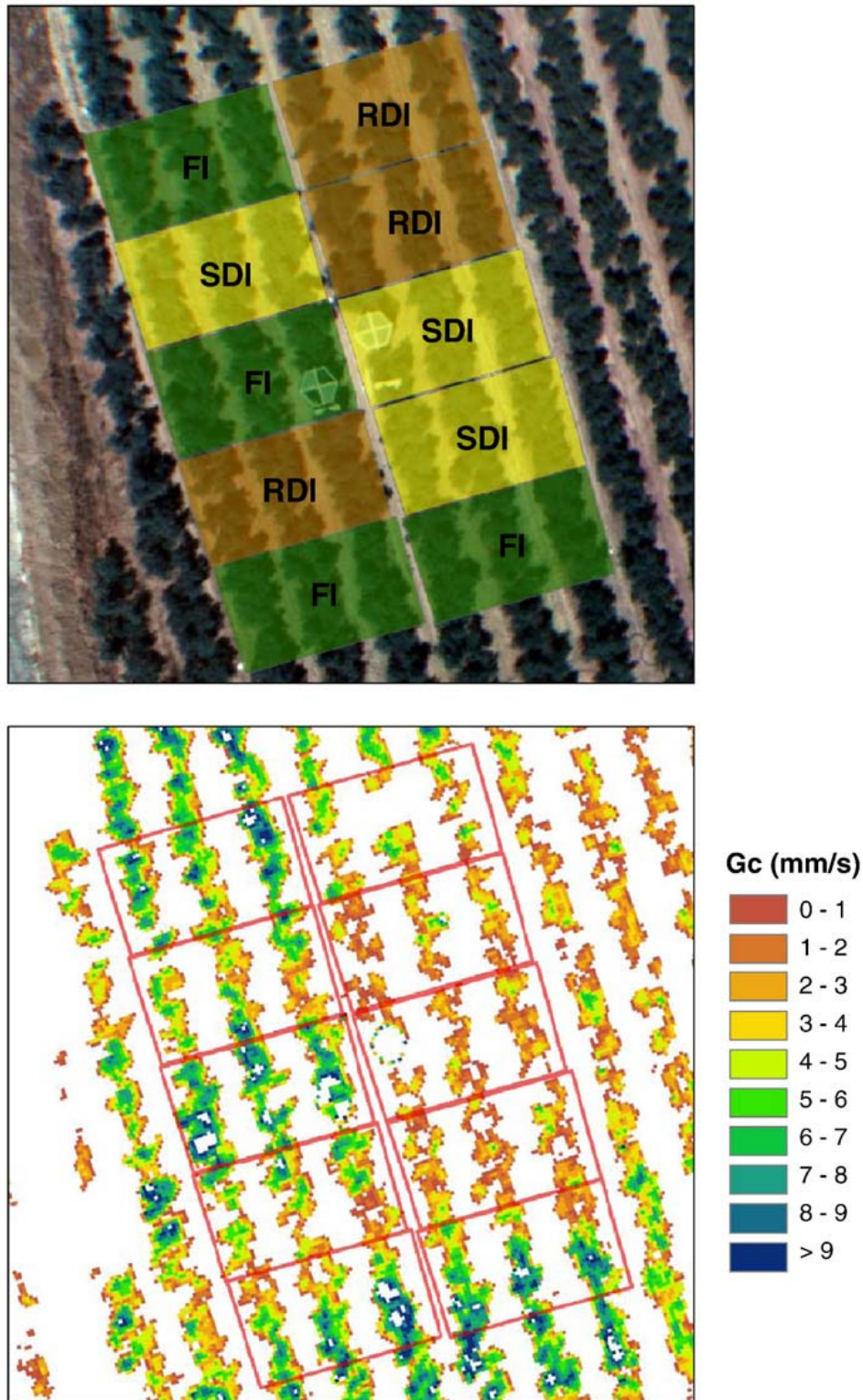


**Figure 3.7.** Canopy conductance map obtained from the UAV thermal imagery at 13:30 GMT 23 August 2007. Units are mm/s. Local conditions were  $T_a=304.16K$ ,  $RH=19.69\%$ ,  $U_g=1.2m/s$ .

The validation of the estimated  $G_c$  values (Figure 3.8) shows a very good relationship ( $r^2=0.91$ ) and a slope close to 1 (1.08) with an intercept of 0.84 mm/s (RMSE=1.65 mm/s). Additionally, the results show less scatter than those obtained from AHS thermal imagery, suggesting that higher spatial resolution is critical for an accurate extraction of pure crown canopy temperature and to avoid energy fluxes from the bare soil.

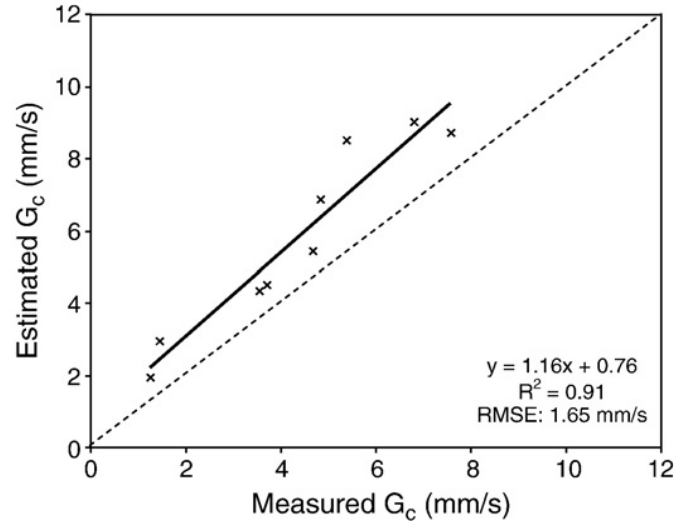


**Figure 3.8.** Validation of the canopy conductance estimations against field measurements. Each point shown represents an individual tree where 5 stomatal conductance measurements were taken.

#### 4.4. Mapping CWSI at high resolution in open-canopy orchards

To calculate the theoretical CWSI using Equation 3.9, the crop potential canopy conductance in absence of water stress should be known, which for olive trees is a strong function of VPD (Moriana et al., 2002; Testi et al., 2006). In this study, in order to determine the function of canopy potential conductance ( $G_{cp}$ ) as a function of the VPD, full irrigation trees were monitored and the estimations of  $G_c$  at noon on clear days with summer standard conditions ( $R_n=700 \text{ W/m}^2$ ) were plotted against the VPD, yielding a close relationship ( $r^2=0.7$ ) and the following equation:

$$G_{cp} = 25.533 \cdot VPD^{-0.7437} \quad [3.12]$$

CWSI was calculated using the estimated  $G_c$  from the air using the high resolution airborne imagery acquired in 2007 and the resulting  $G_{cp}$  from the meteorological conditions at the time of the flight, obtaining a CWSI map with values ranging from 0 to 1 (Figure 9).

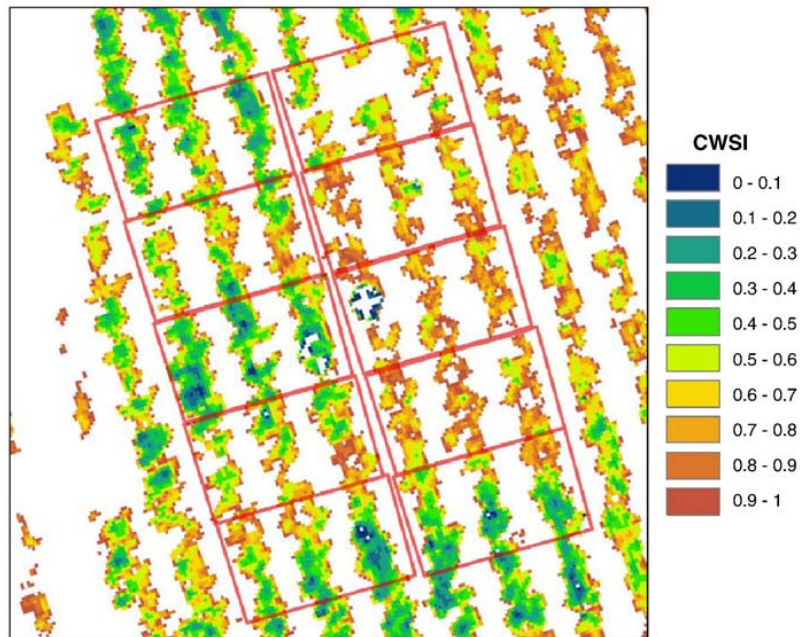


**Figure 3.9.** CWSI map obtained from the UAV high resolution thermal imagery at 13:30 GMT on 23 August 2007.

The value of CWSI was extracted for the trees where leaf water potential was measured. Figure 3.10 delineates the relationships between CWSI and leaf water potential (3.10a) and canopy conductance (3.10b) showing strong correlations ( $r^2=0.82$  and  $r^2=0.91$  respectively), which suggests that CWSI obtained from high spatial resolution thermal imagery can be used as a good indicator to map water stress in open tree canopies. Compared with a map of  $G_c$ , the main advantage of a CWSI map is that absolute values of  $G_c$  cannot be directly translated as an indicator of water stress, whereas CWSI may be used as a stress indicator because it is already normalized for weather conditions and crop characteristics.

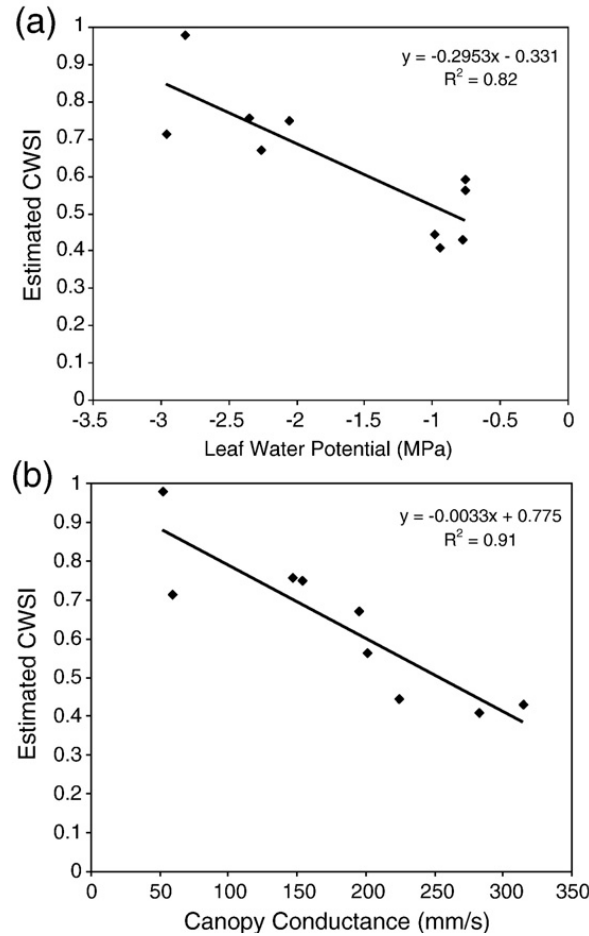


**Figure 3.10.** Relationships between the estimated CWSI from the UAV thermal imagery with a) leaf water potential and b) canopy conductance.

As indicated earlier, a major goal would consist on assessing the proposed modeling methodology to calculate the theoretical NWSB using analytical equations. The  $T_c - T_a$  value was calculated iterating Equation 3.13 as function of VPD with the following average conditions for the summer in Cordoba:  $R_n = 700 \text{ W/m}^2$  and  $650 \text{ W/m}^2$ ,  $T_c = 32^\circ\text{C}$ ,  $U_g = 2.24 \text{ m/s}$  and  $U_g = 1.5 \text{ m/s}$ .

$$T_c - T_a = \frac{r_a R_n}{\rho C_p} \cdot \frac{\gamma(1 + r_c / r_a)}{\Delta + \gamma(1 + r_c / r_a)} - \frac{VPD}{\Delta + \gamma(1 + r_c / r_a)} \quad [3.13]$$

Additionally, the *non-water-stressed baseline* (NWSB) was obtained empirically using the  $T_c - T_a$  values for the trees of the FI treatment (fully irrigated) close to solar noon (12:30 GMT, AHS sensor flight time) using hourly averaged values from clear days from April to September 2005 (days of the year 100-252) were used. The calculated NWSB ( $T_c - T_a = 0.35 \cdot VPD + 2.08$ ,  $r^2 = 0.67$ ) showed large scatter and a very small slope compared with reported baselines from other authors. This means that for large variations of VPD,  $T_c - T_a$  varies less than 1.5K, which is a very small difference if compared with NWSB for herbaceous crops but also for some tree species such as pistachio (Testi et al.,

2008). This is a consequence of the small leaves of the olive which are highly coupled to the atmosphere (Villalobos et al., 2000), and also because even for well irrigated trees, some stomatal closure occurs when the evaporative demand increases. A consequence of this very small slope is that CWSI for olive trees is very sensitive to errors in the estimation of  $T_c$  and the measurement of  $T_a$ .

Figure 3.11 shows the resulting NWSB simulations as compared with the empirical NWSB (solid line). The plot agrees with the theoretical estimates of Hipps et al. (1985) and with the experimental results of Testi et al. (2008) who determined NWSB lines for pistachio, where the variations in radiation caused by time of day also resulted in parallel baselines. This suggests that the model formulated in the present paper could be used to determine NWSB without the limitations of local conditions and the empiricism involved in the original methodology of Idso et al. (1981). Although the traditional NWSB approach is still useful, the methodology proposed here could be used to generate baselines for different conditions and crops to be used by farmers applying CWSI as an irrigation scheduling technique.

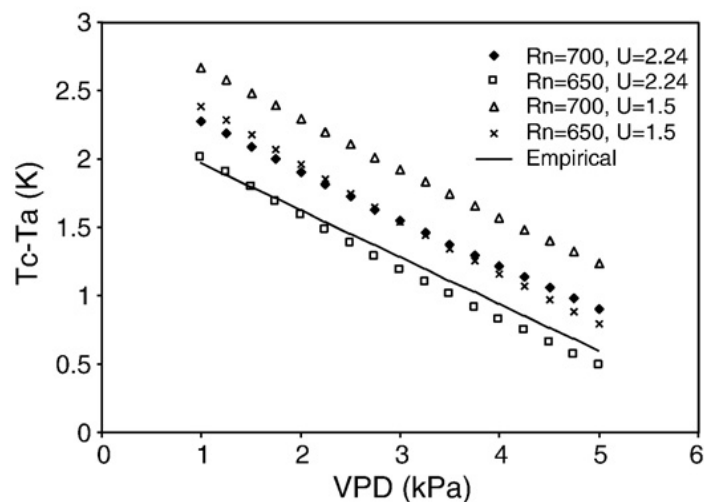


**Figure 3.11.** Simulations of NWSB for CWSI from 4 weather conditions:  $R_n=600\text{W/m}^2$ ,  $R_n=650\text{W/m}^2$ ,  $U_g=2.24\text{m/s}$  and  $U_g=1.5\text{m/s}$ .  $T_a$  was fixed to  $32^\circ\text{C}$ . The solid line is the NWSB estimated empirically.

## **5. Concluding remarks**

The detection of water stress in the field has been hampered by the uncertainty in determining the significance of point measurements of the actual field conditions. In addition, the number of point measurements collected is often limited by the time and cost of acquisition, reason that increases the uncertainty further. Options to spatially map water stress conditions in heterogeneous canopies, such as orchards, via remote sensing have been limited by the lack of spatial and temporal resolution of satellite based approaches. This

manuscript shows the feasibility for mapping two features directly related to the actual transpiration of olive orchards as affected by water deficits. Energy balance equations and the theoretical formulation of the CWSI have been combined with very high resolution thermal imagery to calculate  $G_c$  and CWSI for an heterogeneous olive canopy. Results showed their close relationship when calculated with standard approaches, demonstrating a successful validation against water potential and stomatal conductance field measurements. The ability to produce high resolution maps of  $G_c$  and CWSI, potentially used to calculate actual ET, and to be used as input for irrigation scheduling methods, respectively, provides a powerful tool for future applications of this methodology in the context of precision agriculture.

The potential use of new remote sensing methodologies based on active sensors could provide a better knowledge of the canopy structure (Moorthy et al., 2008), particularly on sparse canopies, and would help to refine the estimates of some of the parameters involved in this methodology, such as aerodynamic resistance and net radiation.

### **6. Acknowledgements**

This work was funded by the Ministerio de Educación y Ciencia (MEC) of Spain with projects AGL-2003-01468, AGL2005-04049, EXPLORA-INGENIO AGL2006 26038-E/AGR, and CONSOLIDER CSD2006-67, as well as the Junta de Andalucía – with project AGR-595, and in-kind support provided by Bioiberica through project PETRI PET2005-0616. Technical support from UAV Navigation and Tetracam Inc. for accommodating airborne requirements are also acknowledged. V. González, M. Morales, C. Ruz, D. Notario, M. Guillén, C. Trapero, I. Calatrava, A. Vera and M. Ruiz Bernier are acknowledged for measurements and technical support in field and airborne campaigns. Special thanks to Dr. Luca Testi for his comments and support.

## **References**

Baldocchi, D.D.; Luxmoore, R.J.; Hatfield, J.L. (1991) Discerning the forest from the trees: an essay on scaling canopy stomatal conductance. *Agricultural and Forest Meteorology*, 54, 197-226.

Berk, A.; Anderson, G.; Acharya, P.; Chetwynd, J.; Bernstein, L.; Shettle, E.; Matthew, M.; Adler-Golden, S. (1999) *MODTRAN4 user's manual*.

Berni, J.A.J.; Zarco-Tejada, P.J.; Suarez, L.; Fereres, E. (2009) Thermal and narrow-band multispectral remote sensing for vegetation monitoring from an unmanned aerial vehicle. *IEEE Transactions on Geoscience and Remote Sensing*, 47, (3), 722-738.

Brest, C.L.; Goward, S.N. (1987) Deriving surface albedo measurements from narrow band satellite data. *International Journal of Remote Sensing*, 8, 351-367.

Brutsaert, W. (1975) On a derivable formula for long-wave radiation from clear skies. *Water Resources Research*, 11, 742-744.

Brutsaert, W.H. (1982) *Evaporation into the atmosphere: theory, history, and applications*. D. Reidel Publishing Co. Dordrecht.

Cohen, Y.; Alchanatis, V.; Meron, M.; Saranga, Y.; Tsipris, J. (2005) Estimation of leaf water potential by thermal imagery and spatial analysis. *Journal of Experimental Botany*, 56, 1843-1852.

Crawford, T.M.; Duchon, C.E. (1999) An improved parameterization for estimating effective atmospheric emissivity for use in calculating daytime downwelling longwave radiation. *Journal of Applied Meteorology*, 38, 474-480.

Fuchs, M.; Tanner, C.B. (1966) Infrared thermometry of vegetation. *Agronomy Journal*, 58, 297-601.

Furon, A.C.; Warland, J.S.; Wagner-Riddle, C. (2007) Analysis of scaling-up resistances from leaf to canopy using numerical simulations. *Agronomy Journal*, 99, 1483-1491.

Garratt, J.R. (1980) Surface influence upon vertical profiles in the atmospheric near- surface layer. *Quarterly Journal, Royal Meteorological Society*, 106, 803-819.

Glenn, D.; Worthington, J.; Welker, W.; McFarland, M. (1989) Estimation of peach-tree water-use using infrared thermometry. *Journal of the American Society for Horticultural Science*, 114, 737-741.

Grant, O.M.; Tronina, L.; Jones, H.G.; Chaves, M.M. (2007) Exploring thermal imaging variables for the detection of stress responses in grapevine under different irrigation regimes. *Journal of Experimental Botany*, 58, 815-825.

Hatfield, J.L. (1989) Aerodynamic properties of partial canopies. *Agricultural and Forest Meteorology*, 46, 15-22.

Herwitz, S.; Johnson, L.; Dunagan, S.; Higgins, R.; Sullivan, D. et al. (2004) Imaging from an unmanned aerial vehicle: agricultural surveillance and decision support. *Computers and Electronics in Agriculture*, 44, 49-61.

- Hipps, L.; Asrar, G.; Kanemasu, E. (1985) A theoretically-based normalization of environmental effects on foliage temperature. *Agricultural and Forest Meteorology*, 35, 113-122.
- Hsiao, T.C. (1990) *Measurements of plant water status*. American Society of Agronomy, Madison (EUA); Crop Science Society of America, Madison (EUA); Soil Science Society of America, Madison (EUA).
- Idso, S.; Jackson, R.; Pinter P.J., J.; Reginato, R.; Hatfield, J. (1981) Normalizing the stress-degree-day parameter for environmental variability. *Agricultural Meteorology*, 24, 45-55.
- Idso, S.; Jackson, R.; Reginato, R. (1978) Extending the 'degree-day' concept of plant phenological development to include water stress effects. *Ecology*, 59, 431-433.
- Idso, S.B. (1982) Non-water-stressed baselines: a key to measuring and interpreting plant water stress. *Agricultural Meteorology*, 27, 59-70.
- Iniesta, F.; Testi, L.; Orgaz, F.; Villalobos, F.J. (2009) The effects of regulated and continuous deficit irrigation on the water use, growth and yield of olive trees. *European Journal of Agronomy*, 30, 258-265.
- Jackson, R.; Idso, S.; Reginato, R.; Pinter Jr, P. (1981) Canopy temperature as a crop water stress indicator. *Water Resources Research*, 17, 1133-1138.
- Jackson, R.; Reginato, R.; Idso, S. (1977a) Wheat canopy temperature: a practical tool for evaluating water requirements. *Water Resources Research*, 13, 651-656.
- Jackson, R.D. (1982) Canopy temperature and crop water stress. *Advances in Irrigation*, 1, 43-85.
- Jackson, R.D.; Idso, S.B.; Reginato, R.J.; Ehrlter, W.L. (1977b) Crop temperature reveals stress. *Crop Soils*, 29, 10-13.
- Jackson, R.D.; Kustas, W.P.; Choudhury, B.J. (1988) A reexamination of the crop water stress index. *Irrigation Science*, 9, 309-317.
- Jarvis, P.G. (1976) The interpretation of the variations in leaf water potential and stomatal conductance found in canopies in the field. *Philos. Trans. R. Soc. London*, 273, 593-610.
- Jones, H.G. (1999) Use of infrared thermometry for estimation of stomatal conductance as a possible aid to irrigation scheduling. *Agricultural and Forest Meteorology*, 95, 139-149.
- Jones, H.G.; Stoll, M.; Santos, T.; Sousa, C.D.; Chaves, M.M. et al. (2002) Use of infrared thermography for monitoring stomatal closure in the field: application to grapevine. *Journal of Experimental Botany*, 53, 2249-2260.
- Kjaersgaard, J.H.; Plauborg, F.L.; Hansen, S. (2007) Comparison of models for calculating daytime long-wave irradiance using long term data set. *Agricultural and Forest Meteorology*, 143, 49-63.
- Leinonen, I.; Grant, O.M.; Tagliavia, C.P.P.; Chaves, M.M.; Jones, H.G. (2006) Estimating stomatal conductance with thermal imagery. *Plant, Cell and Environment*, 29, 1508-1518.

Lhomme, J. (1991) The concept of canopy resistance: historical survey and comparison of different approaches. *Agricultural and Forest Meteorology*, 54, 227-240.

Lhomme, J.P.; Monteny, B. (2000) Theoretical relationship between stomatal resistance and surface temperatures in sparse vegetation. *Agricultural and Forest Meteorology*, 104, 119-131.

Liang, S. (2001) Narrowband to broadband conversions of land surface albedo algorithms. *Remote Sensing of Environment*, 76, 213-238.

Liu, S.; Lu, L.; Mao, D.; Jia, L. (2007) Evaluating parameterizations of aerodynamic resistance to heat transfer using field measurements. *Hydrology and Earth System Sciences*, 11, 769-783.

Monteith, J.L.; Unsworth, M.H. (2008) *Principles of environmental physics*. Elsevier/Academic Press. 440 p.

Moorthy, I.; Miller, J.R.; Baoxin, H.; Chen, J.; Qingmou, L. (2008) Retrieving crown leaf area index from an individual tree using ground-base LIDAR data. *Canadian Journal of Remote Sensing*, 34, 320-332.

Moran, M.S.; Clarke, T.; Inoue, Y.; Vidal, A. (1994) Estimating crop water deficit using the relation between surface-air temperature and spectral vegetation index. *Remote Sensing of Environment*, 49, 246-263.

Moriana, A.; Fereres, E. (2002) Plant indicators for scheduling irrigation of young olive trees. *Irrigation Science*, 21, 83-90.

Moriana, A.; Villalobos, F.J.; Fereres, E. (2002) Stomatal and photosynthetic responses of olive (*Olea europaea* L.) leaves to water deficits. *Plant, Cell and Environment*, 25, 395-405.

Möller, M.; Alchanatis, V.; Cohen, Y.; Meron, M.; Tsipris, J. et al. (2007) Use of thermal and visible imagery for estimating crop water status of irrigated grapevine. *Journal of Experimental Botany*, 58, 827-838.

Nakayama, F.S.; Bucks, D.A. (1983) Application of a foliage temperature based crop water stress index to guayule (*Parthenium argentatum*). *Journal of Arid Environments*, 6, 269-276.

Norman, J.M.; Kustas, W.P.; Humes, K.S. (1995) Source approach for estimating soil and vegetation energy fluxes in observations of directional radiometric surface temperature. *Agricultural and Forest Meteorology*, 77, 263-293.

Orgaz, F.; Villalobos, F.J.; Testi, L.; Fereres, E. (2007) A model of daily mean canopy conductance for calculating transpiration of olive canopies. *Functional Plant Biology*, 34, 178-188.

Rana, G.; Kterji, N. (1998) A measurement based sensitivity analysis of the Penman-Monteith actual evapotranspiration model for crops of different height and in contrasting water status. *Theoretical and Applied Climatology*, 60, 141-149.

Ritchie, J.T. 1972. Model for predicting evaporation from a row crop with incomplete cover, *Water Resources Research* 8, 1204-1213.

Salisbury, J.W.; D'Aria, D.M. (1992) Emissivity of terrestrial materials in the 8-14  $\mu\text{m}$  atmospheric window. *Remote Sensing of Environment*, 42, 83-106.

Sepaskhah, A.R.; Kashefipour, S.M. (1994) Relationships between leaf water potential, cws<sub>i</sub>, yield and fruit quality of sweet lime under drip irrigation. *Agricultural Water Management*, 25, 13-22.

Sepulcre-Cantó, G.; Zarco-Tejada, P.; Jiménez-Muñoz, J.; Sobrino, J.; Soriano, M. et al. (2007) Monitoring yield and fruit quality parameters in open-canopy tree crops under water stress, implications for ASTER. *Remote Sensing of Environment*, 107, 470.

Sepulcre-Cantó, G.; Zarco-Tejada, P.; Jiménez-Muñoz, J.; Sobrino, J.; de Miguel, E. et al. (2006) Detection of water stress in an olive orchard with thermal remote sensing imagery. *Agricultural and Forest Meteorology*, 136, 44.

Shackel, K.A.; Ahmadi, H.; Biasi, W.; Buchner, R.; Goldhamer, D. et al. (1997) Plant water status as an index of irrigation need in deciduous fruit trees. *Hort. Technology*, 7, 23-29.

Smith, R.C.G. (1988) Inferring stomatal resistance of sparse crops from infrared measurements of foliage temperature. *Agricultural and Forest Meteorology*, 42, 183-198.

Sobrino, J.; Jimenez-Munoz, J.; Zarco-Tejada, P.; Sepulcre-Cantó, G.; de Miguel, E. (2006) Land surface temperature derived from airborne hyperspectral scanner thermal infrared data. *Remote Sensing of Environment*, 102, 115.

Sugiura, R. and Noguchi, N. and Ishii, K. (2005) Remote-sensing technology for vegetation monitoring using an unmanned helicopter. *Biosystems Engineering*, 90, 369-379.

Tanner, C.B. (1963) Plant temperatures. *Agronomy Journal*, 55, 210-211.

Testi, L.; Goldhamer, D.A.; Iniesta, F.; Salinas, M. (2008) Crop water stress index is a sensitive water stress indicator in pistachio trees. *Irrigation Science*, 26, 395-405.

Testi, L.; Orgaz, F.; Villalobos, F.J. (2006) Variations in bulk canopy conductance of an irrigated olive (*Olea europaea* L.) orchard. *Environmental and Experimental Botany*, 55, 15-28.

Testi, L.; Villalobos, F.J.; Orgaz, F. (2004) Evapotranspiration of a young irrigated olive orchard in Southern Spain. *Agricultural and Forest Meteorology*, 121, 1-18.

Verhoef, A.; McNaughton, K.G.; Jacobs, A.F.G. (1997) A parameterization of momentum roughness length and displacement height for a wide range of canopy densities. *Hydrology and Earth System Sciences*, 1, 81-91.

Villalobos, F.J.; Orgaz, F.; Testi, L. (2000) Measurement and modeling of evapotranspiration of olive (*Olea europaea* L.) orchards. *European Journal of Agronomy*, 13, 155-163.

Viney, N.R. (1991) An empirical expression for aerodynamic resistance in the unstable boundary layer. *Boundary-Layer Meteorology*, 56, 381-393.

Wanjura, D.F.; Hatfield, J.L.; Upchurch, D.R. (1990) Crop water stress index relationships with crop productivity. *Irrigation Science*, 11, 93-99.

Yazar, A.; Howell, T.A.; Dusek, D.A.; Copeland, K.S. (1999) Evaluation of crop water stress index for LEPA irrigated corn. *Irrigation Science*, 18, 171-180.

## Discusión general

*No es deshonor no alcanzar una cosa, sino cesar de poner los medios.*

Lucio Anneo Séneca (4 a.C.-65 d.C.)

A través de los capítulos de esta Tesis Doctoral se muestra una novedosa forma de llevar a cabo teledetección cuantitativa mediante el uso de vehículos aéreos no tripulados.

Este tipo de plataformas permiten la obtención de imágenes de alta resolución espacial, que gracias a los sensores propuestos y a la configuración de bandas espectrales en la posición y ancho necesarios para el cálculo de índices de vegetación adecuados, posibilitan la estimación de parámetros biofísicos y constituyentes bioquímicos. Cuentan además con la ventaja de poder ser operadas con una alta frecuencia temporal, tal como se ha demostrado en alguno de los experimentos. Además, el uso de métodos de fotogrametría analítica digital permite la generación de mosaicos digitales a partir de los cientos o miles de imágenes que se capturan durante el vuelo sobre una zona de estudio. Esto, unido a la potencia de cálculo de los ordenadores actuales, hace pensar que el tiempo de entrega de resultados al agricultor podría ser menor de 24 horas, una de las limitaciones de otros métodos tradicionales de teledetección.

Sin embargo, la clave del éxito de este tipo de aplicaciones es la capacidad de generar resultados basados en la estimación de parámetros biofísicos que tengan interés en el manejo de cultivos (que podemos llamar productos) y que puedan ser validados y contrastados. Eso sólo será posible mediante el uso de metodologías cuantitativas que hagan uso de modelos de transferencia radiativa (RTM) para considerar y minimizar los efectos que sobre la energía reflejada o emitida por la vegetación tengan, por ejemplo, el suelo, la densidad foliar, la atmósfera, etc.

En la primera parte de esta tesis se ha prestado especial atención a todas las metodologías de calibración de los sensores desde un punto de vista radiométrico, así como a la necesidad de correcciones atmosféricas para llegar a obtener reflectancia y temperatura de superficie. Las metodologías empleadas han sido similares a las utilizadas con sensores instalados a bordo de aviones tripulados pero adaptadas a este tipo de sensores. Los resultados obtenidos en la validación muestran que es posible estimar la reflectancia con un error medio cuadrático (RMSE) de sólo 1.17% sobre las medidas realizadas con espectrorradiómetro en campo. De igual modo, para la temperatura de superficie se han obtenido errores inferiores a 1 K (RMSE = 0.87 K).

También se han tenido en cuenta los aspectos geométricos, ya que el objetivo es la obtención de imágenes georreferenciadas y la posterior generación de mosaicos a partir de todas las imágenes capturadas durante el vuelo. Para este fin se han realizado calibraciones geométricas de las cámaras que permiten, por ejemplo, determinar los parámetros para eliminar la

distorsión de la óptica. Posteriormente se han utilizado técnicas de fotogrametría analítica que combinan los datos obtenidos del sistema de navegación y la búsqueda de puntos automáticos para la generación de mosaicos de forma lo más automatizada posible.

Las estimaciones de parámetros biofísicos y constituyentes bioquímicos, obtenidas a partir de las imágenes de reflectancia y temperatura de superficie, muestran que los resultados son iguales o superiores a los obtenidos en trabajos publicados y realizados con sensores contrastados instalados a bordo de aviones tripulados. Así, se han obtenido coeficientes de determinación de NDVI con LAI de  $r^2=0.5$  para maíz y  $r^2=0.88$  para olivar; en la estimación de contenido clorofílico a partir de TCARI/OSAVI se ha obtenido un RMSE=4.2 $\mu$ g/cm<sup>2</sup> y  $r^2=0.89$ ; el índice PRI ha mostrado igualmente una buena correlación con el estrés hídrico estimado a partir de la temperatura de superficie en maíz ( $r^2=0.69$ ) para ensayos con similar índice de área foliar. Por último, la temperatura de superficie obtenida con alta resolución espacial y temporal ha mostrado cómo se puede monitorizar el comportamiento estomático en un ensayo de variedades en maíz, o cómo se pueden identificar tratamientos de riego diferenciado en cultivos leñosos.

Una vez validada la calidad de los datos obtenidos con esta plataforma, y gracias a las características de la misma, también ha sido posible desarrollar dos nuevas metodologías para la detección del estado hídrico de la vegetación. Se han presentado dos metodologías: una basada en imágenes de la cámara multispectral y otra basada en imágenes de la cámara térmica.

La primera metodología se basa en la obtención de imágenes de fluorescencia clorofílica en estado estacionario ( $F_s$ ) bajo condiciones de iluminación natural usando el método del *in-filling*. Se ha usado el modelo FluorMOD para estudiar la capacidad que los distintos índices de fluorescencia publicados tienen de detectar la fluorescencia, y la influencia que en los mismos tienen parámetros como el contenido clorofílico ( $C_{ab}$ ) y el índice de área foliar. Con ello se ha demostrado que el método del *in-filling*, junto los índices D702/D680 y R761-R757 son los que presentan una mejor relación con la fluorescencia ( $r^2>0.69$ ) y menor influencia a las variaciones de  $C_{ab}$  ( $r^2<0.34$ ) y LAI ( $r^2<0.08$ ). Por el contrario, otros índices aceptados en la bibliografía se han mostrado muy afectados por variaciones de  $C_{ab}$  y LAI. Para la obtención de las imágenes fue necesario instalar en la cámara filtros de 1 nm de ancho de banda centrados en las 757.5 y 760.5 nm. Ello implica que la cantidad de radiación que llega a los sensores es muy reducida en comparación con los filtros de 10nm empleados anteriormente. Sin embargo, los ajustes de la cámara, sus características de señal/ruido y la calibración radiométrica en laboratorio permitieron la obtención de este tipo de imágenes. La fluorescencia extraída a

partir de las imágenes fue validada mediante la comparación de medidas de campo de  $F_s$  usando los instrumentos PAM-2100 y GFS-3000, confirmando éstas las predicciones de las simulaciones. Los experimentos de estrés hídrico llevados a cabo en olivar y melocotonero demostraron la viabilidad de extraer fluorescencia clorofílica ( $F$ ) a nivel de árbol a partir de imágenes aéreas, resultando en coeficientes de determinación de  $r^2=0.57$  (olivar) y  $r^2=0.54$  (melocotonero). La estimación de fluorescencia aérea y su relación con la asimilación ( $A$ ) medida en el ensayo de variedades de olivar sin niveles de estrés hídrico mostraron resultados consistentes, dando lugar a  $r^2=0.71$  en la comparación de las estimaciones realizadas en varios vuelos realizados a lo largo de un día. Esto demuestra la viabilidad de utilizar la fluorescencia clorofílica detectada mediante un sensor aerotransportado para detectar cambios diurnos en fotosíntesis a escala de copa. En cuanto a la capacidad de esta metodología para la detección de estrés hídrico, los resultados se muestran consistentes con la bibliografía al registrarse valores inferiores de  $F$  en la imagen de los tratamientos de riego deficitario, comparado con los tratamientos control.

La segunda metodología trata de cuantificar el estado hídrico mediante la estimación de la conductancia de la cubierta  $G_c$  usando para ello imágenes térmicas de alta resolución espacial que permiten aislar los elementos vegetativos del resto de componentes, como el suelo. El modelo presentado se basa en el uso de las ecuaciones del balance de energía, de forma que se determina el parámetro  $G_c$  a partir de la estimación de los distintos componentes que intervienen en dichas ecuaciones. Para ello es necesario conocer, además de la temperatura de la cubierta, parámetros atmosféricos como la temperatura del aire y humedad relativa, además de la velocidad de viento y la radiación solar que se utilizan como entrada en modelos físicos para simular la resistencia aerodinámica y la radiación neta respectivamente. Se trata, por lo tanto, de un modelo que se puede aplicar tanto para su uso con sensores puntuales de temperatura, como a partir de imágenes térmicas. En la validación realizada a partir de datos medidos en continuo con sensores de infrarrojo térmico (IRT) se han utilizado tanto medidas realizadas a lo largo de todo un verano, como medidas realizadas a lo largo de un día. Las estimaciones de  $G_c$  se han mostrado consistentes para la detección de los distintos tratamientos de riego, tanto en las estimaciones horarias dentro del mismo día, como en la evolución estacional de la conductancia. La validación realizada frente a las medidas realizadas en campo a nivel foliar muestran una buena relación con las medidas realizadas a varias horas del día ( $r^2=0.64$ , RMSE=2.63mm/s), así como para la estimación estacional ( $r^2=0.68$ , RMSE=2.49mm/s). A nivel de imagen, se realizó una validación con medidas de campo en el momento del vuelo, y se obtuvieron unos buenos resultados para las imágenes obtenidas mediante la plataforma presentada ( $r^2=0.91$ ,

RMSE=1.65mm/s). Se ha empleado el CWSI como metodología para la normalización de la estimación del estrés hídrico con objeto de generar mapas de estrés de fácil interpretación. Los valores de CWSI obtenidos de la imagen se han validado frente a medidas de potencial hídrico realizadas en el momento del vuelo, obteniendo una buena relación ( $r^2=0.82$ ).

De forma general podemos decir que los buenos resultados obtenidos con estas dos aproximaciones para la detección del estado hídrico de la vegetación, cada una mediante un tipo de datos y metodologías totalmente diferentes, posibilitan su uso como unas herramientas de gran interés para la agricultura. Mediante estas dos metodologías es posible obtener mapas que muestren la distribución espacial del estrés, más allá de medidas puntuales que no permiten integrar la respuesta a nivel de parcela ya que no tienen en cuenta la variabilidad espacial de factores como el suelo, el sistema de riego, etc. Las aplicaciones que podrían usar dichos mapas van desde la programación de riegos hasta aplicaciones de agricultura de precisión que utilicen estos mapas para segmentar las parcelas agrícolas en zonas uniformes para su manejo. Del mismo modo, estas metodologías podrían ser usadas para la detección de procesos que impliquen una modificación del balance hídrico en la planta, o incluso que tengan influencia en el mecanismo fotosintético de la misma. Enfermedades de hongos vasculares, por ejemplo, así como otras enfermedades o plagas, podrían ser detectadas de forma indirecta mediante el uso de estos mapas de estrés.

Se puede afirmar que hoy realmente existe la tecnología (y además está disponible), para la implementación de las aplicaciones de teledetección en agricultura que se prometieron allá por los años 70-80. De igual forma que se produjo un salto cualitativo con el lanzamiento de los primeros satélites de observación de la Tierra, es probable que el desarrollo de los vehículos aéreos no tripulados suponga un nuevo salto cualitativo en la forma de entender la teledetección de las próximas décadas. Se trataría de una verdadera constelación de aviones que volarán de forma totalmente autónoma sobre las fincas agrícolas tomando imágenes térmicas y multiespectrales, a la vez que se reciben datos de redes de sensores instalados en las parcelas y que registrarán en tiempo real parámetros meteorológicos u otros como la humedad del suelo, el tamaño de los frutos, etc. Todas esas imágenes y datos se enviarán a un servidor central que en menos de 24 horas pondrá a disposición del usuario los resultados del análisis y mapas del estado de la finca, que serán accesibles mediante un visor de mapas a través de internet. De esa forma, el agricultor o gestor de la finca podrá tomar decisiones en tiempo real encaminadas a una mayor productividad o a un uso sostenible de los medios de producción, como es el caso del agua. Este escenario descrito más arriba ha dejado de ser una ficción, como lo era hace tres décadas.



## **Conclusiones generales**

*No entiendes realmente algo a menos que seas capaz de explicárselo a tu abuela.*

Albert Einstein (1879-1955)

1. En esta Tesis Doctoral se ha demostrado la viabilidad de generar productos de teledetección cuantitativa mediante un vehículo aéreo no tripulado y el uso de sensores comerciales de imagen multiespectral y térmica. Los métodos de calibración radiométrica y corrección atmosférica han permitido obtener imágenes multiespectrales de 6 bandas de 10 nm FWHM de ancho y 20 cm de resolución espacial, con un error medio cuadrático de 1.17% sobre la reflectancia medida en tierra con espectrómetro. De igual modo, se han obtenido imágenes térmicas de 40cm de resolución y con un error medio cuadrático tras la corrección atmosférica inferior a 1 K tras comparar con medidas realizadas en campo con pistola térmica en el momento de paso del avión.
2. La selección de las bandas multiespectrales ha permitido el cálculo de índices de vegetación de banda estrecha como el NDVI, TCARI/OSAVI y PRI, que han sido relacionados con parámetros biofísicos mediante el uso de metodologías cuantitativas basadas en el uso de modelos de transferencia radiativa, como PROSPECT o FLIGHT. Las estimaciones de LAI en maíz ( $r^2=0.5$ ) y olivar ( $r^2=0.88$ ), de contenido de clorofila a+b en maíz (RMSE=4.2 $\mu$ m/cm<sup>2</sup>;  $r^2=0.89$ ) o las relaciones de temperatura y PRI con conductancia estomática en maíz, muestran resultados similares, o superiores, a los obtenidos con sensores aerotransportados contrastados, usados en trabajos publicados con anterioridad. Ello es debido a la resolución submétrica utilizada en este trabajo.
3. Se ha demostrado que es posible la obtención de imágenes para detectar la emisión de fluorescencia clorofílica bajo condiciones de iluminación natural. Se ha validado el método del *in-filling*, usando filtros de 1 nm FWHM centrados en 757.5 y 760.5 nm, y que permitieron obtener imágenes de 15 cm de resolución sobre cubiertas vegetales. Mediante vuelos sobre parcelas experimentales de olivar y melocotonero se ha validado la estimación de fluorescencia a partir de las imágenes, comparando con medidas realizadas en campo con fluorímetro PAM-2100, resultando en valores de  $r^2=0.57$  para olivar y  $r^2=0.54$  para melocotonero. La comparación de la fluorescencia frente a medidas de asimilación como indicador de fotosíntesis también se ha mostrado consistente, obteniendo  $r^2=0.71$ . También se ha encontrado consistencia en los valores de fluorescencia detectados mediante las imágenes para los tratamientos de estrés hídrico,

mostrando una relación negativa con la temperatura como medida del estrés hídrico.

4. La alta resolución espacial en el térmico permite separar los flujos de energía en cultivos heterogéneos, y por lo tanto aplicar las ecuaciones del balance de energía a nivel de copa. Combinando la temperatura de superficie con medidas meteorológicas y modelos físicos, es posible obtener de forma analítica estimaciones de conductancia y CWSI de la cubierta a nivel de copa. La validación de  $G_c$  frente a medidas de conductancia estomática ( $r^2=0.91$ ;  $RMSE=1.65$  mm/s) y del CWSI frente al potencial hídrico ( $r^2=0.82$ ) demuestran que es posible mapear la conductancia de la cubierta y el estrés hídrico mediante el CWSI usando imágenes térmicas de resolución submétrica.
5. El desarrollo de nuevas técnicas de teledetección cuantitativa mediante vehículos aéreos no tripulados equipados con sensores multiespectrales y térmicos con resolución submétrica permitirá implementar estas técnicas en aplicaciones agrícolas como la gestión del agua de riego, lo que permitirá dar un paso hacia una nueva era en las aplicaciones de la teledetección a la agricultura.